Molecular Simulation of Chemically Reacting Flows Inside Micro/Nano–channels

by

Amir Ahmadzadegan

A thesis
presented to the University of Waterloo
in fulfillment of the
thesis requirement for the degree of
Doctor of Philosophy
in
Mechanical Engineering

Waterloo, Ontario, Canada, 2013

I hereby declare that I am the sole author of this thesis. This is a true copy of the thesis, including any required final revisions, as accepted by my examiners.

I understand that my thesis may be made electronically available to the public.

Abstract

The main objective of this thesis is to study the fundamental behaviour of multi–component gas mixture flows in micro/nano–channels undergoing catalytic chemical reactions on the walls. This work is primarily focused on nano–scale reacting flows seen in related applications; especially, miniaturized energy sources such as micro–fuel cells and batteries. At these geometries, the order of the characteristic length is close to the mean free path of the flowing gas, making the flow highly rarefied. As a result, non–equilibrium conditions prevail even the bulk flow and therefore, continuum assumptions are not held anymore. Hence, discrete methods should be adopted to simulate molecular movements and interactions described by the Boltzmann equation. The Direct Simulation Monte Carlo (DSMC) method was employed for the present research due to its natural ability for simulating a broad range of rarefied gas flows, and its flexibility to incorporate surface chemical reactions.

In the first step, fluid dynamics and the heat transfer of H_2/N_2 and $H_2/N_2/CO_2$ gas mixture slip flows in a plain micro–channel are simulated. The obtained results are compared to the corresponding data achieved from Navier–Stokes equations with slip/jump boundary conditions. Generally, very good agreements are observed between the two methods. It proves the ability of DSMC in replicating the fluid properties of multi–component gas mixtures even when high mass discrepancies exist among the species. Based on this comparison, the proper parameters are set for the prepared DSMC code, and the appropriate intermolecular collision model is identified. It is also found that stream variables should be calculated more accurately at flow boundaries in order to simulate the intense upstream diffusion emerging at low velocity flows frequently seen in micro/nano–applications. Therefore, in the second step, a novel pressure boundary condition is introduced for gas mixture flows by substituting the commonly used Maxwell velocity distribution with the Chapman–Enskog distribution function. It is shown that this new method yields better results for lower velocity and higher rarefaction level cases.

In the last step, a new method is proposed for coupling the flow field simulated by DSMC and surface reactions modelled by the species conservation ODE system derived from the reaction mechanism. First, a lean H_2/air slip flow subjected to oxidation on

platinum coated walls in a flat micro–channel 4μm in height is simulated as a verification test case. The results obtained are validated against the solutions of the Navier–Stokes equations with slip/jump boundary conditions and very good conformity is achieved. Next, several cases undergoing the same reaction with Reynolds numbers ranging from 0.2 to 3.6 and Knudsen numbers ranging from 0.025 to 0.375, are simulated using the verified code to investigate the effects of the channel height ranging from 0.5μm to 2μm , the inlet mass flow rate ranging from 5 kg/m^2·s to 25 kg/m^2·s, the inlet temperature ranging from 300K to 700K, the wall temperature ranging from 300K to 1000K, and the fuel/air equivalence ratio ranging from 0.28 to 1.5. Some of the findings are as follows: (1) increasing the surface temperature from 600K to 1000K and/or the inlet temperature from 300K to 700K results in negligible enhancement of the conversion rate, (2) the optimum value of the equivalence ratio is on the fuel lean side (around 0.5), (3) the efficiency of the reactor is higher for smaller channel heights, and (4) increasing the inlet mass flux elevates the reaction rate especially for the smaller channels; this effect is not linear and is more magnified for lower mass fluxes.

Acknowledgements

I am deeply grateful to my supervisors Professor Metin Renksizbulut and Professor John Wen for their continuous supports and productive instructions during my study. Their encouraging comments, patience, and sound advices made it possible to overcome the problems on the way of finishing the present thesis. Metin's supportive guidances have always motivated me to continue despite the hardship and move on. I could approach him without hesitation for help and advice.

I greatly appreciate the efforts of my defence committee members Professors John Chatzis, Cécile Devaud, and Kyle Daun, who contributed their valuable time to review my work and helped me fortify the thesis. I am especially thankful to Professor Kyle Daun for his great help and inspiring comments on my progress in our intermittent meetings and fruitful time I had as his teaching assistant. I am also sincerely thankful to Professor Henning Struchtrup for accepting to serve as the external examiner and travelling the long way from Victoria. I am greatly appreciative of his time and effort dedicated for reviewing my thesis.

This work was not possible without emotional support of my lovely wife, Saloumeh, who has filled my life with beauty and happiness since the wonderful moment of meeting her in the first year of my study. No word can express my gratitude to her patience and kindness during the last year reviving me with her indulgent smiles through our long–distance relationship. I am also profoundly indebted to my family for their constant inspiration and warm supports throughout this long period of time.

I warmly thank all the good friends whose companionship helped me to improve my personality and caused a delighted time in Waterloo: Amir Haddadzadeh, Madjid Soltani, Yahya Mahmoodkhani, Mohammad Derakhshani, Keivan Bakhoda, Samad Bazargan, Afshin Zamani, and Yasin Hosseinkhani. It was my honour to be the officemate of Azad Qazi Zade for four years and I really thank him for providing the Navier-Stokes solutions. I should thank my English tutor and my friend Matthew Zepf for all the productive and joyful time he devoted voluntarily for our sessions. I am also grateful to Cassie Smith, my counsellor, for all the invaluable insights I achieved from her constructive advices.

Dedication

This is dedicated to my love Saloumeh and my kind family.

Table of Contents

List of Tables

List of Figures

Nomenclature

General Symbols

A_v	Avogadro's number
$\vec{F}_b$	Body force vector
f	Velocity distribution function
k	The Boltzmann constant ($m^2 \cdot kg \cdot s^{-2} \cdot K^{-1}$)
Kn	Knudsen number
$\dot{m}_i''$	Mass flux of the species i ($kg \cdot m^{-2} \cdot s^{-1}$)
m	Molecular mass (kg)
m_r	Reduced mass
Ma	Mach number
$\dot{N}_i$	Molecular number flux of the species i ($m^{-2} \cdot s^{-1}$)
n	Number density (m^{-3})
$\underline{P}$	Pressure tensor
p	Pressure (Pa, bar=$10^5 Pa$)

p_r	Pressure ratio
$\vec{q}$	Heat transfer vector (W)
R	Specific gas constant $(J \cdot kg^{-1} \cdot K^{-1})$
R_f	Random number
Re	Reynolds number
S_n	Number of real molecules represented by each particle
T	Temperature (K)
T_s	Gas temperature next to the wall (K)
T_w	Wall temperature (K)
u,v,w	Components of the velocity vector $\underline{v}$ (m/s)
v	Velocity (m/s)
v'	Molecular thermal velocity (m/s)
v_0	Mean stream velocity (m/s)
V_{mp}	Most probable thermal velocity (m/s)
X_i	Molar fraction of species i
Y_i	Mass fraction of species i

Greek Symbols

β	Reciprocal of the most probable velocity
Γ	Density of catalytic free sites (m^{-2})
γ_i	Sticking factor of the species i

δ	Mean molecular spacing
$\underline{\delta}$	Unity tensor
ζ	Internal degrees of freedom
θ_i	Surface coverage of the species i
λ	Mean free path (m)
ν_f	Mean collision frequency (s^{-1})
ρ	Density $(kg \cdot m^{-3})$
σ	Molecular diameter (m)
σ_T	Collision cross section
ϕ	Air/fuel equivalence ratio
ω	Temperature exponent in the viscosity expression (viscosity index)

Subscripts

0	Mean stream values
in	Inlet
int	Internal
n	Normal component
out	Outlet
ref	Reference value
tr	Translational
x, y	Cartesian directions

Acronyms

DSMC	Direct Simulation Monte Carlo
DSMC/CE	DSMC results with pressure boundary condition derived from Chapman–Enskog velocity distribution
DSMC/M	DSMC results with pressure boundary condition derived from Maxwell velocity distribution
HS	Hard Sphere collision model
MCR	Mean Collision Rate
NS	Navier–Stokes solution
NSWS/J	Navier–Stokes solution with slip/jump boundary conditions
VHS	Variable Hard Sphere collision model
VSS	Variable Soft Sphere collision model

Chapter 1

Introduction

This thesis is dedicated to a fundamental study of gas mixture flows through flat micro/nano–channels undergoing chemical reactions on catalytic walls. The method introduced in this research can be used in developing future continuous flow micro/nano–reactors as a part of many progressing technologies in which catalytic walls are involved. Of the various applications, miniaturized sources of energy is mainly targeted in this thesis and is the base for choosing chemical reactions and gas species utilized in the problems studied. These energy sources are especially beneficial for next generations of electronic devices and micro electro–mechanical systems (MEMS) not only because of their very small sizes, but also for their durability. Developing such technologies would able their users, for example to have their cell phones on for days with just a drop of a fuel.

Another direction of the research followed in this thesis is focusing mostly on nano–scale reactors. A conceptual reactor can be assumed as a wafer type reactor consisting of several micro–reactor layers with similar arrangements as shown in Figure 1.1. As seen, a perforated plate is sandwiched between two plenums; one reserved for the inlet and the other for the outlet. The height of these plenums is considered well below the quenching distance in order to prevent any combustion outside the catalytic channels in the perforated plate. The inlet plenum provides a fuel/air mass flow, $\dot{m}_{in}$, with an equivalence ratio, ϕ. The homogenized fuel/air mixture enters the inlet plenum and eventually flows through the perforations in the plate. As shown in Figure 1.1 each perforation makes a

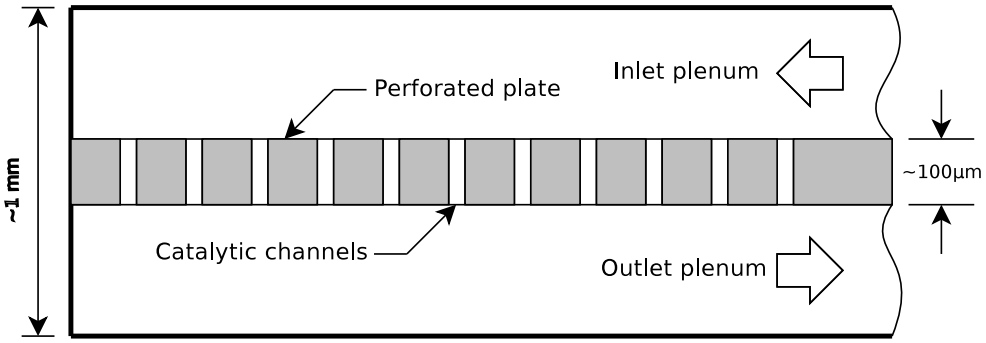

Figure 1.1: A conceptual wafer reactor

channel with a low height–to–width aspect ratio and with platinum coating on its walls. Therefore, the flow through the plate can be simulated as flow through a bundle of parallel channels and flow through each of these channels can be simulated as flow between parallel walls. Analyzing these reactors can also help to have better understanding the behavior of catalytical–chemical reactions in nano–porous media used in fuel cells and nano–channel reactors if the proper reaction mechanism is implemented. In order to attain this goal, it is necessary to understand all physical phenomena associated with micro/nano–scale reactors. A detailed experimental analysis which can capture variations in flow and surface properties along a micro/nano–reactor seems extremely difficult for the time being, based on current measurement technologies. Therefore, reliable numerical analysis is the only method that can be used for this purpose and is undertaken in the present work.

1.1 Rarefaction

Generally, the miniaturization of flow geometries intensifies non-equilibrium effects close to the walls and even in the bulk flow. This happens due to the fact that as the size of flow passages approach the mean molecular spacing, the number of molecules in the confined space decreases, assuming a constant pressure. As a result, the ratio of the mean collision rate of the molecules with the surrounding walls and the intermolecular collision rates depart from their equilibrium values. This hinders the information transfer between surfaces

and the flowing gas leading to some specific behaviours such as velocity slip, temperature jump, and concentration jump. These non-equilibrium phenomena are similar to that seen in low density conditions associated with low pressure environments and therefore, called rarefaction. The level of rarefaction depends on the characteristic size of the channel (h) and the mean free path of the flowing gas (λ). Thus, it is typically described by the ratio λ/h known as the Knudsen number Kn, based on which, micro-gas flows fall into four categories: continuum flow ($Kn < 0.005$[1]), slip flow ($0.005 < Kn < 0.1$), transition flow ($0.1 < Kn < 10$), and free molecular flow ($Kn > 10$). Conventional partial differential models like Navier-Stokes equations are only valid for the continuum flow regime. In the slip flow regime, bulk motion is still in equilibrium; however, non–equilibrium conditions arise between the wall surface and the adjacent gas flow. Therefore, Navier-Stokes equations can still be used for simulating the bulk motion (outside of the Knudsen layer) in the slip flow regime, and the discontinuity at the gas–wall interface is modelled by taking advantage of slip/jump boundary conditions. For the rest of the Kn range, however, the flow is fully rarefied and discrete molecular methods should be employed. In modelling free molecular flows ($Kn > 10$), it is assumed that the intermolecular collisions are so rare that they can be completely neglected. This simplifies the simulation to just modelling molecular advection and hence, many related problems can be solved analytically. In the case of the transition flow regime ($0.1 < Kn < 10$) however, intermolecular collisions are important and as well, continuum methods are inapplicable. The Kn range associated with gas nano–flows, which are of interest in this thesis, mostly fall in this regime. In order to solve transition flow problems, atomistic modelling techniques known as direct simulation methods must be employed.

1.2 Numerical method

At the molecular scale there is an uncertainty associated with every measured quantity. This issue has been established by Heisenberg based on the fact that the probability of a definite value for a molecular quantity at those scales is zero; therefore, for every quantity,

[1]Different criteria can be found in the literature for continuum flow from 0.001 [1] to 0.01 [2]

there must be a differential range in which a certain value would be possible. Accordingly, in discrete methods, kinetics of the probability density function $f(\vec{r}, \vec{v}, t)$ of the molecules located at $\vec{r}$ with a velocity of $\vec{v}$ are analysed. The Boltzmann equation introduced by Ludwig Eduard Boltzmann (1844 – 1906) is the cornerstone of the kinetic theory of gases and describes the general distribution of $f(\vec{r}, \vec{v}, t)$ (the definition of f is given in (2.5)) for dilute gases: [1]

$$\frac{\delta}{\delta t}(nf) + \vec{v} \cdot \frac{\delta}{\delta \vec{r}}(nf) + \vec{F_b} \cdot \frac{\delta}{\delta \vec{v}}(nf) = \int_{-\infty}^{\infty} \int_{0}^{4\pi} n^2 (f^* f^*{}_1 - f f_1) v_r \sigma(v_r, \Omega) d\Omega d\vec{v_1} \tag{1.1}$$

where, σ is the collision cross–section and $\vec{F_b}$ represents external body forces. The left hand side of the Boltzmann equation describes effects of the molecular convection, while its right hand side describes effects of intermolecular collisions.

A direct solution for the Boltzmann equation is too costly and time consuming, especially when complicated phenomena like chemical reactions are involved. Therefore, different methods have been developed to reduce the required computational effort. Theoretical solutions are also very restricted to some simple cases, mostly for the free molecular regime. Generally, they simplify the Boltzmann equation either by linearization and simplification of the collision integral [3, 4], or by using distribution functions and Chapmann-Enskog expansion [5, 6]. Although these solutions are analytical, due to errors associated with linearizations and simplifications, they are not of adequate accuracy. In addition, final partial differential equations obtained from such methods still require numerical solution.

Full numerical solutions, on the other hand, can handle majority of problems with reasonable accuracy. A group of such numerical methods solve the Boltzmann equation directly by linearizing and discritizing it over a generated mesh distributed over the entire solution domain. Some of these methods split the Boltzmann equation into two parts: transport terms and collision terms. They treat the former just the same as the finite difference method and handle the latter using the Monte Carlo algorithm. Another old but efficient numerical scheme is the discrete ordinate method; in which, the molecular velocity is restricted to predefined values and directions [7, 8]. The most successful method of this group is the Lattice–Boltzmann method (LBM), which presents a different approach for

modelling both continuum and discrete fluid flows. However, due to the complicated perturbed derivation of the LBM, simulation of complex phenomena such as thermal radiation or chemical reaction becomes prohibitively difficult; especially, where steep gradients are present [9, 1].

The remaining type of numerical methods to solve the Boltzmann equation are categorized as direct simulations, which model molecular translations and collisions stochastically. Molecular Dynamics (MD) method and Direct Simulation Monte Carlo (DSMC) are the two commonly used direct simulation methods. In the MD method molecules occupy space and intermolecular forces are considered in detail. Using the resultant force exerted on each molecule, molecular translations are traced according to Newtons second law, and dynamic and kinematic relations. As can be inferred from the nature of the MD procedure, the intention is to mimic the actual molecular physics and geometry. Therefore, the number of simulating molecules for achieving reasonable accuracy and meaningful averages is high and not arbitrary. In fact, this number should be identical to those inside a cube with dimensions equal to one mean free path λ. Hence, this number is obtained from:

$$N_{MD} = n\lambda^3 \tag{1.2}$$

In standard conditions, this number is nearly 10^8 for a cubic domain with 30λ. The point is that the mean free path is proportional to ρ^{-1} and consequently $\lambda \propto n^{-1}$, and thus, $N_{MD} \propto n^{-2}$ and it can be seen that if the pressure is raised to 100 times its standard magnitude, the required number of molecules in the specified cube reduces to 10^4. The MD method, therefore, is suitable for higher pressures since the computation load is lower at those conditions. In the rarefied gas flow, however, working pressure is typically low and/or λ is comparable to the characteristic length of the domain; these conditions are not necessarily in favour of the MD method.

The DSMC method, on the other hand, is specially developed to stochastically model rarefied gas flows, where fundamental assumptions are based on low density gases and ideal gas relations. Molecules are modelled by so–called simulating particles (so–called particles throughout this thesis), which are assumed unaware of each other, unless there is a collision. The DSMC was introduced by G.A. Bird in 1963 and is known to be a remarkably successful tool in modelling complicated physical phenomena in rarefied gas flows. It is, in fact, the

only numerical method currently available to deal with high Kn rarefied gas flows [2]. The specifications and capabilities of the DSMC method get along well with the requirements of the current study and therefore, it is employed as the numerical method. Like all other numerical models, there are some drawbacks associated with DSMC : DSMC is generally considered a demanding numerical method and its computational time is much longer than conventional CFD methods even for a simple geometry flow. Due to the stochastic nature of the DSMC method, the results contain some statistical scatter. This reduces the quality of the results especially in low velocity flows where the order of the statistical scatter of a variable is close to its actual value. In such a case, the number of iterations required to decrease the statistical scatter to a reasonable level can be so high that DSMC method becomes inefficient. Moreover, as it will be shown in this work, an appropriate treatment of open boundary conditions has not been well defined yet, especially for gas mixtures, and using extended domains are still necessary to minimize the imperfections at the flow inlet/outlet boundaries.

1.3 Review of previous studies

The DSMC method is naturally able to deliver physical phenomena such as pressure and thermal diffusion which are difficult to capture by continuum transport models [10]. Therefore, DSMC has been undertaken by researchers for simulating gas flows in micro/nano–channels. Most of the studies, however, has been devoted to single component gas flows. One of the very first attempts is an inlet/outlet pressure boundary condition introduced by Ikegawa and Kobayashi [11]. They simulated a Poiseuille flow in the transition regime with a Kn range between 0.13 to 5 and verified mass flux results at different Knudsen numbers against experimental data. Their method of controlling pressure, however, uses flow information collected from the last time step which increases the instability and amplifies the statistical scatter. Piekos and Breuer [12] introduced a modified pressure boundary condition using the characteristic line method and substituting for the unknown variables at flow boundaries the corresponding weighted average values of the last several time–steps. They simulated gas flows in a parallel micro–channel in the slip and transition regimes and their findings demonstrate the intrinsic ability of DSMC to capture the non–equilibrium

phenomena at moderate to high Knudsen numbers. In the verification of their results with analytical data, small errors together with high fluctuations are observed. Liou et al. [13] and Wang et al. [14] improved the pressure boundary condition using gas dynamics relations and obtained accurate results with reasonably less statistical scatter even in the velocity field. They compared velocity slip from DSMC simulations with theoretical results for a range of Knudsen numbers $0.05 < Kn < 1$. In their work, the temperature distribution and the effect of Knudsen number on the heat transfer characteristics of such flows are also investigated. Wang et al. [15] introduced a constant heat flux boundary treatment scheme for DSMC modelling of micro–channel flows. Based on this method, the wall surface temperature is evaluated at each time step using the specified heat flux and the total energy (translational and internal) of the incident molecules.

Less focus has been devoted to multi–component gaseous flows in micro–channels although majority of applications are of this type. A proper implementation of the pressure boundary condition is especially a challenge at the flow boundaries. A simple workaround is leaving the boundary untreated. This reproduces the vacuum environment at the boundary causing considerable pressure drop and large stream velocities close to the boundary. Le and Hassan [16] applied this method at the outlet boundary in their study of the mixing process of CO and N_2 in a T-shaped micro–mixer. Wang and Li [14] studied the parallel mixing process of the same species in a planar channel. They imposed constant pressure at the outlet boundary, however, CO/N_2 species have almost the same molecular mass and diameter and therefore, the procedure used for single component flows can still be applied. Yan and Farouk [17] studied the flow of binary mixtures of He/Xe, He/Kr and He/Ar. They utilized the method originated by Piekos and Breuer [12].

Wang et al. [15] used mixtures of various species in their attempt to propose a constant heat flux boundary treatment. However, the inlet/outlet pressure ratio they applied was so high that the outlet velocity passes sonic threshold and hence, no molecule enters at the boundary; this way, no special treatment is required for the outlet boundary.

Working with individual molecules makes DSMC an efficient and flexible method for simulating gas mixtures flows exposed to chemical reactions. Bird [18] introduced a model based on the reactive cross section for simulating binary reactions. In that model, experimental kinetics in the form of the Arrhenius equation were translated into a probability,

by which some intermolecular collisions result in chemical reactions. Later on, Bird introduced an alternative model based on the collision energy and the vibrational energy levels of the reactant molecules participating in the collision [18]. The latter eliminates the dependency on experimental kinetics. Another method is called the Macroscopic Chemistry Method (MCM) introduced by Lilley and Macrossan [19]. In this method, instead of using the reactive cross section, mean values of species concentrations are directly substituted into the Arrhenius equation associated with each sub-reaction, and thus, chemical kinetics with a large number of sub-reactions and species can be modelled easier. However, as part of their procedure, it is required to artificially compensate the chemical potential of the reactants, by adding it in the form of internal or translation energy to the product molecules. This leads to irregular molecular velocities and results in instabilities for micro/nano–applications which have mostly low temperatures. All of the above mentioned methods, however, have been introduced for homogeneous gas reactions. Heterogeneous chemical reactions are seldom investigated by DSMC. Few reported studies, like Cercignani et al. [20], deal with simple dissociation reactions without catalytic effects.

1.4 Objectives and structure of the thesis

The main objective of this thesis is to develop a comprehensive DSMC code to simulate chemically reacting gaseous flows inside micro/nano–planar channels with greater focus on nano–scales using the least simplifying assumptions. The DSMC method and its algorithm is briefly described in Chapter 2. In addition, many parameters from gas dynamics and statistical mechanics required in understanding DSMC routines are explained in Section 2.1 in the same chapter. General forms of thermal and fluid dynamics boundary conditions used in DSMC are discussed in this chapter. The method introduced in this thesis for coupling heterogeneous reactions on the catalytic walls and the flow is also included.

The first step prior to modeling chemical reacting flows is to develop a code for simulating non–reacting multi–component micro/nano–flows and to verify the results in detail. In Section 3.2 of Chapter 3 the fluid dynamics and thermal results obtained from the DSMC code are verified against the solutions of the Navier-Stokes equations with

slip/jump boundary conditions for gaseous micro–flows in the slip flow regime. The results of this study have been published in the International Journal of Heat and Mass Transfer [21]. As stated before, proper implementation of flow boundary conditions, especially the pressure boundary condition is a challenge for modeling gas mixture flows using DSMC. Moreover, stream velocities are generally low in micro/nano–channel applications and therefore, upstream diffusion is important. This can carry the inaccuracies, produced by an inefficient outlet pressure boundary condition, upstream into the channel and affect the flow properties. Therefore, in Section 3.3 of Chapter 3 a through review of available pressure boundary conditions is presented and then an improved pressure boundary condition using the Chapman–Enskog distribution is introduced. It is shown that this new pressure boundary treatment can improve the accuracy of the results for high Kn and low inlet/outlet pressure ratio cases. The results of this section have been published in International Journal of Modern Physics C [22].

In Chapter 4, the procedure of modeling heterogeneous chemical reactions by DSMC is implemented and the achieved results are verified against Navier-Stokes equations with slip/jump boundary treatment. The chosen problem is the H_2/air gas mixture flow with a specified equivalence ratio in a planar micro–channel undergoing catalytic oxidation on platinum coated walls. It should be noted that the oxidation of H_2 undertaken in this study is an example and the general method of Chapter 4 is capable of modeling other surface reactions as long as their mechanism is known. The validated code is then used to study the same reacting flow under different geometrical and fluid dynamics conditions. This way, effects of the channel height, inlet mass flow rate, inlet and wall temperatures, and the equivalence ratio are investigated.

Finally in Chapter 5 conclusions are discussed and the possibilities for future works are suggested.

Chapter 2

Direct Simulation Monte Carlo (DSMC) method

As mentioned, conventional Navier-Stokes equations are only valid for continuum flows. They can also be used for simulating the bulk motion (outside the Knudsen layer) in the slip flow regime, taking advantage of slip/jump conditions to model the rarefaction effects which appear on the walls. For the rest of the Kn range, however, the flow is fully rarefied and atomistic modelling techniques must be employed.

The Direct Simulation Monte Carlo method satisfies the Boltzmann equation [23] using a stochastic approach and is applicable for a broad range of Kn from slip flow to free molecular flow. Although DSMC is computationally demanding, particularly in low velocity and low Kn flows, alternative methods [24] (e.g., Grad's 13-moment, linearised Boltzmann, extended lattice Boltzmann) have limitations on the Kn range and are not all flexible enough to include complex phenomena such as chemical reactions. Theoretically, there is no limitation on Kn for DSMC and this especially makes DSMC a proper method for modelling nano-scale flows. In addition, high Kn conditions are favourable for the DSMC algorithm and improves its efficiency at nano-geometries.

The DSMC algorithm is based on the collision theory in which, molecular movements and intermolecular collisions are the only calculations made for modelling a gas flow. The collision models have been under improvement since first versions of DSMC were published.

The simplest model is the Hard Sphere (HS) model in which post–collision velocities of a colliding pair of molecules have the same distribution as of two hard spheres with the same geometries and pre–collision specifications. This model has been improved to include the effects of short range forces and anisotropic scattering as seen in reality using a phenomenological approach. As a result some more realistic models have been introduced; Variable Hard Sphere (VHS) model by Bird [1], Variable Soft Sphere (VSS) model by Koura and Matsumoto [25, 26], and Generalised Hard Sphere (GHS) model by Hassan and Hash [27].

In case of an intermolecular collision, the internal energy is also exchanged as well as the translational energy. When introduced, the DSMC method was based on the Chapman-Cowling [28] gas kinetic theory. The strength point of Chapman-Cowlings theory in contrast to others, was taking the benefit of Larson-Borgnakke [29] procedure of intermolecular energy exchange during inelastic collisions. In addition, unlike other methods that devote their focus on modelling the collisions all theoretically in detail, Larson-Borgnakke model presented a phenomenological approach. This avoids most of the difficulties associated with storing data associated with the molecular orientation and rotational speed, and eliminates the need for complicated computations.

Many parameters are involved in the DSMC procedure, both from statistical mechanics and gas dynamics. A selected number of these parameters which are important in understanding the DSMC procedure are briefly explained in the next section.

2.1 Molecular magnitudes

Generally, any vector or scalar quantity which is a function of molecular speed $\vec{v}$ are considered as molecular properties [28]. These properties can be functions of time or position as well. As expected, molecular properties have erratic changes both in time and in space, which is due to the variations of the number of the molecules inside the considered volume during the time. Consequently, time average (average of a quantity over a relatively long period of time) and ensemble average (average over an indefinite number of calculation repetitions) are used to demonstrate a mean value. The average values or symbols presented in this thesis are ensemble averages unless otherwise stated.

An ensemble average value is generally defined as follows:

$$\bar{Q} = \Sigma Q / \Delta N \tag{2.1}$$

In which, ΣQ is the summation of any molecular quantity Q for a finite number of molecules ΔN which is calculated by $n\Delta V$ for a finite volume ΔV, and $\bar{Q}$ is the corresponding mean value. The integral form of ensemble averaging is:

$$\bar{Q} = \frac{1}{N} \int Q dN \tag{2.2}$$

The common classical model that generally expresses molecular interactions is the inverse power law model which describes the long range force between two molecules:

$$F = \kappa / r^n \tag{2.3}$$

in which, r is the distance between the center of the molecule.

There are two main assumptions that are essential for DSMC simulation of molecular collisions; first, the flowing gas is dilute i.e., the distance between two molecules is much greater than the molecules diameter, d. Second, the period of time for each collision can be neglected. The average volume occupied by a single molecule in a gas with a number density of n is:

$$\delta^3 = n^{-1} \tag{2.4}$$

Based on this definition, dilute gases can be recognized by the criterion of $\delta >> d$ (conversely $\delta/d > 7$ [30]).

According to uncertainties at molecular scales, each molecule is in a position between $\vec{r}$ and $\vec{r} + \vec{dr}$ with a velocity of $\vec{v} + \vec{dv}$. Hence, a probability distribution function can be defined for the number of molecules with a specific location and velocity as follows [1]:

$$dN = n f(\vec{v}, \vec{r}, t).dv.dr \tag{2.5}$$

in which dN is the number of molecules located between $\vec{r}$ and $\vec{r} + \vec{dr}$ and having a velocity between $\vec{v}$ and $\vec{v} + \vec{dv}$. The relative velocity of two molecules with velocities $\vec{v}_1$ and $\vec{v}_2$ is:

$$\vec{v}_r = \vec{v}_1 - \vec{v}_2 \tag{2.6}$$

Another important definition is for the thermal velocity given by:

$$\vec{v'} = \vec{v} - \vec{v}_0 \tag{2.7}$$

where, $\vec{v}_0$ represents the stream velocity vector. Nearly all intensive macroscopic quantities such as temperature, are directly related to the thermal velocity.

As stated previously, the simplest intermolecular collision model is HS in which, each molecule is assumed as a solid sphere with a diameter of d. Now, one can consider an imaginary circle around a molecule of *radius* d. A collision happens whenever the trajectory of another molecule crosses this circle. Such a circle is called total collision cross section σ_T which is equal to $\pi d^2/4$ for the HS model but in reality, σ_T depends on v_r as well. σ_T is an important quantity in the simulation of macroscopic properties of the flowing gas such as viscosity and diffusion coefficients. In the HS model, trajectories of deflected molecules come from a fixed center of scattering which makes all deflection angles equally likely. More realistic models are described in Section 2.2.3. Assuming HS for collisions of the molecules with uniform diameter, the average number of intermolecular collisions seen by each molecule in a time interval Δt is [1]:

$$\nu_f = n\overline{\sigma_T v_r} \tag{2.8}$$

Using the result of Equation (2.8), a simple relation can be derived for the mean free path λ as follows:

$$\lambda = \frac{\bar{v'}}{\nu_f} = \frac{1}{n\left(\overline{\sigma_T v_r}/\bar{v'}\right)} \tag{2.9}$$

In addition, the average period of time between two successive intermolecular collisions of one molecule known as mean collision time (Δt_c) is obtained from:

$$\Delta t_c = 1/\nu_f \tag{2.10}$$

Using the quantities defined so far, it is possible to evaluate the number of intermolecular collisions in a unit of volume during a unit of time as:

$$N_c = \frac{1}{2} n \nu_f = \frac{1}{2} n^2 \overline{\sigma_T v_r} \tag{2.11}$$

This relation is the base of the No Time Counter (NTC) DSMC method which will be explained later.

In the rest of this section, some expressions used in the final sampling step are presented. The pressure tensor $\underline{P}$ (the negative of the conventional stress tensor introduced in fluid mechanics) is defined as [1]:

$$\underline{P} = \rho \overline{\vec{v'}\vec{v'}} \tag{2.12}$$

Scalar pressure used in the transport equations is then defined as:

$$p = \frac{1}{3}\rho \overline{\vec{v'}^2} \tag{2.13}$$

Since heat transfer and chemical reactions are part of the current study, the quantities required for non–isothermal analysis are presented here. The kinetic energy of a molecule due to its translational motion with its thermal velocity is:

$$E_{tr} = \frac{1}{2} m \overline{v'^2} \tag{2.14}$$

The distribution of the molecular energy based on the Larsen–Borgenakke theory is as follows [1]:

$$f_{E_{tr}} \propto {E_{tr}}^{3/2-\omega} \exp\{-E_{tr}/(kT)\} \tag{2.15}$$

It is common to denote the quantity E_{tr}/m by e_{tr} called specific translational energy. Combining equations Equations 2.13 and 2.14 results in:

$$p = \frac{2}{3}\rho e_{tr} \tag{2.16}$$

Comparing the result with the ideal gas relation $p = \rho RT$ which is applicable for equilibrium conditions, it is possible to define a translational kinetic temperature T_{tr} as:

$$e_{tr} = \frac{3}{2} R T_{tr} \tag{2.17}$$

Internal energy temperature is defined in the same way for diatomic and poly-atomic molecules. Different modes of internal energy like rotational and vibrational energies are possible for a molecule according to its structure and number of atoms. The distribution of E_{int} is written as [1]:

$$f_{E_{int}} \propto {E_{int}}^{\zeta/2-1} \exp\{-E_{int}/(kT)\} \tag{2.18}$$

Similar to the expression of translational energy (Equation 2.17) an internal energy temperature T_{int} can be defined in such a way that:

$$e_{int} = \frac{1}{2}\zeta R T_{int} \tag{2.19}$$

where $e_{int} = E_{int}/m$. In equilibrium conditions; all internal and translational temperatures are equal for the molecules located in a dV. For gases in non-equilibrium conditions the measurable temperature at a point is defined as [1]:

$$T = (3T_{tr} + \zeta T_{int})/(3 + \zeta) \tag{2.20}$$

In molecular approach, heat flux is the summation of translational energy ($\frac{1}{2}\rho v'^2 \vec{v'}$), and internal energy ($\rho e_{int}\vec{v'}$) of the molecules passing a unit area of a surface; therefore:

$$\vec{q} = \frac{1}{2}\rho \overline{v'^2 \vec{v'}} + \rho e_{int}\vec{v'} \tag{2.21}$$

It is worth to note that $3p = \rho v'^2$ from Equation 2.13, so that the first term in the above equation is related to the pressure work on moving molecules.

All quantities defined above are for single–component gases. the equivalence of some of these quantities are presented for multi–component gas mixtures, due to their importance in this study. Total amount of a gas mixture molecules located in a unit of volume is:

$$n = \sum_{i=1}^{s} n_i \tag{2.22}$$

where, s is the total number of species. As such, the density of a gas mixture is evaluated from:

$$\rho = \sum_{i=1}^{s} n_i m_i = n\overline{m} \tag{2.23}$$

If species 1 and 2 are selected, then the effective molecular diameter is considered as:

$$d_{12} = (d_1 + d_2)/2 \tag{2.24}$$

The corresponding collision cross section is:

$$\sigma_{T12} = \pi d_{12}^2 \tag{2.25}$$

If it is considered that molecules of species 1 are colliding with those of species 2, the mean collision rate of the selected pair of species can be obtained from:

$$\nu_{f_{12}} = n_1 \overline{\sigma_{T12} v_{r12}} \tag{2.26}$$

where, $\sigma_{T12} = \pi d_{12}^2$ and in the HS model, $d_{12} = (d_1 + d_2)/2$. The collision rate for each species can be determined by summation of Equation (2.26) over all species:

$$\nu_{f_i} = \sum_{j=1}^{s} \left(n_j \overline{\sigma_{Tij} v_{rij}} \right) \tag{2.27}$$

The same as single gas, the mean free path is calculated from Equation 2.9 by substituting mean collision rate from equation Equation 2.27:

$$\lambda_i = \left(\sum_{j=1}^{s} \left(n_i \overline{\sigma_{Tij} v_{rij}} / \overline{v'_i} \right) \right)^{-1} \tag{2.28}$$

The total number of collisions per unit time and per unit volume can then be obtained from:

$$N_c = \frac{1}{2} n \nu_f = \frac{1}{2} \sum_{i=1}^{s} \left(n_i \nu_{f_i} \right) \tag{2.29}$$

The mean values of some flow variables used in sampling routines are presented here. The stream velocity is obtained from [31]:

$$\vec{v_0} = \frac{1}{\rho} \sum_{i=1}^{s} \left(m_i n_i \overline{\vec{v_i}} \right) \tag{2.30}$$

In which, $\overline{\vec{v_i}}$ is the average of molecular velocities for the species i. The pressure tensor and scalar pressure are:

$$P_{xy} = \sum_{i=1}^{s} \left(\rho_i \overline{v'_{xi} v'_{yi}} \right) \tag{2.31}$$

$$p = -\frac{1}{3} \sum_{i=1}^{s} \left(\rho_i \overline{v'^2_i} \right) \tag{2.32}$$

where, x and y are components of the vector $\vec{v'}_i$ and xy indicates the components of the stress tensor $\underline{\sigma}$. The mean translational temperature for the mixture is:

$$\frac{3}{2}kT_{tr} = \frac{1}{2}\sum_{i=1}^{s}\left\{(n_i/n)m_i\overline{v'^2_i}\right\} \tag{2.33}$$

For diatomic and polyatomic gases, a definition similar to Equation 2.19 is applicable for each species. For the gas mixture, mean internal degrees of freedom is defined, so that the definition of the internal energy temperature is:

$$\frac{1}{2}\bar{\zeta}RT_{int} = \sum_{i=1}^{s}\frac{n_i}{n}e_{int_i} \tag{2.34}$$

Similarly, a component of the heat flux is expressed as:

$$q_x = \sum\left[\frac{1}{2}\rho_i\overline{v'^2_i v'_{xi}} + \rho_i e_{int_i}\overline{v'_{xi}}\right] \tag{2.35}$$

2.2 DSMC algorithm

DSMC decouples the Boltzmann equation (Equation (1.1)) into two parts: molecular movement and intermolecular collisions. These parts are respectively applied to simulating particles each representing a specified number, S_n, of real molecules. In the DSMC method, the domain is first partitioned into some virtual cells which are used to trace the movement of simulating particles. The simulating particles are initially spread over the cells and their initial velocities are assigned from the equilibrium distribution. New particles enter at the inlet and outlet boundaries and the simulating particles move according to their existing velocities during the time step Δt. The time step must be chosen in such a way that a molecule with the maximum molecular speed cannot traverse a cell face at once. The maximum molecular speed is considered as three times the most probable molecular thermal speed V_{mp} of the species involved [1]. The expression of V_{mp} is as follows:

$$V_{mp} = \left(\frac{2kT}{m}\right)^{-1/2} \tag{2.36}$$

where, k is the Boltzmann constant and m denotes the molecular mass. Those molecules which collide with the walls are reflected according to the condition considered for the walls. After finishing the movements, a specific number of pairs from the molecules in each cell are then randomly selected for binary collisions. Following Bird's NTC methodology [1], intermolecular collisions take place between some of the pairs according to a specified probability. The post-collision particle velocities and translational directions are then calculated and saved.

After a specific number of movement and collision loops, velocity, translational energy, and internal energy of the simulating particles inside each cell are sampled and thus, one iteration is completed. This iteration is repeated for a specific number, and then the values of number density, pressure, mass averaged stream velocity and temperature for each cell are calculated as final outputs using the information sampled during the solution and the equations provided in Section 2.1. These quantities are also calculated for implementation of the inlet and outlet boundary conditions as required, similar to the DSMC-IP procedure [32]. The cell-based data preservation is known as an efficient way to reduce statistical scatter [32]. As outlined above, DSMC algorithm consists of four steps (see Figure 2.1):

1. Initialization
2. Molecular movement
3. Intermolecular collision
4. Sampling and output

2.2.1 Initialization

Initially, the domain is partitioned into virtual cells which are demonstrated in Figure 2.2. The cell based scheme is an efficient method of tracing incremental movement of large number of particles which is used in the DSMC. The cell side length, Δx, must be a fraction of the mean free path. As it was noted by Bird [1], Δx should be less than $\lambda/3$.

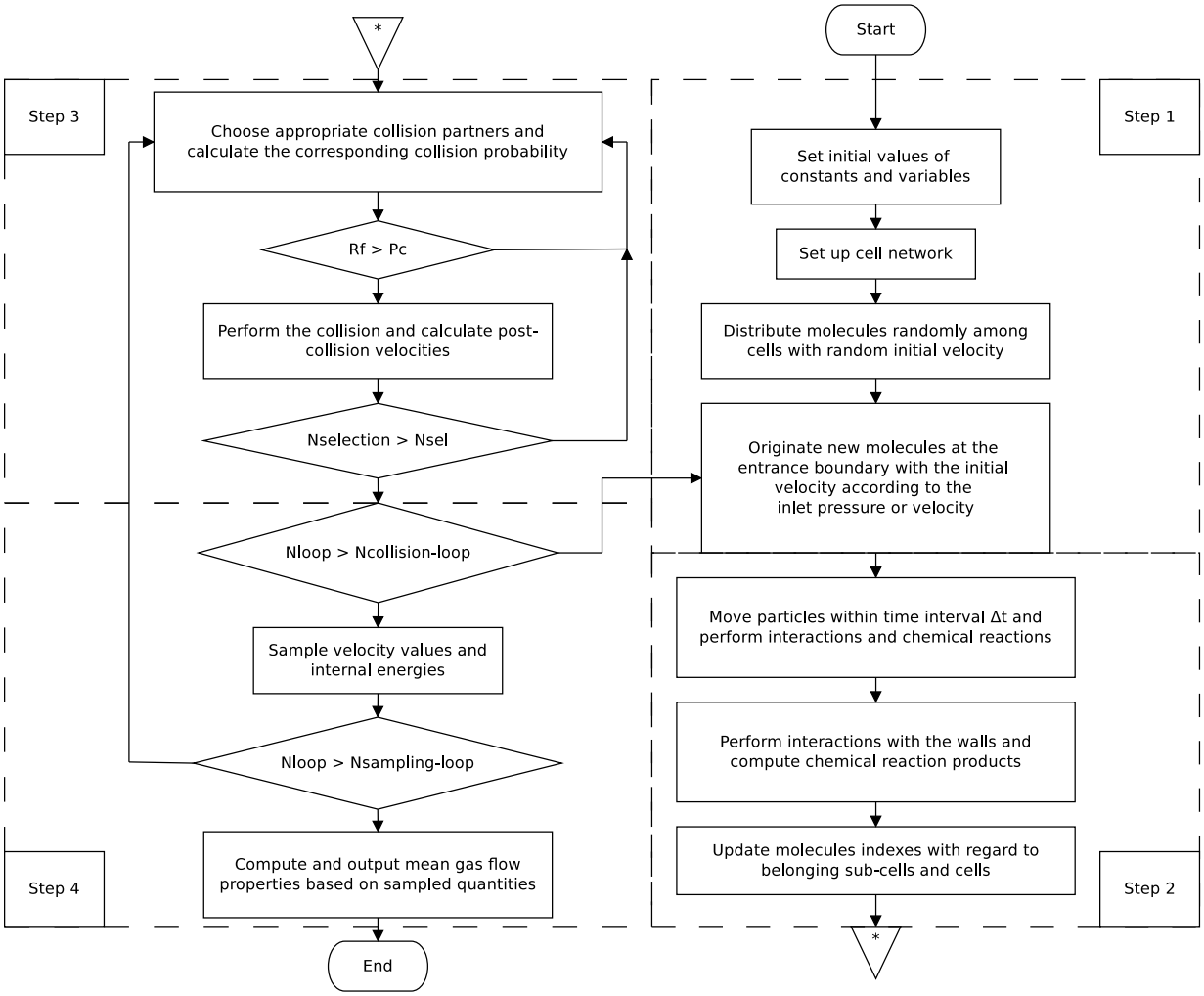

Figure 2.1: The flowchart of the DSMC algorithm

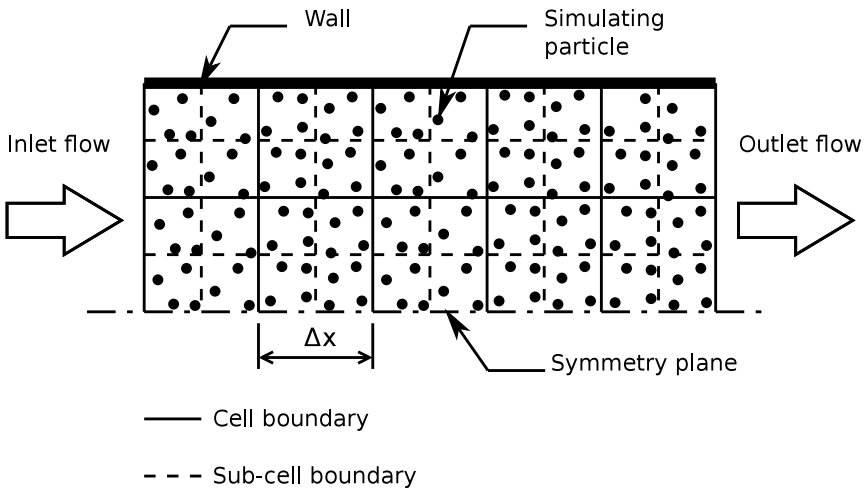

Figure 2.2: The solution domain initially divided into cells and sub-cells, and simulating particles are distributed randomly.

The maximum limit of Δt is calculated based on Δx as follows:

$$\Delta t < C\Delta x / V_{mp} \tag{2.37}$$

The value of C is normally taken equal to 0.1 [33]. In the modified version of the DSMC (1994 & 2007), each cell is also divided into uniform sub-cells (see Figure 2.2). This way, binary collision partners are chosen from the molecules inside each sub–cell and therefore, they are closer to each other and more likely to collide. Furthermore, sub-cells are not considered in sampling steps for the sake of saving computation time and memory and hence, this approach is superior to using finer cells [34]. At the beginning, simulating molecules are randomly spread out among the cells, with an equilibrium velocity distribution (Maxwellian velocity distribution) as follows:

$$f^{(0)} = V_{mp}^{-3}\pi^{-3/2}\exp\left(-v'^2/V_{mp}^2\right) \tag{2.38}$$

All of them are numbered and their positions are traced by the corresponding sub-cell and the cell numbers they are in. Sampling a random value from a distribution is the basis for the Monte Carlo methods which is demonstrated in Appendix B. Using this sampling

procedure, values of velocity components for 2D problems are initialized as:

$$\begin{aligned} A &= \sqrt{-ln(R_{f1})} \\ \theta &= 2\pi R_{f2} \\ v_x &= A\cos(\theta) \\ v_y &= A\sin(\theta) \end{aligned} \tag{2.39}$$

where R_{f1} and R_{f2} are two randomly generated numbers between 0 and 1. In this step initial values of species mole fractions are also set to the specified values at the inlet of the channel.

2.2.2 Molecular movement

The simulating particles are moved with regard to their existing velocities during the time interval Δt. Interactions with the walls are performed in this step as well which is described in Section 2.3. In the cell based scheme, following the moving procedure, there is an indexing routine which sorts the molecule numbers in cells and sub-cells. Algorithm of such a procedure is simple in the case of a single gas flow; however, for gas mixtures, numbering logic must support binary collisions of both similar and different species.

2.2.3 Intermolecular collisions

In this step, first, pairs of molecules are selected randomly within sub–cells. The total number of collisions in a cell during Δt simply equals to $N_c \Delta t$; where, N_c is obtained from Equation 2.11. The number of selected pairs, however, should be higher since not all of the selected pairs collide with each other. Therefore, in the No Time Counter method (NTC) proposed by Bird [1], this number is calculated according to the collision probability P_c. P_c is based on the product of relative velocity and collision cross section which implies a cylinder with the cross section σ_T swept by a molecule towards another, so that the length of the cylinder will be $v_r \cdot \Delta t$. The collision happens whenever a molecule exists in the swept volume, $\sigma_T v_r \cdot \Delta t$. Therefore, the collision probability P_c is obtained from [1]:

$$P_c = v_r \sigma_T / (v_r \sigma_T)_{max} \tag{2.40}$$

The initial value of $(v_r\sigma_T)_{max}$ is set to a suitably large magnitude and is updated during the solution. The total number of collision during one Δt , therefore, is calculated from Equation (2.29). In the NTC method, this value is divided by the collision probability, Equation 2.40, to obtain the total number of binary pairs which should be considered to account for the actual number of binary collisions. The result is:

$$N_{sel} = \frac{1}{2} N_{cell} \overline{N}_{cell} S_n (v_r \sigma_T)_{max} \Delta t / V_{cell} \tag{2.41}$$

in which, S_n is the number of real molecules represented by a simulating particle, N_{cell} is the average number of simulating particles in a cell and $\overline{N}_{cell}$ is the time average of the N_{cell}. Equation 2.41 reveals that N_{sel} varies linearly with N_{cell}, using the relation ${N^2}_{cell} = N_{cell}\overline{N}_{cell}$. This is one of the main advantages of Bird's NTC method. The collision probability P_c is then checked for each selected pair and the collision happens if a random number R_f is larger than P_c. Values of post-collision translational and internal energies are then required to be evaluated for successful collision pairs. This is done through the collision model employed in the simulation.

Elastic binary collisions

A binary collision is elastic if only translational energy is exchanged during the collision. In this case, to obtain post–collision velocities, momentum and energy conservation equations are to be solved; however, two extra equations are required to calculate all velocity components. Hence, the azimuth angle, ϵ (see Figure 2.3), and the center distance, b, are usually prescribed by a collision model. As it was mentioned in Section 2.1, the HS model cannot express the physics of the collision completely and therefore, VHS (Variable Hard Sphere) and VSS (Variable Soft Sphere) models have been introduced. VHS is a generalized form of the HS model with the same fixed center of scattering but variable diameter d. In the VHS model, d is not constant but a function of the v_r. Such a relation is of this form [31]:

$$\sigma_T / \sigma_{T,ref} = (d/d_{ref})^2 = (v_r/v_{ref})^{-2\zeta} \tag{2.42}$$

The reference values of d_{ref} and $\sigma_{t,ref}$ are specified at a reference relative velocity, v_{ref}. In this model b is related to the deflection angle χ as:

$$b = d \cdot \cos(\chi/2) \tag{2.43}$$

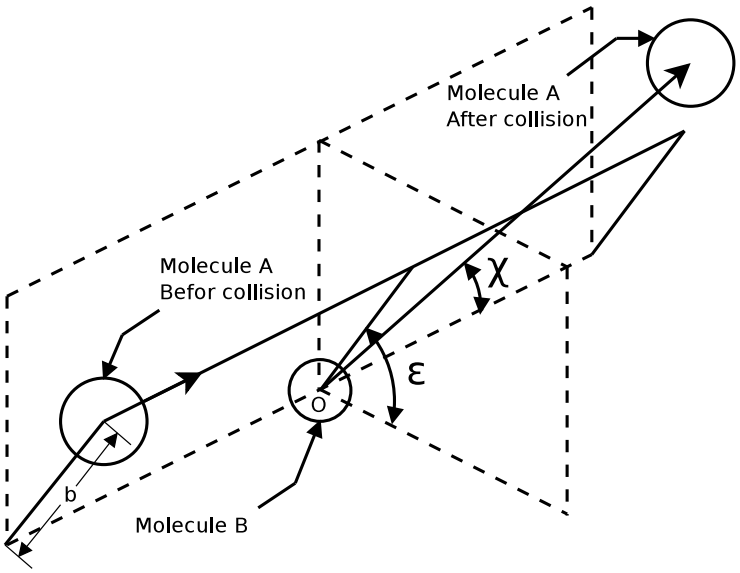

Figure 2.3: Demonstration of VHS parameters in molecules A and B collision.

The deflection angle is then calculated from $\cos(\chi) = 2(b/d)^{2/\alpha} - 1$. In the above relation d is the effective diameter and thus, a collision takes place if the fraction b/d falls within 0 and 1. Theoretically, any choice in the range of 0 to 1 is probable for the quantity b/d, as a result, in the Monte-Carlo methodology a random number will be chosen in this range and accordingly, the angle of deflection is calculated from:

$$\cos(\chi) = 2(R_f)^2 - 1 \tag{2.44}$$

where R_f is a random number in the range 0 to 1. In addition the angle between the collision plane and the reference plane, ϵ, can vary between 0 and 2π; therefore, $\epsilon/2\pi$ falls within 0 and 1 and is treated similar to b/d as:

$$\epsilon = 2\pi R_f \tag{2.45}$$

The collision cross section of VHS model is independent of deflection angle χ. Therefore, all reflection angles are of the same probability (fixed center of scatter) so that the orientation of the reference plane is not important. In such a condition, it is preferred to consider the x axes parallel to the direction of $\overrightarrow{v_r}$ and one of the other axes is placed in

the collision plane. According to Figure 2.3 and using momentum and energy balances of the colliding molecules, the magnitudes of the post–collision velocities for the VHS model are obtained as [31, 1]:

$$\begin{aligned} v^*_{rx} &= v_r \cos\chi \\ v^*_{ry} &= v_r \cos\epsilon \cdot \sin\chi \\ v^*_{rz} &= v_r \sin\epsilon \cdot \sin\chi \end{aligned} \tag{2.46}$$

Here, v_r represents the pre-collision and v^*_r represents the post–collision relative velocities.

The VHS model does not follow the inverse power law for modelling short range forces due to its fixed scattering center. Therefore, Koura and Matsumoto [25] made the following modification (the VSS model):

$$b = d \cdot \cos^{\alpha}(\chi/2) \tag{2.47}$$

In the VSS model both the diameter d and the exponent α are obtained from the inverse power law model. This way, a phenomenological method is presented for obtaining physical scattering deflection angles. Magnitudes of α depend on temperature and molecular properties of the collision partners. In the VSS model, a reference plane is fixed in an arbitrary position for all collision calculations. This plane is usually chosen normal to one of the global axes. Consequently, the deflection angle is sampled from:

$$\cos(\chi) = 2(R_f)^{2/\alpha} - 1 \tag{2.48}$$

and the velocities components are given by:

$$\begin{aligned} A &= \cos\chi \\ B &= \sin\chi \\ C &= \cos\epsilon \\ D &= \sin\epsilon \\ E &= \sqrt{v^2_{ry} + v^2_{rz}} \\ v^*_{rx} &= Av_{rx} + E \cdot B \cdot D \\ v^*_{ry} &= Av_{ry} + (C \cdot |v_r| v_{rz} - D \cdot v_{rx} v_{ry})\, B/E \\ v^*_{rz} &= Av_{rz} - (C \cdot |v_r| v_{ry} + D \cdot v_{rx} v_{rz})\, B/E \end{aligned} \tag{2.49}$$

Due to computational demand of VSS model, it is used only if $\alpha - 1 > 10^{-3}$; otherwise, VHS model is preferred. Elastic collisions are limited mostly to single atomic molecules

which have just one internal degree of freedom, $\zeta = 1$. Nevertheless, diatomic and poly-atomic molecules are always involved in chemically reacting flows. During collisions of such molecules internal energy is exchanged as well as translational energy.

Inelastic binary collisions

During inelastic collisions, there is an exchange of energy between both translational and internal modes. In order to maintain equilibrium conditions, energy must be distributed appropriately among these modes. The Larson–Borgnakke redistribution model is an effective method for this purpose and is undertaken in DSMC. Translational and internal energy distribution functions are presented in Equations 2.15 and 2.18 respectively. The total collision energy is the sum of translational and internal energies of both molecules. It can be shown that the probability ratio of a certain amount of translational energy [1] is:

$$\frac{P}{P_{max}} = \left\{ \frac{\zeta + 1/2 - \omega}{3/2 - \omega} \left(\frac{E_{tr}}{E_c} \right) \right\}^{3/2-\omega} \left\{ \frac{\zeta + 1/2 - \omega}{\zeta - 1} \left(1 - \frac{E_{tr}}{E_c} \right) \right\}^{\zeta - 1} \tag{2.50}$$

With regard to the form of the above relation, Bird introduced a phenomenological form of Larson–Borgnakke model, applicable for general poly-atomic energy interchange, based on Pullins theory [35]. Generally, total number of internal degrees of freedom for both collision partners is:

$$\Sigma\zeta = (5/2 - \omega_{12}) + \zeta_{rot,1}/2 + \zeta_{rot,2}/2 + \Sigma\zeta_{v,1}/2 + \Sigma\zeta_{v,2}/2 \tag{2.51}$$

It was stated in Section 2.1 that in the inverse power law model, viscosity varies with temperature as:

$$\mu \propto T^{\omega_{12}} \tag{2.52}$$

where $\omega_{12} = \frac{1}{2}(\eta + 3)/(\eta - 1)$ and η is the exponent of Equation 2.3. If $\Sigma\zeta$ is divided into two parts, $\Sigma\zeta_a$ and $\Sigma\zeta_b$, the distribution of energy between them according to Larsen–Borgnakke methodology is:

$$f\left(\frac{E_a}{E_a + E_b}\right) = f\left(\frac{E_b}{E_a + E_b}\right) = \frac{\Gamma(\Sigma\zeta_a + \Sigma\zeta_b)}{\Gamma(\Sigma\zeta_a)\Gamma(\Sigma\zeta_b)} \left(\frac{E_a}{E_a + E_b}\right)^{\Sigma\zeta_a - 1} \left(\frac{E_b}{E_a + E_b}\right)^{\Sigma\zeta_b - 1} \tag{2.53}$$

By integrating the last equation from zero to one with respect to the variable $E_a/(E_a + E_b)$, the following result is obtained for the mean value of E_a which is distributed equally between its all degrees of freedom:

$$\overline{E_a} = \frac{\Sigma\zeta_a}{\Sigma\zeta_a + \Sigma\zeta_b}(E_a + E_b) \tag{2.54}$$

The Larsen–Borgnakke method allows redistribution to be brought about in successive steps. Consequently, the rotational energy redistribution can be analysed independently. To redistribute rotational energy, $\Sigma\zeta_b$ is set to the total translational degrees of freedom:

$$\Sigma\zeta_b = 5/2 - \omega_{12} \tag{2.55}$$

Unlike the original Larsen–Borgnakke method, a fraction of collisions, Ω, is assumed to be *completely* inelastic. The fraction Ω is also called collision number which is a second order function of macroscopic temperature in real gases. A random number, R_f , is generated and if $1/\Omega > R_f$, the rotational energy is to be redistributed. Such a criterion must be checked for both colliding molecules separately, since it is possible that rotational energy redistribution takes place only in one of the partners. In this condition, the chosen molecule rotational degrees of freedom is added to $\Sigma\zeta_a$; so that, all degrees of freedom from which energy of collision is to be redistributed to $\Sigma\zeta_a$, are stored in $\Sigma\zeta_b$. Moreover, the energy of collision is translational energy plus total rotational energy of one or both interacting molecules (depending on the redistribution condition). Now, it is required to calculate the ratio $E_a/(E_a + E_b)$. Following the Monte-Carlo procedure, the probability of an amount of energy equal to E_a is associated with $\Sigma\zeta_a$. This quantity is obtained from Equation (2.57) as:

$$\frac{P}{P_{max}} = \left(\frac{\Sigma\zeta_a + \Sigma\zeta_b - 2}{\Sigma\zeta_a - 1}\left(\frac{E_a}{E_a + E_b}\right)\right)^{\Sigma\zeta_a - 1}\left(\frac{\Sigma\zeta_a + \Sigma\zeta_b - 2}{\Sigma\zeta_a - 1}\left(1 - \frac{E_a}{E_a + E_b}\right)\right)^{\Sigma\zeta_b - 1} \tag{2.56}$$

As it is not possible to get inverse from the last equation (in order to have a straight forward relation for the $E_a/(E_a + E_b)$ ratio), an acceptance-rejection procedure is applied which is explained in Appendix B. In such a procedure, a random number R_{f1} is generated and P/P_{max} is calculated by substituting R_{f1} in place of the ratio $E_a/(E_a + E_b)$ in equation Equation (2.56). Then R_{f1} is accepted if $P/P_{max} > R_{f2}$; in which, R_{f2} is a second random number between zero and one.

In the special case of just two internal degrees of freedom for rotational energy, the ratio $E_a/(E_a + E_b)$ is obtained easier from the following relation:

$$\frac{E_a}{E_a + E_b} = 1 - {R_f}^{1/\Sigma\zeta_b} \tag{2.57}$$

After calculating the energy ratio, E_a is determined using the accepted R_{f1} and then the relative translational energy is achieved correspondingly from:

$${E^*}_{tr} = E_{tr} + E_{rot} - {E^*}_{rot} \tag{2.58}$$

Having ${E^*}_{tr}$, the new relative velocity after the collision is calculated from:

$$v_r = \sqrt{2 \cdot {E^*}_{tr}/m_r} \tag{2.59}$$

The directions of the post velocities are obtained from the model of the collision (VHS or VSS).

The temperature required for vibrational degrees of freedom is very high and is far beyond the maximum temperatures likely to occur in micro–reactor applications. Therefore, this mode of internal energy is not considered in the present work.

2.2.4 Sampling and output

After each specified number of collision loops, a sampling process is applied, in which molecular velocities are sampled and stored for further mean–value computations. Higher number of sampling during the solution will result in lower statistical scatter and smoother results. Mean values of flow data are then retrieved as outputs after a specific number of sampling procedure. In this regard, equations of Section 2.1 are used. For velocity components equation Equation (2.30) and, for translational and rotational temperatures equations Equation (2.33) and Equation (2.34) are used. The overall temperature is then calculated from:

$$T = (3T_{tr} + \overline{\zeta_{rot}}T_{rot} + \overline{\zeta_v}T_v)/(3 + \overline{\zeta_{rot}} + \overline{\zeta_v}) \tag{2.60}$$

where, ζ_{rot} and ζ_v are mean internal degrees of freedom for rotational and vibrational degrees of freedom.

2.3 Boundary conditions

2.3.1 Surface interactions

During the molecular movement step, some molecules, adjacent to a wall surface, will cross the prescribed wall and are thus positioned outside of the domain. These molecules are considered as those which have collided with the wall. Upon collision, a portion of incident molecules penetrate into the wall pores. After successive reflections, these molecules leave the surface in a direction independent of the incident trajectory. Therefore, it is common to consider a fraction of the molecule–surface collisions to have diffuse reflection in which the reflected molecules move along trajectories with random directions. The procedure, described in Appendix B, is employed to generate random reflection velocity components. The rest of molecules reflect specularly, where the normal component of the incident velocity is just reversed while the tangential components remain unchanged. The fraction of the molecules reflected diffusely to the total number of incident molecules is called the velocity accommodation coefficient σ_v. As it is mentioned by Bird [1], examinations on smooth metallic surfaces have proved that incident molecules undergo fully diffuse reflections.

2.3.2 Constant surface temperature

In this work, thermally diffuse reflection is considered at the wall surfaces, i.e. the thermal accommodation factor σ_{th} is set to one which is reasonable for most metallic surfaces [1, 31]. Hence, both translational and internal temperatures of the reflected molecules are set equal to the wall temperature, T_w. Translational temperature is adjusted by calculating $V_{mp} = \sqrt{2kT_w/m}$ using the wall temperature and substituting it in the Maxwellian distribution for sampling velocity components of the reflected molecule. This process is identical to the one explained in Appendix B.

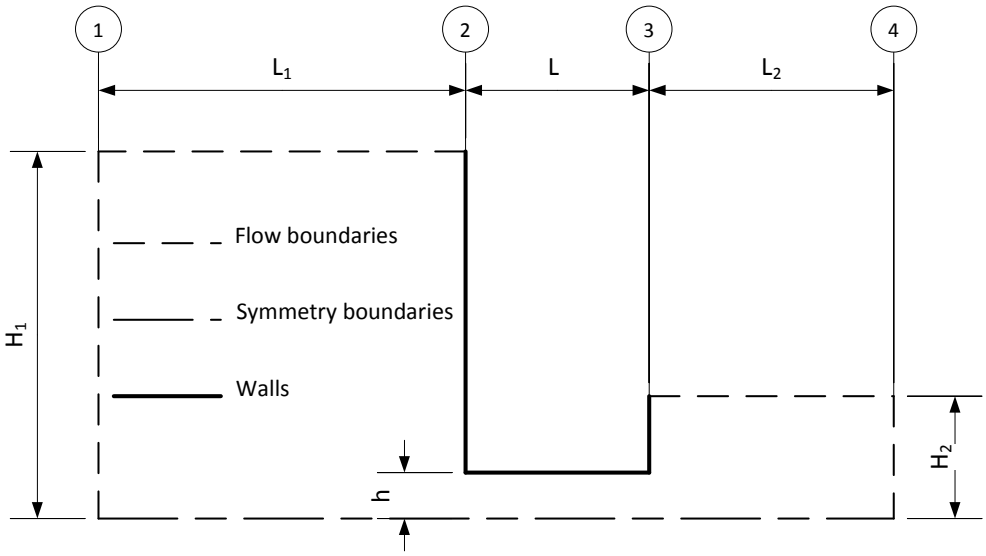

Figure 2.4: A channel connected to an inlet and an outlet reservoirs

2.3.3 Inlet and outlet boundary conditions

Two different inlet flow boundary conditions are employed in this work: (1) Constant pressure boundary condition, which is adopted in Chapter 3 in order to be consistent with another DSMC reference problem against which our results are compared. The details of implementing this boundary condition are described in Section 3.2. (2) The constant mass flow, which is adopted in Chapter 4 in order to be consistent with the inlet boundary condition of the Navier–Stokes solution used for validation of reacting flow results. This way, velocity and pressure profiles are automatically built up at the entrance of the channel.

The above mentioned boundary conditions are applied right at the entrance of the channel; however, it should be noted that inlet/outlet flow conditions are generally controlled by reservoirs (see Fig. 1.1) in most micro-channel applications. In these cases, the flow–structure interactions between the flow and the channel entrance affect the velocity and pressure profiles across the inlet. Therefore, the value and the distribution of the variable considered as the boundary condition will be different at the inlet cross section of the channel and far from it inside the reservoir. It has been shown that this effect depends on

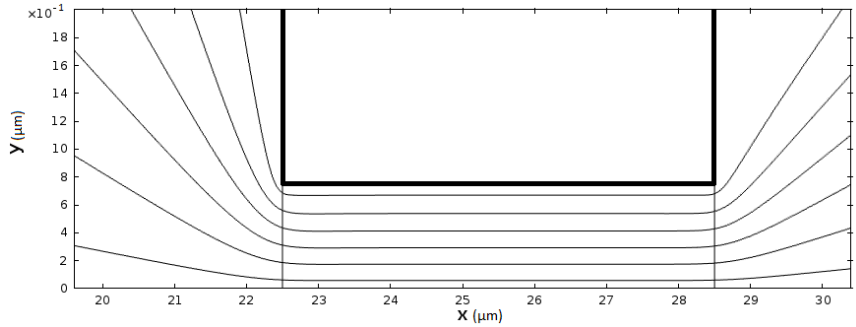

(a) P_1=1.2bar

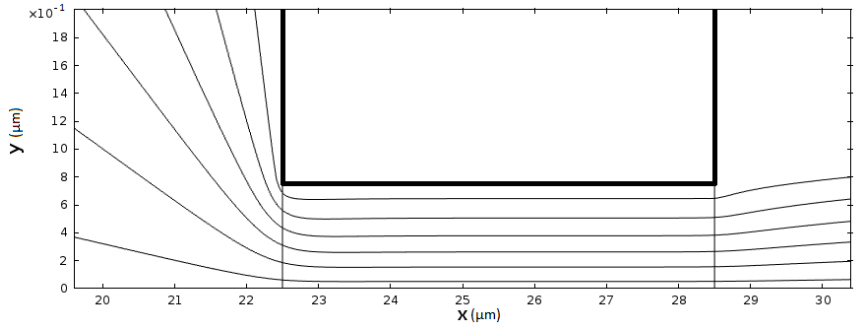

(b) P_1=3.0bar

Figure 2.5: Streamlines for cases (a) P_1=1.2bar, and (b) P_1=3.0bar

the flow velocity and rarefaction (Knudsen number) and is magnified as the flow velocity (pressure ratio) increases [36, 37]. For low speed (low Mach number) flows the effect of the reservoir on the entrance is small and therefore, many researchers have applied the inlet flow condition at the boundary [12, 38, 14] since an enormous computational effort is required for modeling a reservoir. In order to have an estimate of such a difference for a typical flow of the present work, a channel connected to inlet and outlet reservoirs is considered as shown in Figure 2.4. The channel geometries are considered as 2h=1.5μm and l=6μm and the geometries of the reservoirs are the same as those suggested in [36] (H_1=L_1=30h, H_2=10h and L_2=20h). The pressure at section 4 (P_4; this section includes both horizontal and vertical flow boundaries of the outlet reservoir) is kept at atmospheric value and two different pressures are applied at section 1 (P_1; this section includes both

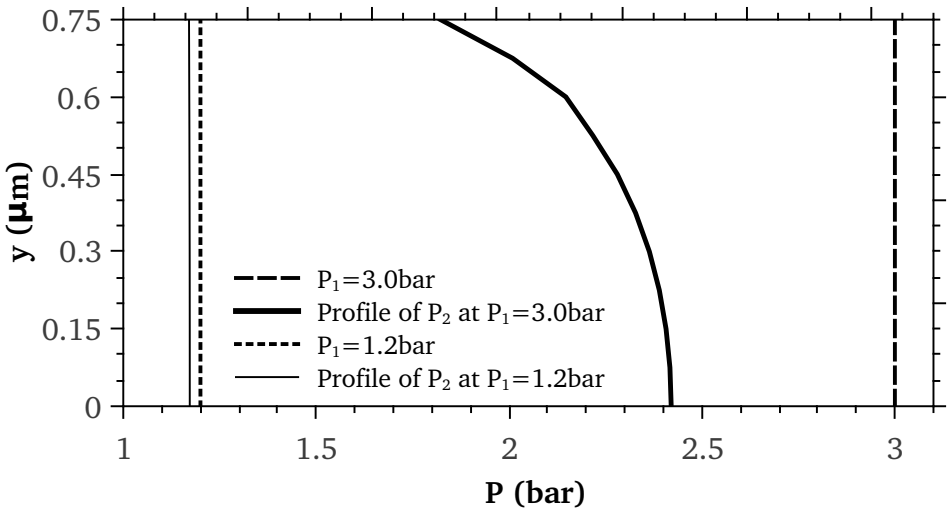

Figure 2.6: Pressure profiles at the inlet of the channel (section 2 of Figure 2.4) and the pressure value imposed at the inlet of the reservoir (section 1 of the same figure) for P_1=1.2bar and P_1=3.0bar

horizontal and vertical flow boundaries of the inlet reservoir): P_1=1.2bar in order to produce a low speed flow similar to the cases studied in this work and P_1=3bar for producing a high speed flow. The resulting streamlines are shown in Figure 2.5. As expected, the stream lines converge at the inlet of the channel to comply with the flow geometry. The change in the direction of the flow (curvature of streamlines) at the entrance of the channel causes gradients of velocity and the pressure across the channel inlet. These gradients become larger by increasing the flow velocity. Figure 2.6 shows the pressure profiles at the inlet of the channel (section 2 of Figure 2.4) and compares them with the pressure values imposed at the inlet of the upstream reservoir (section 1 of the same figure). As observed, the pressure difference is less than 3% for P_1=1.2bar whereas for P_1=3bar the maximum difference is about 40%. Similar results have also been reported in [36] in which the difference between the pressure inside the reservoir and the pressure at the inlet of the channel is about 5% for the flow specifications close to a high speed case of the present work (for example, Case 14 in Table 4.2). Furthermore, the pressure profile for P_1=1.2bar shown

in Figure 2.6 is closer to a uniform distribution compared with P_1=3.0bar. These results suggest that if the flow geometry includes a reservoir at the inlet, applying the boundary condition right at the inlet of the channel for low speed (low Mach number) flows could lead to a maximum error of about 5%; however, this error is considerable for high velocity flows and therefore, such a reservoir should be modeled. It should be noted that in the current study, inlet conditions are applied at the inlet of the channel since the focus is on the method of modeling the chemical reacting flows. Moreover, flow velocities of the cases under study in the present work are all in the low Mach number range ($Ma < 0.2$). Nevertheless, the method of simulating reacting flows introduced in Chapter 4 can be used for different geometries and flow speeds.

Another observation from Figure 2.5 is that at the outlet of the channel (section 3 of Figure 2.4) streamlines diverge into the reservoir affecting distributions of the pressure and the velocity. This effect is obviously stronger for lower velocity case and therefore, applying the outlet boundary condition at the outlet of the channel requires special considerations. This issue has been addressed in some studies [12, 38]. Since flow velocities of the case studies in this work are in the low Mach number range, the implementation of the outlet pressure boundary conditions in DSMC is discussed in detail in Section 3.3.

The inlet/outlet boundary conditions are controlled by the number flux of molecules crossing the boundary, their assigned velocities, and their internal energies. In order to evaluate these quantities it is necessary to have the stream velocity, the temperature, the pressure, and species concentrations (in case of multicomponent flows) at the boundary. These values are obtained based on the type of the flow boundary condition and are explained in the following Chapters when needed.

Using specified temperature, stream velocity, and molar density of each species (which is directly related to pressure via the ideal gas law), the number flux of different species can be obtained using (this relation is used for each species [1]):

$$\dot{N} = \frac{n}{2\beta\sqrt{\pi}} \left[\exp\left(-s^2 \cdot \cos^2\theta\right) + \sqrt{\pi} s \cdot \cos\theta \left(1 + erf\left(s \cdot \cos\theta\right)\right) \right] \tag{2.61}$$

in which, θ is the angle between the stream velocity and the inlet plane and $s = v_0\beta$. These molecules are randomly located at the boundary and their thermal velocities are assigned

using the following distribution [1, 31]:

$$f_{\beta v'_n} \propto \beta \left(v'_n + v_{n0}\right) \exp\left(-\beta^2 v'^2\right) \tag{2.62}$$

Accordingly, the probability ratio is:

$$\frac{P}{P_{max}} = \frac{2\beta(v'_n + v_{n0})}{\beta v_{n0} + \sqrt{\beta^2 v^2_{n0} + 2}} \exp\left(\frac{1}{2} + \frac{\beta v'_n}{2}\left(\beta v'_n - \sqrt{\beta^2 v^2_{n0} + 2} - \beta^2 v'^2_n\right)\right) \tag{2.63}$$

In the above relations, v_{n0} is the normal component of the stream velocity and v'_n is the normal component of the thermal velocity. For implementing the acceptance–rejection method to sample v'_n from the last equation, a random number is generated in the range $[v_{n0}, 3/\beta]$ at the specified temperature for the inlet cell. Other thermal velocity components are obtained from Equations B.11 and B.14 of Appendix B. If there should be any tangential velocity at the inlet, their values are to be added to the sampled thermal values. The molecules which leave the outlet boundary are removed from the domain.

Chapter 3

Non-reacting flows

It was mentioned in Section 1.3 that few studies are available on multi–component (multi–species) gas flows inside micro/nano–channels using DSMC. Understanding the behaviour of DSMC in modelling these flows is the prerequisite for studying reacting flows. In addition, multi–component flows are important and common in applications; therefore, a DSMC code for modelling such flows is developed. Different flow and surface boundary conditions are investigated and the results are validated against other DSMC results and also the Navier–Stokes method in the slip regime. In order to obtain accurate results with low statistical scatter and within a reasonable computation time, many parameters should be set correctly for DSMC. The number of simulating particles is one of these parameters. Too many particles can extend the computation time to an infeasible point while too few particles can increase the order of magnitude of the statistical scatter to the order of results. Thus, in this chapter, effects of number of simulating particles on the results is first investigated. Another important parameter in DSMC is the collision model which simulates macroscopic properties of the flowing gas like viscosity and molecular diffusion. In order to verify the DSMC code and also to find out which molecular collision model is suitable, results of the code for single and multiple component slip flows are verified with corresponding data obtained from the Navier–Stokes method. Appropriate implementation of inlet/outlet flow boundary conditions in DSMC is another key factor. A constant pressure boundary condition using the Maxwell velocity distribution was used in obtaining

the results which were compared with Navier-Stokes data. Effects of using a higher order velocity distribution (Chapman–Enskog) for predicting stream and molecular quantities at flow boundaries are studied and the results are presented in the last section of this chapter.

3.1 Number of simulating particles

In the DSMC method, two parameters affect the results numerically: sizes of the sampling cells and the number of simulating particles. As it was discussed in Section 2.2.1, the maximum value of Δx is restricted by a suggested value of $\lambda/3$. Also, Δx can not be very small in order to have a meaningful average with an acceptable standard deviation inside the cell. In fact, the cell dimensions must be much larger than mean molecular spacing δ. In addition, calculating Δt depends on the vale of Δx and choosing very small Δx will dramatically increase the computational time. Therefore, based on the flow properties $\Delta x = \lambda/3$ is an optimum value. However, the number of simulating particles can vary considerably and it is reported in the literature that the optimum number is between 20-30 particles per cell, depending on the nature of the problem. In Figure 3.1, the effect this value ranging from 4 to 64 particles per cell on two sectional profiles of the stream velocity located at 50% and 75% of the channel length is shown for Case 4 of Table 4.2.

As seen, using 4 or 16 particles per cell causes statistical scatter and hence the results fluctuate especially close to the channel mid–plain. On the other hand, the profiles obtained from using 32 and 64 particles per cell have smoother profiles coinciding with each other. Therefore, for the results shown in the rest of the thesis, at least 30 particles per each cell is initially set.

3.2 Verification against Navier-Stokes

Data achieved from experimental studies of gas flows in micro/nano–channels are very limited due to manufacturing difficulties and current restrictions in sensor technology. Published studies include just pressure measurements at some spots along a micro–channel [2]

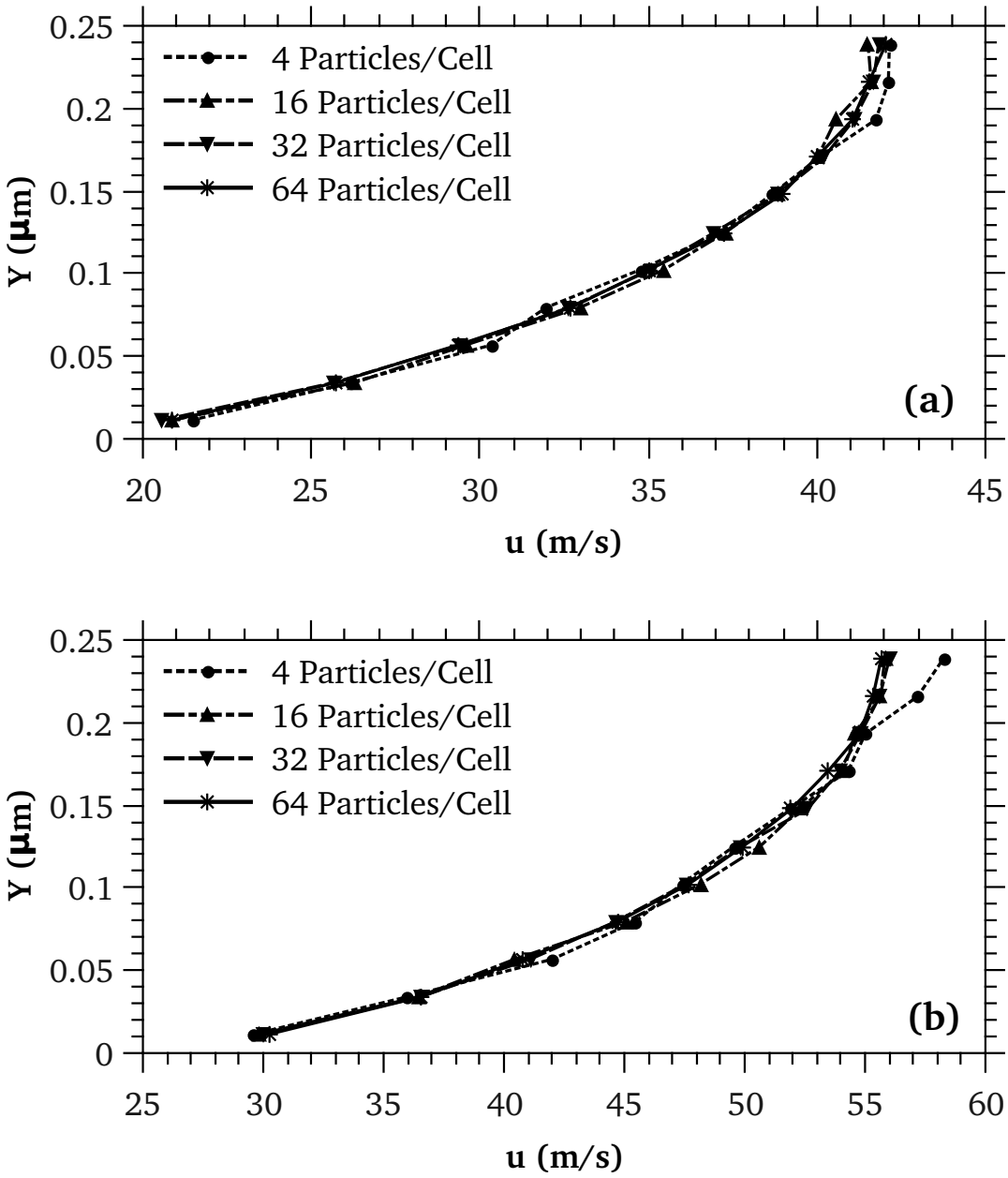

Figure 3.1: Demonstration of solution independence to number of simulating particles for sectional distribution of stream velocity at 50% (a) and 75% (b) of the channel length. The results are shown for the lower half of the channel.

and capturing variable profiles requires further technological developments. This makes it difficult to verify numerical simulations especially for the transition regime. DSMC is generally accepted as the reference method for these cases; however, an efficient implementation of DSMC requires setting up its different parameters (flow boundary conditions, molecular collision model, and number of simulating particles) correctly. This is particularly important for gas mixture simulations in which collisions of the molecules with different masses are involved. Very few studies have been conducted on modeling gas mixture flows using DSMC and nearly non of them have been verified. Considering the fact that conventional collision models (HS, VHS, etc.) should be modified for molecular collision with large mass discrepancy [39], a through verification seems essential for this case. In order to reach the optimum parameters, the results of the DSMC code prepared for this study are compared to the data obtained from a Navier–Stokes code with slip/jump conditions on walls [21]. The Navier–Stokes code has been intensively verified against existing experimental data [40, 41, 42] and therefore, validating DSMC results against its solutions is in fact comparing DSMC results to experimental data indirectly. This comparison is made for a Kn in the slip regime which is the overlap of the lowest Kn range applicable for DSMC and the highest Kn range applicable for Navier–Stokes.

3.2.1 Problem definition

A gas mixture flow of H_2/N_2 and $H_2/N_2/CO_2$ in a parallel channel is considered. A constant atmospheric pressure is applied at the outlet and the wall temperature is kept constant. In this section, the solution domain is split into two parts for proper handling of the outlet boundary condition. As shown in Figure 3.2, the gas molecules are diffusely reflected back into the domain at the wall temperature in the micro–channel section, while specular reflection is applied to the pseudo–reservoir section walls without reaching the equilibrium state.

A constant and uniform mass flux $\dot{m}''$ is imposed at the inlet such that $\rho_i u_i$ is kept constant for each species denoted by "i". This is done by calculating ρ_i from $Y_i \dot{m}''/u_0$ where Y_i is the species mass fraction obtained from a specified equivalence ratio ϕ and u_0 is the mean stream velocity sampled at the cell adjacent to the boundary. Using ρ_i and

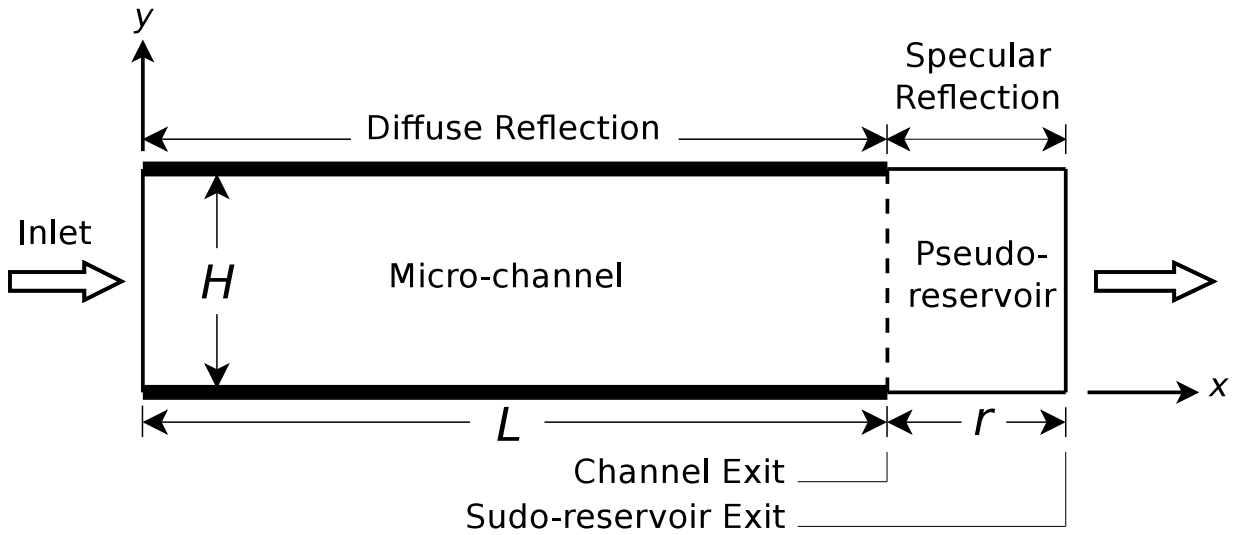

Figure 3.2: The DSMC solution domain which is divided into the microchannel and the pseudo–reservoir sections of a length r.

u_0, the number flux of molecules entering at boundary can be evaluated using the method explained in Section 2.3.3. This procedure is performed at each time step so that the mean value of $\dot{m}''$ remains constant over time. It should be noted that for moderate to high Péclet number flows where advection transport is dominant, species velocities u_i are close to u_0 and therefore, Y_i can be calculated based on u_i instead of u_0. In Section 4.2 an improved method for highly diffusive flows is introduced and verified.

The method used to control the outlet pressure is similar to the one introduced by He et al. [43] but modified for multi–component gases. In this method, the streamwise velocity of each species u_i is calculated from:

$$n_i u_i = \dot{N}_i^+ - \dot{N}_i^- \tag{3.1}$$

where $\dot{N}_i^+$ is the number flux of species "i" in the positive x direction and is sampled directly by counting the number of molecules leaving the boundary. And, $\dot{N}_i^-$ is calculated using Equation (2.61) by substituting $v_0 = -u_0$ where the magnitude of u_0 is adopted from the previous time step. Furthermore, the species number density n_i is determined from nX_i where n (the total number density) is obtained using the ideal gas law ($n = p_o/kT$),

and X_i (the species molar fraction) and T are both taken from the adjacent boundary cell. p_o is the specified pressure imposed at the outlet. Using the above quantities, the new u_0 for the current time step is calculated from:

$$\bar{u}_0 = \frac{\sum_{i=1}^{N_g} m_i \left(\dot{N}_i^+ - \dot{N}_i^- \right)}{\sum_{i=1}^{N_g} m_i n_i} \tag{3.2}$$

where N_g is the number of species in the gas and m_i is the molecular mass of species "i".

The detail analyses of data obtained for species fractions show that there are some inaccuracies associated with the mass fraction data. This is caused by the defects in the calculation of $\dot{N}_i^-$ and the Maxwellian velocity distribution employed in Equation (2.61) is the main reason. The Maxwellian distribution assumes equilibrium conditions at the outlet; however, existing velocity, temperature and concentration gradients violate this assumption. This leads to some deviations from the actual value of the number flux required for $\dot{N}_i^-$. This effect is especially magnified in multi–component flows in which molecules have considerable mass discrepancies. That is why in this section a pseudo–reservoir is added to the channel exit with specular reflection at the wall. This moves inaccuracies further downstream and therefore prevents them from affecting the velocity distribution at the channel outlet boundary. A practical interpretation of such an arrangement can be thought of as a number of parallel micro–channels discharging into a constant pressure reservoir. The specular reflection on pseudo–reservoir walls acts as a symmetry boundary and the numerical results show that the pressure remains essentially constant and equal to P_o throughout this section.

3.2.2 Numerical implementation

The Navier–Stokes equations, slip/jump boundary conditions, and a brief description of the numerical implementation are presented in Appendix C. It is worth noting that the fluid properties required in the Navier–Stokes calculations are adopted from experimental references [40, 41]. There is also a discussion about the effects of the accommodation coefficient on the results in comparison with existing experimental data in [44]. Therefore, input parameters of the Navier–Stokes calculations are independent from the current

Table 3.1: Properties of single molecules and binary pairs for different species [28].

	N_2	H_2	CO_2	N_2/H_2	N_2/CO_2	H_2/CO_2
Molecular diameter $\times 10^{10}$	4.11	2.88	5.54	3	3.75	3.29
Molecular mass $\times 10^{26}$ (kg)	4.65	0.33	7.31	–	–	–
VSS scattering parameter	1.36	1.35	1.61	1.41	1.87	1.69
Viscosity index ω	0.74	0.67	0.93	0.78	0.75	0.84
Degree of freedom	5	5	6.7	–	–	–

DSMC method and hence, there is no recursive verification in between. The pseudo–reservoir length is set equal to 15% of the channel length. It was found that the Variable Soft Sphere (VSS) model should be employed for the collision processes and VHS can not simulate variations near the wall correctly. The total number of simulating particles considered here is 619,000. It was found that the results are independent of the number of simulating particles when more than 30 simulating particles per cell are used. In addition, cell sizes of $\Delta x = 0.45\lambda$ and $\Delta y = 0.33\lambda$ yield grid independent results, where λ is considered here as the smallest molecular mean free path of the mixture components. This ensures that a molecule with the maximum molecular speed (three times the largest most probable speed) cannot traverse a cell face during an iteration. Thus, for the current problem, the solution domain is divided into 350×100 cells in the x and y directions, respectively. The final results are sampled after 2×10^4 time steps with $\Delta t = 7.8 \times 10^{-12}$ increments. The calculations were carried out using the gas properties listed in Table 3.1.

In order to ensure the accuracy of the prepared DSMC code, its results are validated by comparing the velocity slip and wall heat flux results with previous DSMC studies. Figure 3.3[1] (a) shows the velocity slip along a 2.0μm channel with N_2 as the working fluid compared with the Liou et al. [13] data. The channel height is 4.0μm, pressure ratio is 2.5 and inlet and wall temperatures are 300K and 323K, respectively. Figure 3.3 (b) shows the wall heat flux predictions of the current DSMC method together with the numerical

[1]The properties of the gas binaries shown in Figure 3.3 can be found in [13] and [15], and are repeated in Table 3.1

simulations of Wang et al. [15] for two binary gas mixtures. In these simulations, the channel length and height are 4.0μm and 1.0μm, respectively, with a pressure ratio of 3.0. The inlet gas temperature is 300K while the walls are kept at 350K. Very good agreement is observed in both comparisons.

3.2.3 Results and discussion

Table 3.2 shows all cases studied for comparison purposes. As seen, results of DSMC and Navier–Stokes methods are considered under various geometries and flow variables. Effects of the channel height is investigated by studying H =1.5μm and H =4μm. The aspect ratio is constant for all cases and is equal to L/H =4.0. A constant inlet temperature of 300K is specified but different wall temperatures T_w of 300K (isothermal), 350K, and 400K are applied. The outlet pressure is kept at atmospheric value for all cases. Two different mass fluxes of $\dot{m}''_{in}$ =50kg/m^{2}s and $\dot{m}''_{in}$ =100kg/m^{2}s are also considered which are applied uniformly along the inlet boundary. The chosen species are H_2 and N_2 since they are common gases and can be found in many applications. In addition, they have considerable mass difference and simulating this mixture by DSMC collision models can ensure its ability for modelling other mixtures as well. For the multi–component mixture of Case 6, CO_2 is considered since its a multi–atomic species which includes more internal degrees of freedom. This challenges the DSMC algorithm and can reveal its ability in simulating various gas species. Mass fractions considered at the inlet are chosen such that number of molecules for different species are equal. This ensures minimum error caused by non–uniform intermolecular collisions.

Mass and momentum transfer

Figure 3.4 shows the comparison of of slip velocity distribution along the channel. The data for DSMC is interpolated at the edge of the Knudsen layer which limits the Navier–Stokes solution domain. Generally, good agreement is observed and the maximum deviation is about 11% at the inlet where non–equilibrium conditions are extreme which causes maximum slip. It decreases right after the inlet as gradients reduce and then increases as

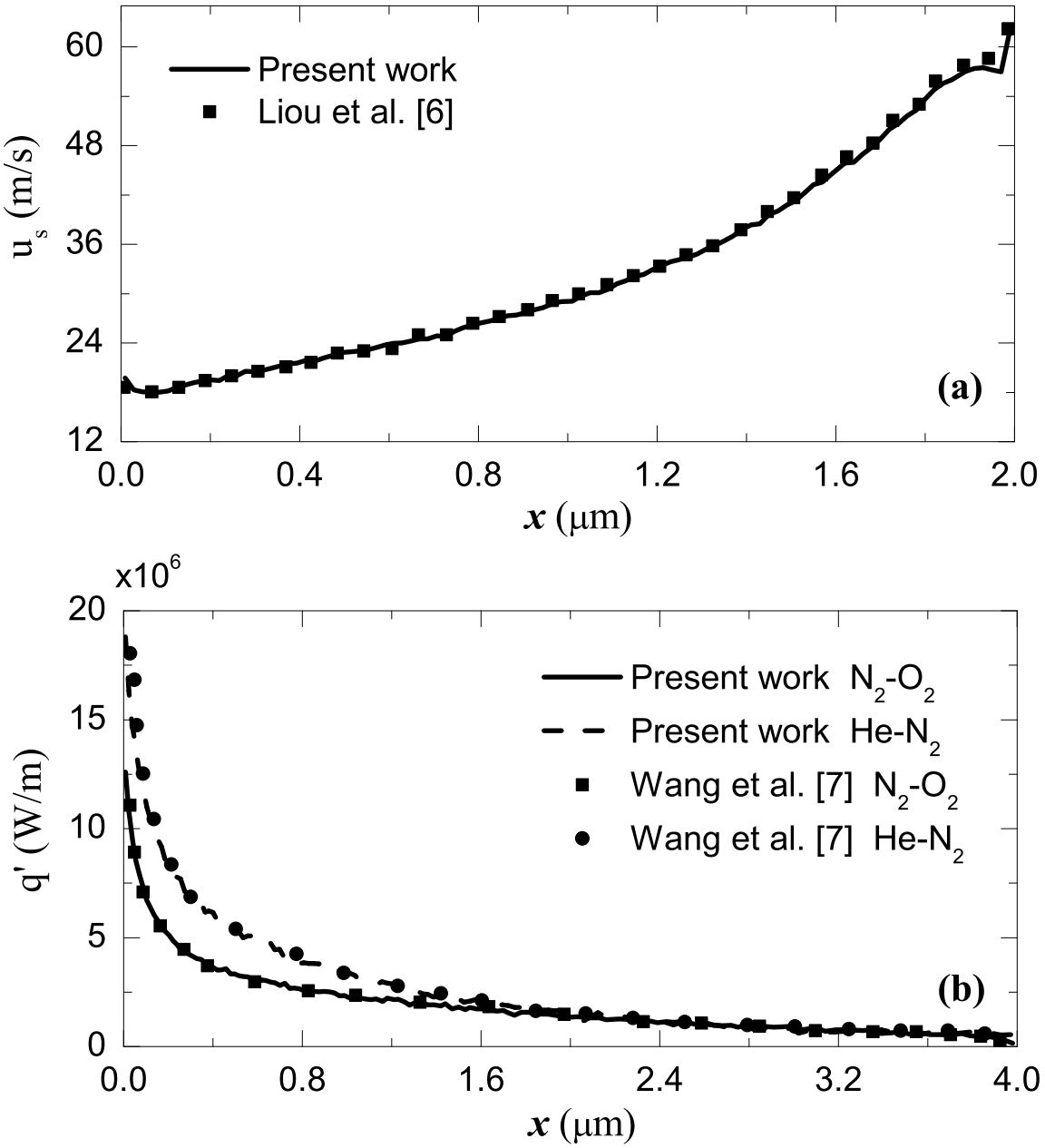

Figure 3.3: Velocity slip (a) and wall heat flux (b) compared to the DSMC results of Liou et al. [13] and Wang et al. [15].

Table 3.2: Geometrical and operational specifications of different cases.

	Mixture	H (μm)	L (μm)	$\dot{m}''_{in}$ (kg/m^2s)	T_w (K)	Mass % fraction		
						H_2	N_2	CO_2
Case 1	H_2/N_2	1.5	6.0	50.0	350	10.0	90.0	–
Case 2	H_2/N_2	1.5	6.0	50.0	300	10.0	90.0	–
Case 3	H_2/N_2	1.5	6.0	100.0	350	10.0	90.0	–
Case 4	H_2/N_2	1.5	6.0	50.0	400	10.0	90.0	–
Case 5	H_2/N_2	4.0	16.0	50.0	350	10.0	90.0	–
Case 6	$H_2/N_2/CO_2$	1.5	6.0	50.0	350	2.7	37.8	59.5

rarefaction continuously goes up. The predictions of the two methods are very closer to each other where non–equilibrium effects are less intense.

Figure 3.5 shows slip velocity data for Cases 1–4. Effect of the wall temperature T_w is presented by Cases 1,2, and 4. As seen, slip velocity predicted by DSMC for isothermal flow (Case 2) is a little higher. The reason can be the temperature gradient caused by viscous dissipation which is naturally captured in DSMC and therefore, increases the slip velocity. A good agreement is observed for Cases 1 and 4 in which the temperature gradient produced by higher T_w increases the slip velocity. Cases 1 and 3 demonstrate the effect of higher inlet mass flux $\dot{m}''_{in}$. By elevating $\dot{m}''_{in}$, velocity gradients and therefore, non–equilibrium effects increase along the channel causing higher slip velocity. This rise in the slip velocity is more pronounced at the outlet compared to the inlet since the outlet pressure is kept constant and thus, the stream velocity and velocity gradients have much larger values. As observed, DSMC and Navier-Stokes show some deviations for Case 3 due to the intense non–equilibrium effect resulting from these gradients.

Distributions of axial (x–component) and normal (y–component) velocities across the channel is shown in Figure 3.6 at three locations along the channel for Case 1. A very good agreement is generally observed which implies that the viscosity of the gas mixture is effectively simulated by DSMC. The largest different between the two methods happens

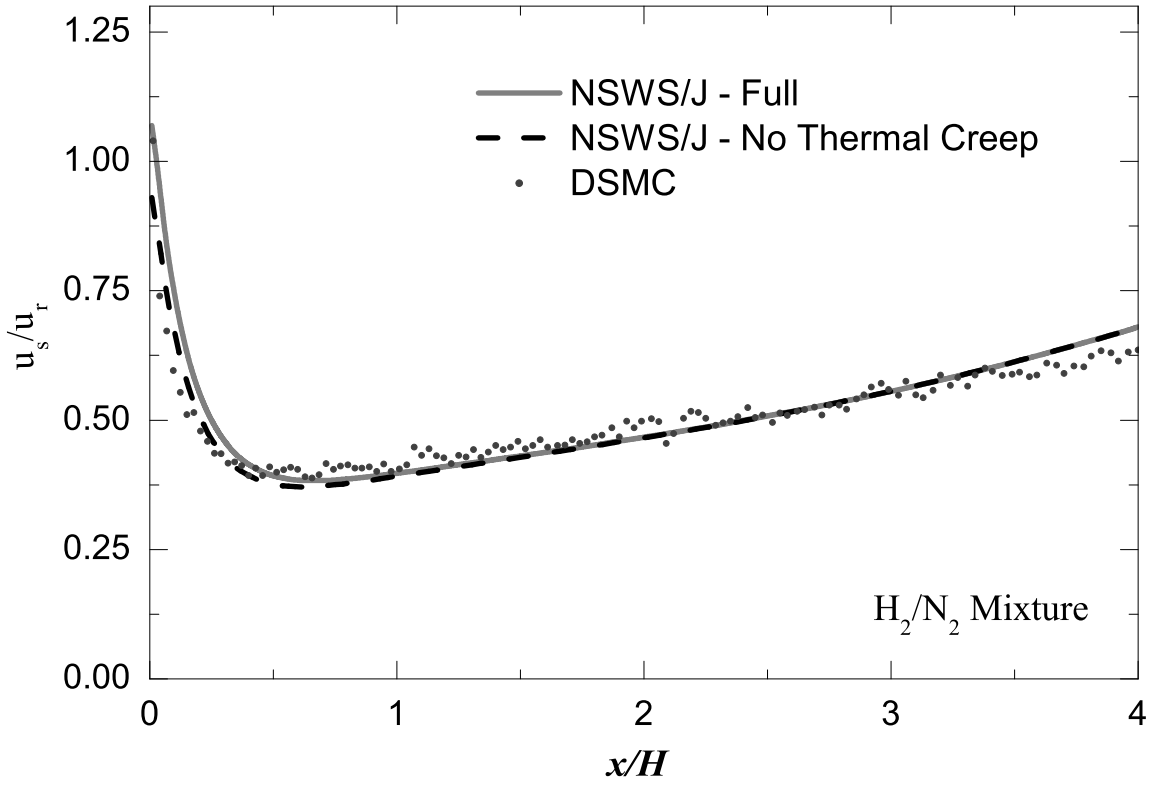

Figure 3.4: Slip velocity distribution along the channel obtained from Navier–Stokes and DSMC methods. u_r is the reference velocity ($u_r = 50m/s$).

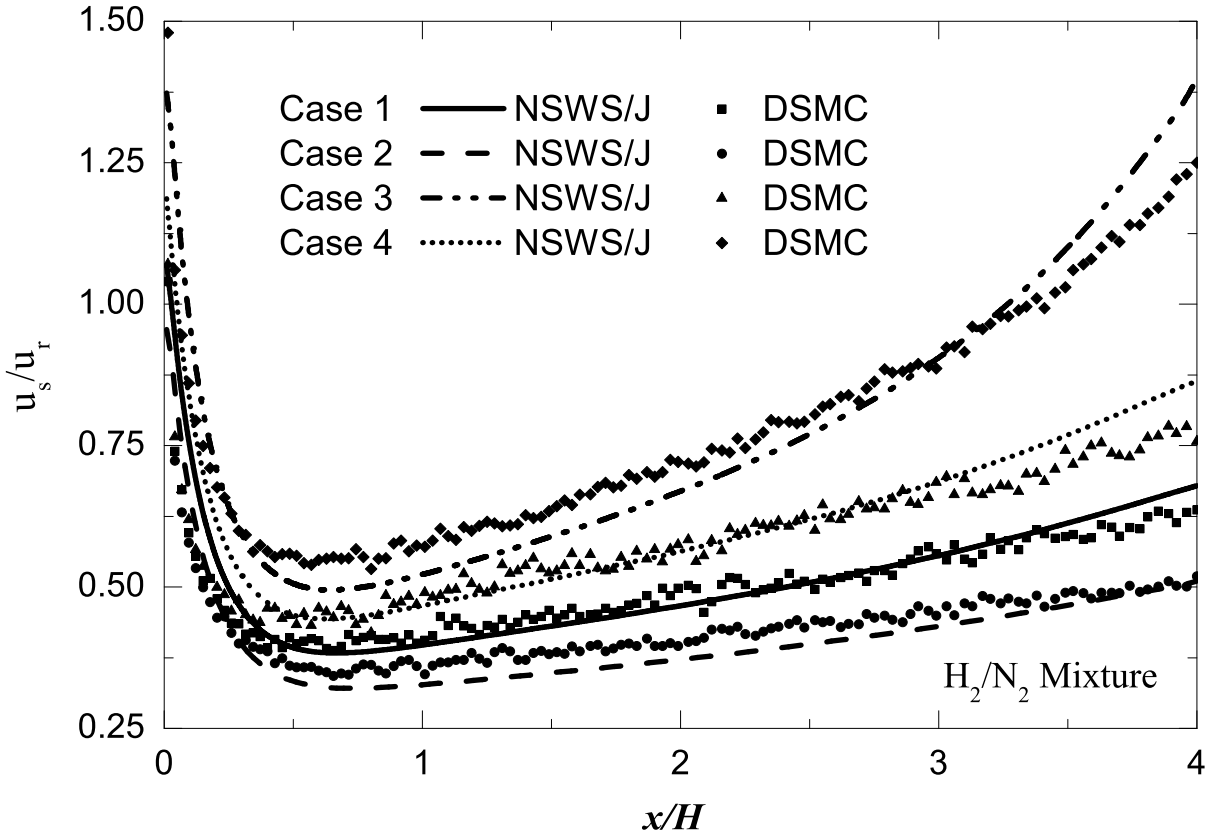

Figure 3.5: Normalized slip velocity under different operating conditions specified in Table 4.2. The reference velocity is $u_r = 50$ m/s.

at the mid–plane and closer to the outlet. It seems that higher rarefaction effects at the outlet (due to larger mean free path and Kn) penetrate upstream into the bulk motion causing Navier-Stokes slip model to digress more from DSMC.

Effects of the channel height on slip velocity data of Cases 1 and 5 are demonstrated in Figure 3.7. As seen, by rising the channel height and decreasing Kn, the slip velocity decreases as expected. The two methods agree well for both cases; however, for the smaller channel (and hence, higher non–equilibrium conditions) there is a little deviation at the inlet. Variations of Kn[2] is also shown for both Cases and demonstrates that the rarefaction is more magnified at the outlet by decreasing the height. This occurs due to rapid pressure drop close to the outlet causing steep Kn elevation which also causes a discrepancy between the results.

Profiles of mass fraction Y_i of H_2 and N_2 across the channel are shown in Figure 3.8 for Case 1 at x/H=0.259. As mentioned before, H_2 and N_2 have large mass discrepancy and this causes considerable difference in their diffusion. H_2 is the lightest available molecules and therefore its most probable thermal speed V_{mp} is very high according to the relation: $V_{mp} = \sqrt{2kT/m}$. This increases the diffusion of H_2 upstream especially at the vicinity of the wall where the gas temperature is higher. As seen in the magnified view of Figure 3.8, this causes non–uniform variations for N_2 mass fraction close to the wall. Moreover, Y_{N_2} decreases near the wall which proves higher upstream diffusion of H_2 in this location. There is almost a constant difference between predictions of the two methods with an amount of less than 8% and 1% for H_2 and N_2, respectively. It should be noted that this deviation is partly due to the difference in the method of enforcing constant mass flux at the entrance for DSMC and Navier-Stokes. For DSMC the iterative nature of imposing constant $\dot{m}''_{in}$ makes the obtained results to be between the specified values and the results of the previous step. In addition, values of the stream velocity and the number density are adopted from the boundary cell since these are not accessible at the boundary. Therefore, $\dot{m}''_{in}$ has small differences (slightly lower) which is carried into the channel with the flow and is one of the causes of the deviation seen in Figure 3.8. Furthermore, the upstream diffusion of lighter species affects $\dot{m}''_{in}$ applied by the Navier-Stokes method, especially in the region

[2]Wall Knudsen number is calculated from the conventional definition of Knudsen number λ/H with the mean free path λ obtained at the vicinity of the wall.

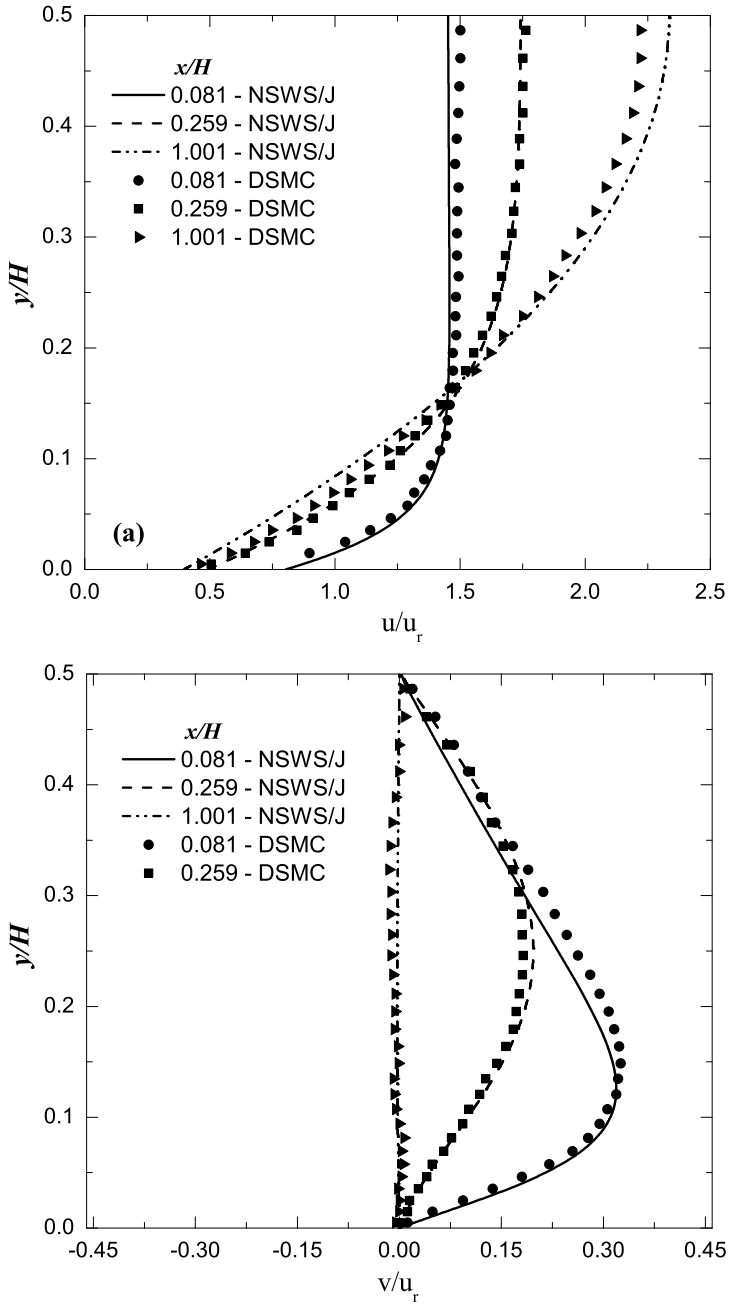

Figure 3.6: Distributions of x–component (a) and y–component (b) of the stream velocity across the channel at three locations along the channel for case 1.

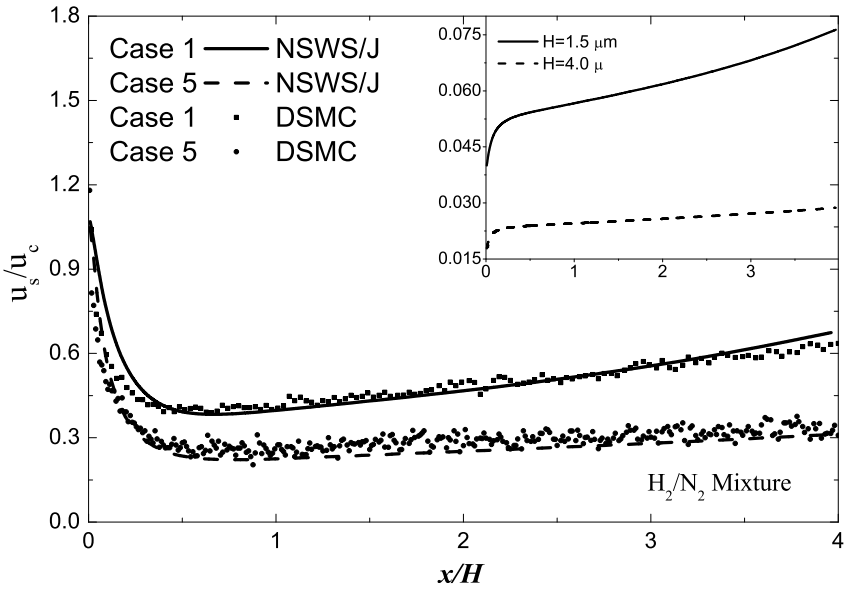

Figure 3.7: Normalized slip velocity and the wall Knudsen number in a $H = 4\mu m$ channel.

close to the walls. This also can be considered as one of the reason for the above mentioned deviation.

As stated before, a pseudo–reservoir is added at the outlet in order to keep the channel domain unaffected of the inaccuracies caused by the outlet pressure boundary condition. Figure 3.9 (a) shows the effect of the pseudo–reservoir length on the behaviour of the slip velocity for Case 1. It is observed that r=0.15L results in less fluctuations and also improves the proximity of the predictions. However, extending the pseudo–reservoir length to r=0.3L does not change the results considerably. This shows that the r=0.15L sufficiently reduces the effects of the outlet boundary condition inaccuracies and the differences of the results come from their intrinsic specifications. Figure 3.9 (b) demonstrates the behaviour of temperature jump variations (T_s is the gas temperature next to the wall surface) under different pseudo–reservoir lengths. As shown, T_s is not affected by changing pseudo–reservoir lengths. This is due to the fact that T_s approaches T_w quickly within the fist half of the channel and hence, incoming molecules at the outlet boundary have already temperature equal to T_w. Overall r=0.15L is chosen based on the information obtained from Figure 3.9.

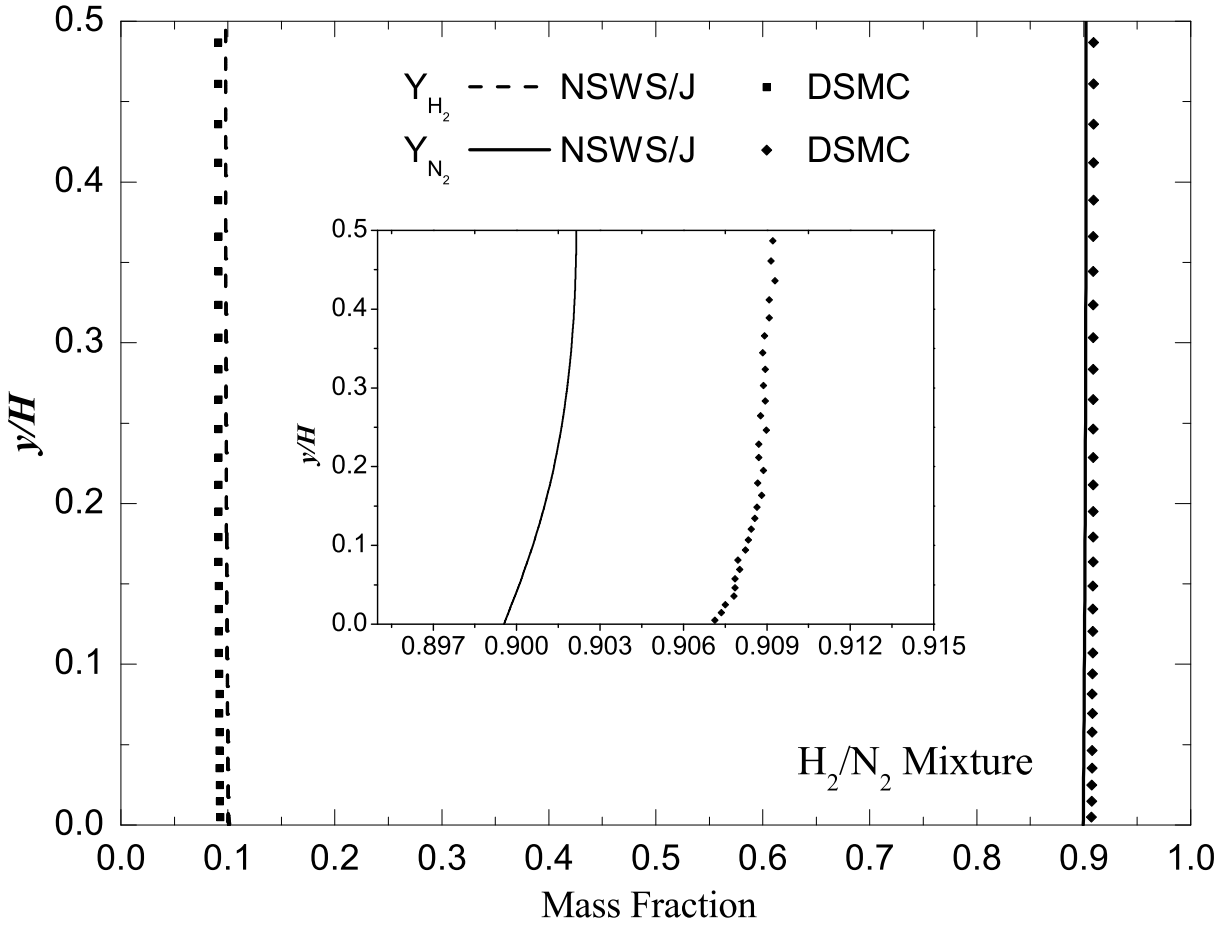

Figure 3.8: Hydrogen and nitrogen mass fractions across the channel at $x/H = 0.259$ for case 1.

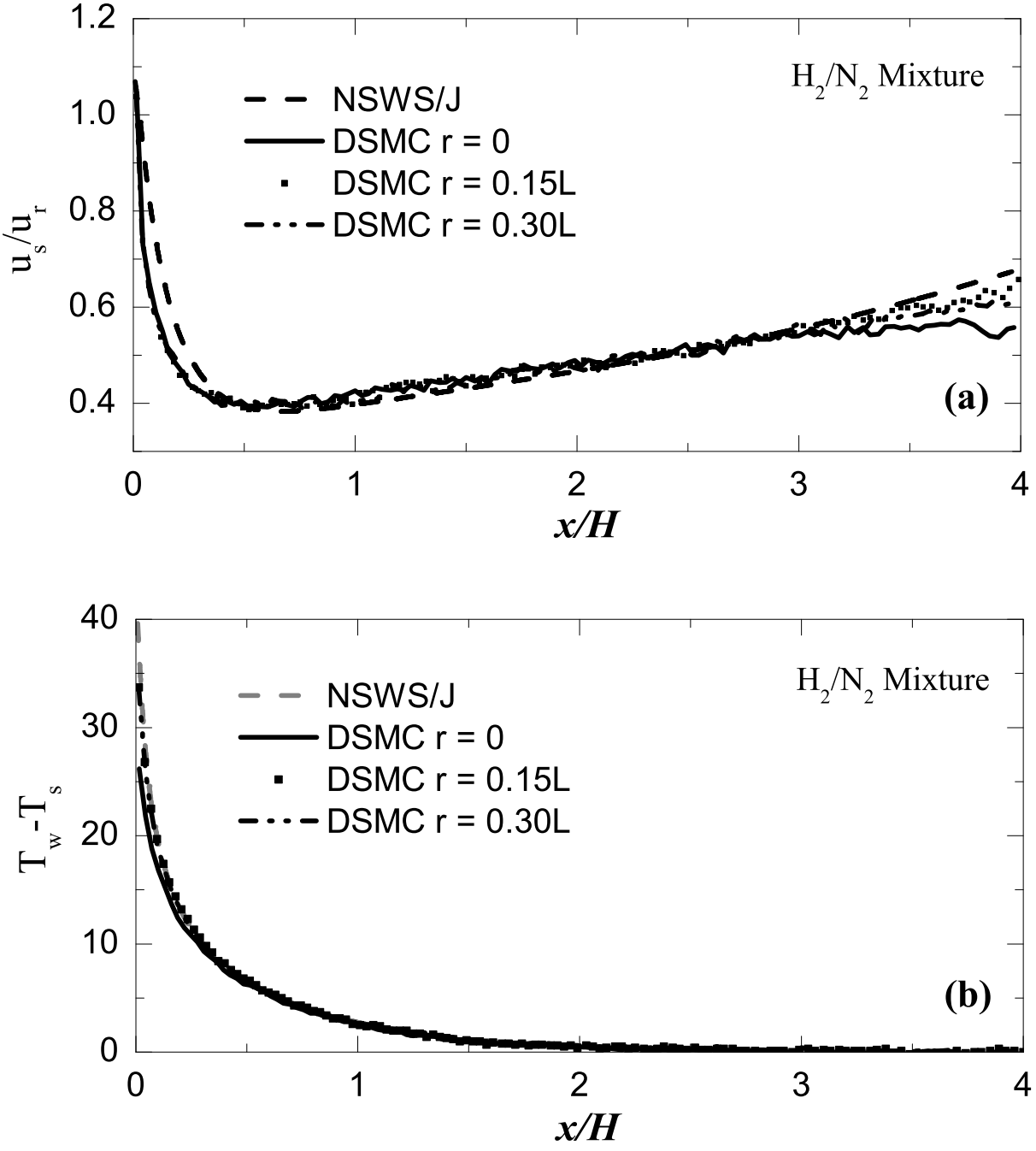

Figure 3.9: Velocity slip (a) and temperature jump (b) predictions for case 1 with different pseudo–reservoir lengths. u_r=50m/s

The results of the slip velocity for a multi–component gas flow of $H_2/N_2/CO_2$ are shown in Figure 3.10 (a). A behaviour similar to Figure 3.4 is seen and therefore, adding another component to the flowing gas did not change the agreement of the two methods. The discrepancies observed close to the inlet and outlet boundaries are analogous to Figure 3.4 and are caused by non–equilibrium effects. Figure 3.10 (b) shows mass fractions of the three species. A good conformity between DSMC and Navier-Stokes methods is generally observed. As shown in the magnified view, the mass fraction of H_2 is higher close to the wall. It was stated previously that this occurs due to higher upstream diffusion rate of H_2 near the wall.

Heat transfer

Apart from the statistical scatter introduced naturally by the DSMC algorithm, the temperature jump data for Cases 1,3, and 4 for both methods are in very good compliance as shown in Figure 3.11. The temperature jump generally has its highest value at the inlet due to larger velocity and temperature gradients and gradually fades out along the channel. It is observed that the presence of a temperature gradient is essential for having temperature jump at the wall since, there is no temperature jump close to the outlet, despite the equilibrium effects present there. That is also why the temperature jump distribution is not affected by the outlet conditions (e.g. the length of the pseudo–reservoir).

The simulation results of the wall heat flux for Cases 1,3, and 4 are shown in Figure 3.12. This quantity in the DSMC method is obtained from:

$$q'' = \frac{\sum_{i=1}^{N_g} e_i^* - \sum_{i=1}^{N_g} e_i}{A \cdot \Delta t} \tag{3.3}$$

where e_i^* is the summation of translational and internal energies (total energy) of a single simulating particle reflected back from the wall surface having the wall temperature (thermally diffuse), e_i is the total energy of the same simulating particle right before hitting the surface, Δt is the DSMC sampling time step and A is the surface area of the incident cell and is equal to Δx. As seen, predictions of the methods are in very good agreement. The maximum deviation of 10% is observed for Case 4 at the inlet. The reason is mainly due to intense non–equilibrium conditions close the the inlet which lead to a difference between

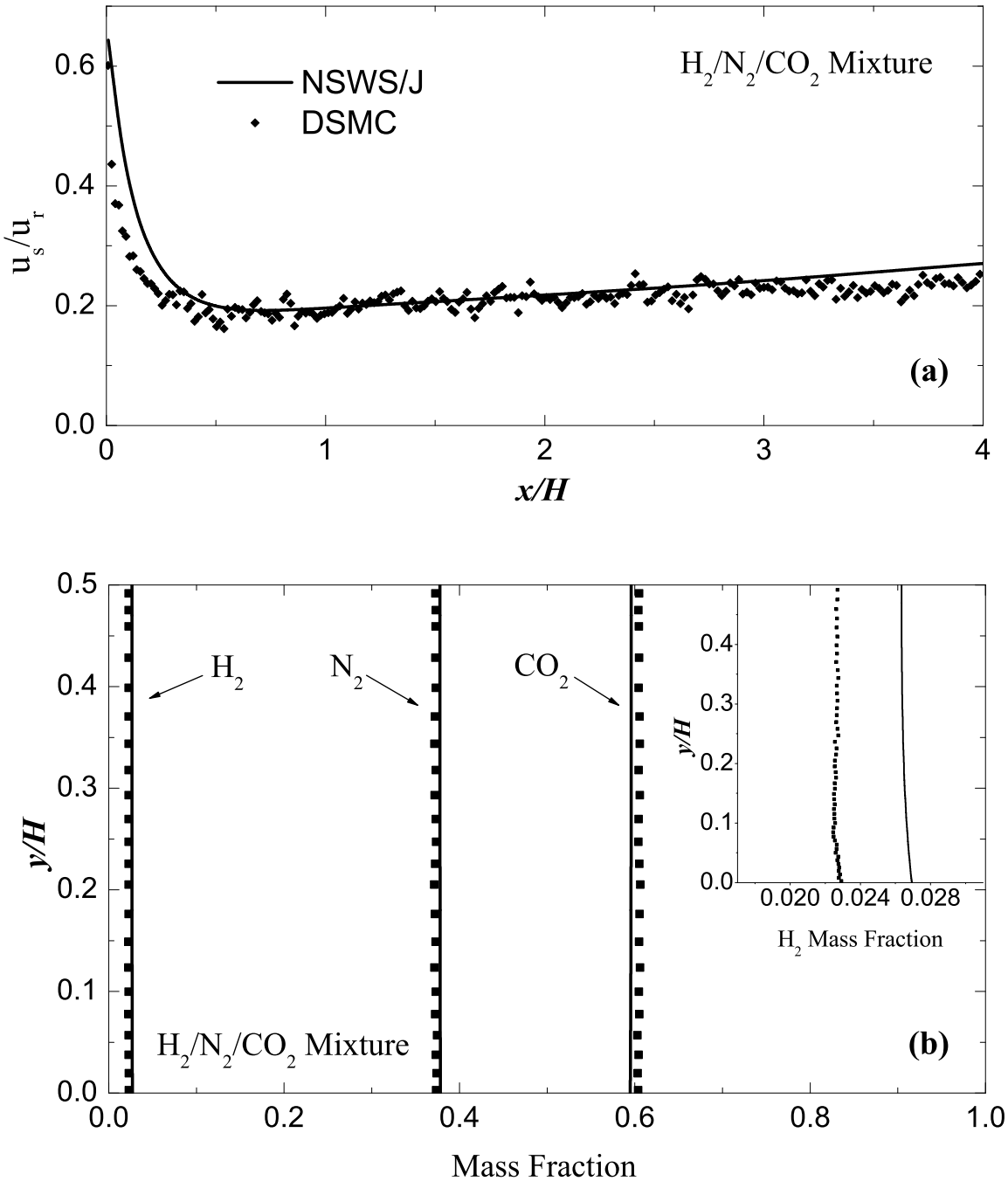

Figure 3.10: Velocity slip (a) and mass fractions of $H_2/N_2/CO_2$ at $x/H = 0.157$ (b) for the gas mixture of Case 6

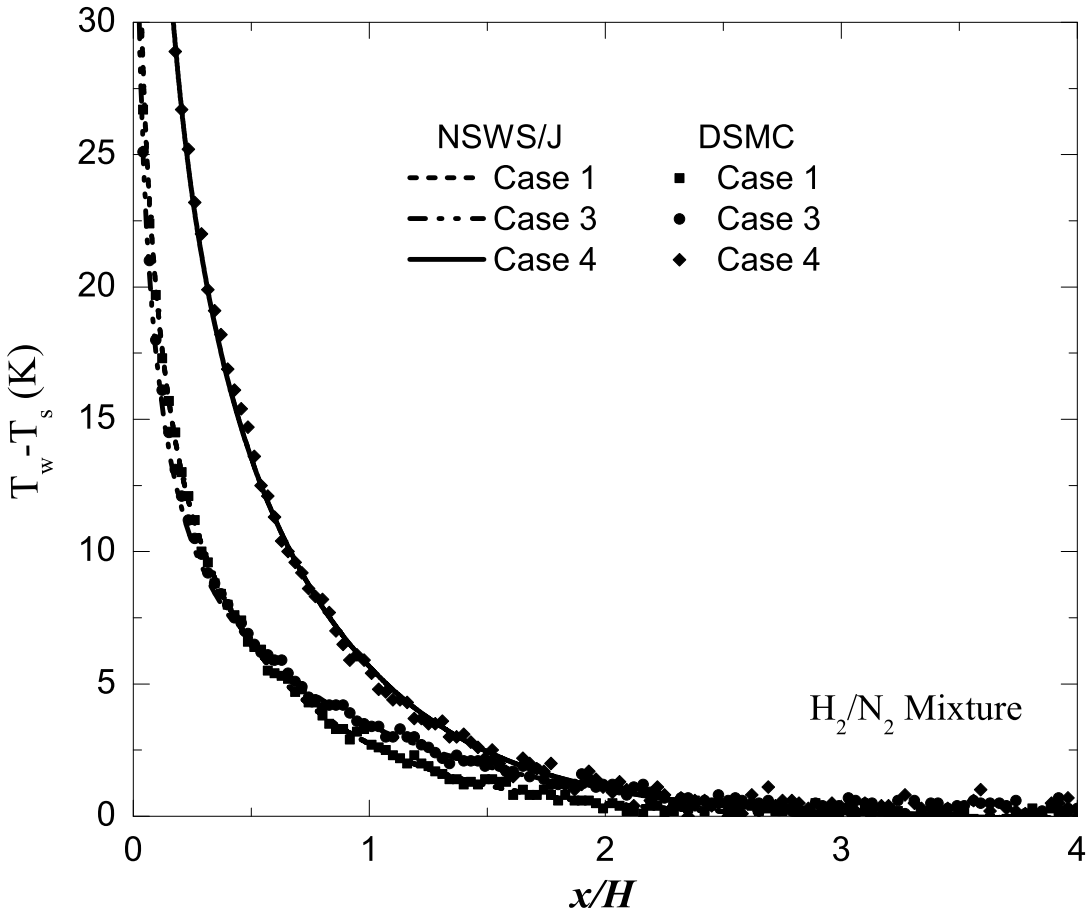

Figure 3.11: Temperature discontinuity at the edge of the Knudsen layer under different operating conditions.

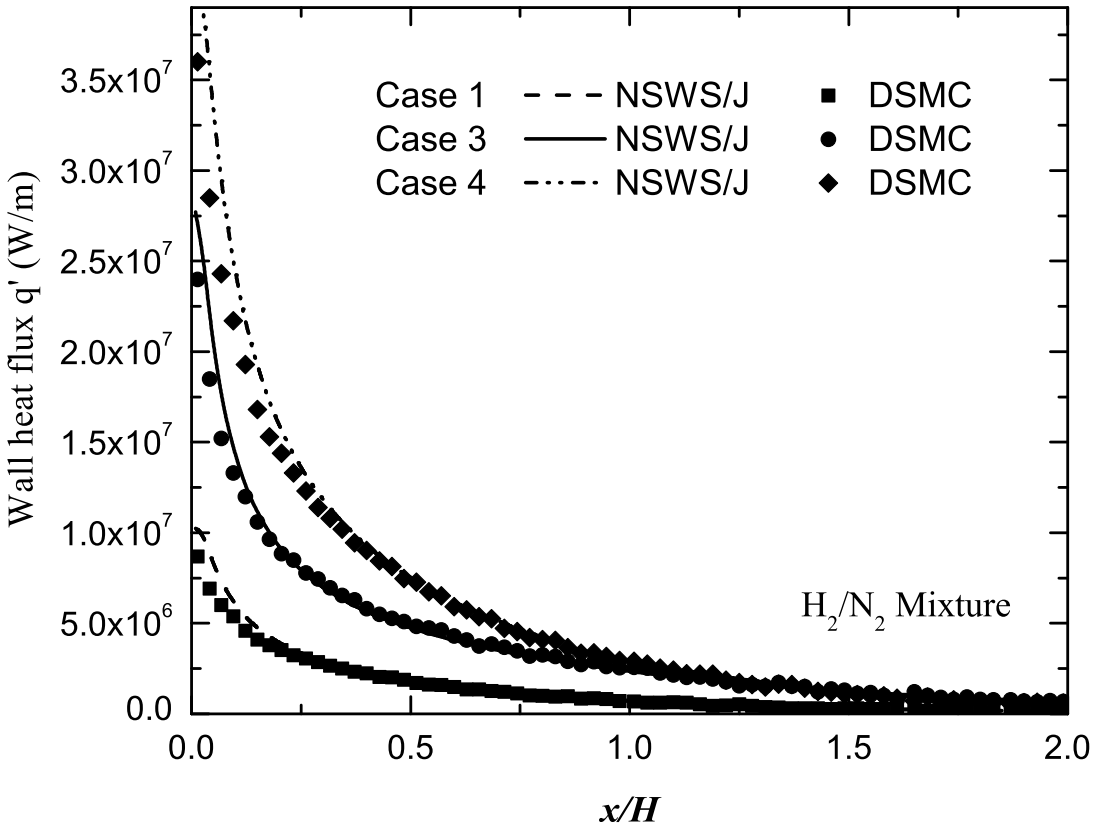

Figure 3.12: Wall heat flux along the channel under different operating conditions; The results of Case 1 are multiplied by 0.5 to avoid cluttering.

the mean collision rate of molecules with the wall calculated by DSMC and Navier–Stokes methods. In Navier-Stokes this quantity is calculated by the Maxwell distribution in the form of continuum relations which is necessarily applicable just for the equilibrium state. Whereas, in DSMC the mean collision rate is sampled directly. Therefore, heat flux values obtained from the DSMC are slightly lower than Navier-Stokes since in rarefied conditions less molecules are expected to hit the wall surface. This results in less energy carries into the flow as shown in Figure 3.12.

3.2.4 Summary

The results of DSMC and Navier-Stokes methods are compared for binary and multi–component gas mixture micro–flow in the slip regime. The Navier-Stokes results are obtained from a verified code with slip/jump boundary treatment developed by Qazi Zade et. al. [45]. The gas mixtures used in this study were N_2/H_2 and $N_2/H_2/CO_2$. This combination ensures to challenge the ability of DSMC in reproducing flow properties such as viscosity and molecular diffusion for a mixture with large mass discrepancies and multi–atomic molecules. A constant mass flux is imposed at the inlet and an atmospheric pressure is applied at the outlet. In order to prevent the channel domain from being affected by the inaccuracies resulting from the Maxwell distribution used in the outlet pressure boundary condition, a pseudo–reservoir with specular reflection on its walls is added at the channel exit. It is found that the pseudo–reservoir is enough to be 15% of the channel length. Based on the considered cases, effects of the channel height, the wall temperature and the inlet mass flux on the conformity of the methods on prediction of the slip velocity, the temperature jump, the wall heat flux, and velocity profiles are studied. It was found that the VSS collision method should be used for capturing near wall phenomena correctly.

3.3 Effect of higher order pressure boundary conditions

AS stated before, numerical simulation of multi-species gas flows through micro/nano-channels is the first step for modelling chemically reacting flows. One of the challenges on the way of modelling such flows using DSMC is the implementation of the flow boundary conditions. A prescribed pressure is the most commonly used inlet/outlet boundary condition. In order to control the pressure value at the boundary, local values of stream velocity components, density and temperature must be either known or calculated in each time step. The temperature and the number density are imposed directly at the inlet boundary as their values are known. For the outlet boundary, these quantities are taken from the sampled values of adjacent cells. Two different methods for evaluating velocity components

have been reported for the case of single-species gas flows. The first method, introduced by Nance et al. [46], uses the characteristic line equations of sound wave propagation for the outlet boundaries and Wang and Li [14] further developed it for inlet boundaries. One of the fundamental assumptions of the characteristic line method is that the flow is isentropic. Our previous simulations Qazi Zade et al. [45], in agreement with Fang et al. [13], show that this assumption causes non-physical behavior in non-adiabatic flows as expected. The second method of obtaining unknown flow variables at the boundary involves using the velocity field information from the previous iteration step and applying a mass balance scheme at the boundary. Ikegawa and Kobayashi [11] first introduced this method using the number of molecules crossing the boundary during the last time step. However, the values of the molecular flux calculated during one time step are so small that the pressure boundary condition becomes unstable. Wu and Tseng [47] solved this problem by employing ensemble average values of flow properties, taken over previous time steps, in evaluating the molecular flux. This method has no extra assumptions and is based on the conservation of mass. Using values of the density, the temperature and velocity components calculated from either of the above described methods, the molecular flux at the boundary is calculated via a relation derived from the Maxwell velocity distribution.

For multi-component flows, species concentrations should also be evaluated at the outlet boundary. As of yet, there is no specific methodology proposed in the literature, and available studies try to circumvent the need for calculating the species concentrations. Yan and Farouk [17] analyzed the mixing process of a binary gas flow and used the outlet boundary without any special treatment, i.e., those molecules leaving the domain were simply removed. Wang and Li [48] studied the mixing efficiency of N_2 and CO in a parallel micro-mixer, exerting a constant pressure both at the inlet and the outlet boundaries. However, the molecular specifications of both selected species were very similar, and therefore, the effect of mass diffusion was reasonably negligible and the utilization of the single-species boundary treatment was possible. Wang et al. [15] also simulated binary gas mixture micro-flows with different gas compositions between parallel plates in order to verify their new constant heat flux boundary condition. The details of the pressure boundary conditions they implemented were not described, but based on our simulations, the pressure ratio of 3.0 applied to a $1\mu m \times 4\mu m$ micro-channel results in a near sonic velocity at the

outlet. Under such a condition, the exit pressure cannot practically be controlled since the number of molecules entering the domain at the boundary is negligible. In the present work, a pressure boundary condition for a multi-species flow is introduced based on the Wu and Tseng [47] methodology. The number density for each species is sampled separately and species concentrations are calculated accordingly. The results for high speed flows are verified against Wang et al. [15] results. However, the accuracy of the method in predicting species concentrations decreases considerably as the flow speed is reduced. In an effort to overcome this problem, we noticed the effects of the rarefaction caused by the rapid pressure drop near the outlet flow boundary. This introduces non-equilibrium conditions and hence put the applicability of the commonly used Maxwell velocity distribution into question. The Maxwell distribution function is the first term of the general distribution function f written in a perturbation series as [1]:

$$f = f^0 + f^1 + f^2 + ... \tag{3.4}$$

where f^0 is the solution of the Boltzmann equation for a homogeneous simple gas in an equilibrium condition. By considering f^1 in the determination of f, deviations from equilibrium are taken into account up to first order. f^1 is obtained by the Chapman-Enskog solution of the Boltzmann equation. Here, the proposed pressure boundary condition for multi-species gas micro-flows is explained in detail and then modified by the Chapman-Enskog velocity distribution. The molecular flux expression is also modified accordingly and its general explicit form is presented. Then, the effect of the first order variations on controlling boundary pressure are demonstrated.

It should be noted that f^1 is derived by perturbing the distribution function f by a small amount from equilibrium conditions, and therefore, the accuracy of this method decreases as Kn increases. Nevertheless, the Chapman-Enskog distribution offers higher accuracy in comparison to the commonly used Maxwell distribution which neglects non-equilibrium effects.

3.3.1 Inlet and outlet boundary conditions

General description

As stated before, a specified constant pressure condition is commonly used at the inlet/outlet flow boundaries. In DSMC, the pressure is controlled by adjusting the velocity and the density of the gas which enters the domain at the boundary. The density of each species is calculated by the ideal gas law, $p_j = n_j kT$, where, p_j and n_j are the partial pressure and number density of the species j, respectively. In the boundary treatment proposed here, the temperature T is set equal to the corresponding value of the cell adjacent to the boundary, and the partial pressure of each species is calculated from $p_j = X_j p$ in which, $X_j = n_j/n_0$ is the mole fraction evaluated in the adjacent cell and p is the pressure to be imposed at the boundary. Having the value of n_j, the velocity component normal to the boundary for each species, u_j, is then calculated by a mass conservation scheme as follows:

$$n_j u_j = \dot{N}_j^+ - \dot{N}_j^- \tag{3.5}$$

where the values of $\dot{N}_j^+$ and $\dot{N}_j^-$ are the number fluxes of species j which cross the boundary in the positive and negative directions, respectively. At a boundary, either $\dot{N}_j^+$ or $\dot{N}_j^-$ which tends to leave the domain is known and can be evaluated by a sampling process, but the other one which is directed into the domain is not known and is obtained from:

$$\dot{N}_j^{+/-} = n_j \int_{-\infty}^{\infty} \int_{-\infty}^{\infty} \int_{0/-\infty}^{\infty/0} u_j f_j \, du_j dv_j dw_j \tag{3.6}$$

where, u, v and w are velocity components, each of which is composed of a mass averaged stream part, u_0, v_0 and w_0, and a peculiar part, u', v' and w', i.e., $u = u_0 + u'$, $v = v_0 + v'$ and $w = w_0 + w'$. In the above equation, it is assumed, without any loss of generality, that the vector normal to the boundary is parallel to the x-coordinate (Figure 3.13), thus, the velocity component u_j is normal to the flow boundary. In addition, f is the velocity distribution function which is given by the Maxwell distribution function, f^0, in the conventional DSMC as [1]:

$$f^{(0)} = V_{mp}^{-3} \pi^{-3/2} \exp\left(-v'^2/V_{mp}^2\right) \tag{3.7}$$

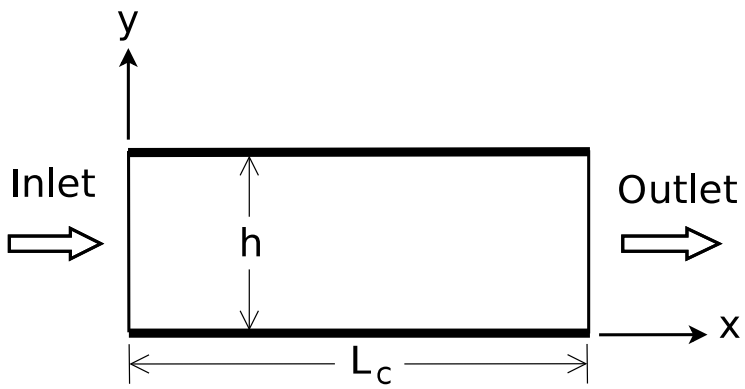

Figure 3.13: The schematic of the channel under study

where $\vec{v'} = (u', v', w')$ and V_{mp} is the most probable velocity of the molecules. The result of the integration in Equation (3.6) using f^0 instead of f is [1]:

$$\dot{N}_j^{(0)^+/-} = \frac{n_j S_n V_{mpj}}{2\sqrt{\pi}} \left(\exp\left(-s_j^2\right) \pm \sqrt{\pi} s_j \left(1 \pm erf\left(s_j\right)\right)\right) \tag{3.8}$$

where, s_j is defined as $s_j = u_0/V_{mpj}$ and u_0 is calculated from $u_0 = \sum_j Y_j u_j$ where $Y_j = \rho_j/\rho_0$. Thus, the number of molecules that enter the boundary cell face with area A at the current time step Δt is obtained from $N_j^{(0)} = \dot{N}_j^{(0)} A \Delta t$. Velocities of the entering molecules are assigned based on an acceptance-rejection method [1]. Those particles which leave the flow domain are removed and the number of molecules inside the domain is corrected correspondingly.

The proposed constant pressure boundary condition must predict the flux of particles accurately for each participating component entering the domain with regard to the imposed pressure. As it will be shown in the results, for low velocity flows, this method overestimates the molecular flux at the outlet, especially near the walls. In order to study the effect of non-equilibrium conditions near the walls on the prediction of molecular number flux, the second order approximation of the velocity distribution is used by considering the second term of Equation (3.4). According to the Chapman-Enskog solution, the second order approximation of f can be represented as a small perturbation from equilibrium state

(f^0) in the form:

$$f = f^0 + f^1 = f^0(1 + \Phi) \tag{3.9}$$

By substituting the second approximation of f into the Boltzmann equation and performing some nontrivial mathematical operations (details can be found in [28]), the general form of Φ for a binary gas mixture is obtained as:

$$\begin{aligned} \Phi_1 &= -\underline{A}_1 \cdot \vec{\nabla}(ln(T)) - \underline{D}_1 \cdot \vec{d}_{12} - 2\underline{B}_1 : \vec{\nabla}\vec{v}_0 \\ \Phi_2 &= -\underline{A}_2 \cdot \vec{\nabla}(ln(T)) - \underline{D}_2 \cdot \vec{d}_{12} - 2\underline{B}_2 : \vec{\nabla}\vec{v}_0 \end{aligned} \tag{3.10}$$

in which, subscripts 1 and 2 belong to the species and the vector $\vec{d}_{12}$ is given as:

$$\vec{d}_{12} = \vec{\nabla}X_1 + \left(X_1\frac{\rho_2}{\rho_0} - X_2\frac{\rho_1}{\rho_0}\right)\vec{\nabla}ln(p) \tag{3.11}$$

The vectors $\underline{A}$ and $\underline{D}$ and the tensor $\underline{B}$ given in Equation (3.10) are of the forms $\vec{A} = \vec{v'}A(v')$, $\vec{D} = \vec{v'}D(v')$ and $\underline{B} = \overrightarrow{v'}^{\circ}\overrightarrow{v'}B(v')$[1], where B, A and D were derived independently by Chapman and Enskog and can be found in [28]. An organized list of the equations and required steps to evaluate the function B and then functions A and D for binary gas mixtures are presented in Appendix A following the method of Tipton et al. in [49, 50].

The number flux expression using the Chapman-Enskog distribution

In order to incorporate the effect of flow variable gradients in determining the number flux of molecules, Equation (3.9), is used in Equation (3.6) which gives:

$$\dot{N}_j^{(1)^+/-} = \dot{N}_j^{(0)^+/-} - \int_{-\infty}^{\infty}\int_{-\infty}^{\infty}\int_{0/-\infty}^{\infty/0} \{2B_j + A_j + D_j\} \times f_j^{(0)} u_j \, du_j dv_j dw_j \tag{3.12}$$

where B_j contains the effect of velocity gradients and viscosity, A_j contains effects of temperature gradients and thermal diffusion, and D_j includes effects of pressure and species concentration gradients and molecular diffusion. The integration process reported in

[1] $\underline{\mathring{W}} = \underline{W} - \frac{1}{3}(\Sigma w_{ii})\,\underline{\delta}$ where $\underline{\delta}$ is the unity tensor

the literature is focused on calculating the number flux of particles crossing the Knudsen layer formed on the walls where the stream part of u_j, which is normal to the wall is set equal to zero [51, 52]. To extend the integration results to a flow boundary (inlet/outlet), general expressions for B_j, A_j and D_j functions are represented as follows based on the relations in [49, 50]:

$$\begin{aligned} B_1 &= b_1 \overrightarrow{\mathcal{C}}_1 \overset{\circ}{\overrightarrow{\mathcal{C}}}_1 \colon \vec{\nabla}\vec{v}^*_{01} \\ B_2 &= b_{-1} \overrightarrow{\mathcal{C}}_2 \overset{\circ}{\overrightarrow{\mathcal{C}}}_2 \colon \vec{\nabla}\vec{v}^*_{02} \end{aligned} \tag{3.13}$$

$$\begin{aligned} A_1 &= \left\{ a_1 \left(\tfrac{5}{2} - \mathcal{C}_1^2\right) + k_T \left\{ d_0 M_1^{1/2} \frac{\rho_2}{\rho_0} + d_1 \left(\tfrac{5}{2} - \mathcal{C}_1^2\right) \right\} \right\} \vec{\mathcal{C}}_1 \cdot \vec{\nabla} ln(T) \\ A_2 &= \left\{ a_{-1} \left(\tfrac{5}{2} - \mathcal{C}_2^2\right) + k_T \left\{ -d_0 M_2^{1/2} \frac{\rho_1}{\rho_0} + d_{-1} \left(\tfrac{5}{2} - \mathcal{C}_2^2\right) \right\} \right\} \vec{\mathcal{C}}_2 \cdot \vec{\nabla} ln(T) \end{aligned} \tag{3.14}$$

$$\begin{aligned} D_1 &= \left\{ d_0 M_1^{1/2} \frac{\rho_2}{\rho_0} + d_1 \left(\tfrac{5}{2} - \mathcal{C}_1^2\right) \right\} \vec{\mathcal{C}}_1 \cdot \vec{d}_{12} \\ D_2 &= \left\{ -d_0 M_2^{1/2} \frac{\rho_1}{\rho_0} + d_{-1} \left(\tfrac{5}{2} - \mathcal{C}_2^2\right) \right\} \vec{\mathcal{C}}_2 \cdot \vec{d}_{12} \end{aligned} \tag{3.15}$$

where k_T is the thermal diffusion coefficient, $\vec{\mathcal{C}}_j = \vec{v'}_j / V_{mpj}$ and $\vec{v}^*_{0j} = \vec{v}_0 / V_{mpj}$. The integration of functions A_j, D_j and B_j, shown on the right hand side of Equation (3.12), are labelled as ${}_B\dot{N}_j^{+/-}$, ${}_A\dot{N}_j^{+/-}$ and ${}_D\dot{N}_j^{+/-}$ for clarity. These integrations give the following results:

$$\begin{aligned} {}_B\dot{N}_1^{+/-} &= \pm \frac{n_1 b_1 V_{mp1}^2}{6\sqrt{\pi}} \left\{ 2\frac{\partial u^*_{01}}{\partial x} - \frac{\partial v^*_{01}}{\partial y} - \frac{\partial w^*_{01}}{\partial z} \right\} \exp(-u^{*2}_{01}) \\ {}_B\dot{N}_2^{+/-} &= \pm \frac{n_2 b_{-1} V_{mp2}^2}{6\sqrt{\pi}} \left\{ 2\frac{\partial u^*_{02}}{\partial x} - \frac{\partial v^*_{02}}{\partial y} - \frac{\partial w^*_{02}}{\partial z} \right\} \exp(-u^{*2}_{02}) \end{aligned} \tag{3.16}$$

$$\begin{aligned} {}_A\dot{N}_1^{+/-} &= \pm \frac{n_1 V_{mp1}}{4\sqrt{\pi}} \left\{ u^*_{01} \left(d_1 k_T + a_1\right) \exp(-u^{*2}_{01}) \right. \\ &\qquad \left. + \sqrt{\pi} d_0 k_T \sqrt{M_1} \frac{\rho_2}{\rho_0} \left\{ erf(u^*_{01}) \pm 1 \right\} \right\} \frac{\partial ln(T)}{\partial x} \\ {}_A\dot{N}_2^{+/-} &= \pm \frac{n_2 V_{mp2}}{4\sqrt{\pi}} \left\{ u^*_{02} \left(d_{-1} k_T + a_{-1}\right) \exp(-u^{*2}_{02}) \right. \\ &\qquad \left. - \sqrt{\pi} d_0 k_T \sqrt{M_2} \frac{\rho_1}{\rho_0} \left\{ erf(u^*_{02}) \pm 1 \right\} \right\} \frac{\partial ln(T)}{\partial x} \end{aligned} \tag{3.17}$$

$$
\begin{aligned}
{}_D\dot{N}_1^{+/-} &= \pm\frac{n_1 V_{mp1}}{4\sqrt{\pi}}\left\{d_1 u_{01}^{*}\exp(-u_{01}^{*2}) + \sqrt{\pi}d_0\sqrt{M_1}\frac{\rho_2}{\rho_0}\left\{erf(u_{01}^{*})\pm 1\right\}\right\} \\
&\quad\times\left\{\left(X_1\frac{\rho_2}{\rho_0} - X_2\frac{\rho_1}{\rho_0}\right)\frac{\partial ln(p)}{\partial x} + \frac{\partial X_1}{\partial x}\right\} \\
{}_D\dot{N}_2^{+/-} &= \pm\frac{n_2 V_{mp2}}{4\sqrt{\pi}}\left\{d_{-1} u_{02}^{*}\exp(-u_{02}^{*2}) - \sqrt{\pi}d_0\sqrt{M_2}\frac{\rho_1}{\rho_0}\left\{erf(u_{02}^{*})\pm 1\right\}\right\} \\
&\quad\times\left\{\left(X_1\frac{\rho_2}{\rho_0} - X_2\frac{\rho_1}{\rho_0}\right)\frac{\partial lnp}{\partial x} + \frac{\partial X_1}{\partial x}\right\}
\end{aligned}
\tag{3.18}
$$

The final value of molecular number flux derived from the Chapman-Enskog velocity distribution is then calculated from:

$$
\dot{N}_j^{(1)^{+/-}} = \dot{N}_j^{(0)^{+/-}} - \left\{{}_B\dot{N}_j^{+/-} + {}_A\dot{N}_j^{+/-} + {}_D\dot{N}_j^{+/-}\right\} \tag{3.19}
$$

The calculated value of $\dot{N}_j^{(1)^{+/-}}$ is next substituted into Equation (3.5) and the procedure described following that equation is applied to improve the pressure boundary condition for the DSMC method. Accordingly, equations used in the pressure boundary condition derived from the Maxwell (DSMC/M) and the Chapman-Enskog (DSMC/CE) distribution functions are as follows:

- DSMC/M: Equation (3.5) with Equation (3.8)
- DSMC/CE: Equation (3.5) with Equation (3.19)

Above mentioned acronyms are used for the rest of the discussions.

3.3.2 Numerical verification

The DSMC code for this study was prepared based on the algorithm proposed by Bird [1]. The modules were updated and modified for simulating flows of multi-species gas mixtures in two-dimensional channels. A schematic of the solution domain is shown in Figure 3.13. For verification purposes, the geometry of the domain for this study was selected the same as Wang et al. [15], with L = 4μm and h = 1μm. This domain was partitioned into 140×60 structured rectangular cells. A gas mixture of He-N_2 with a molar concentration of 50%-50% flows inside this channel with the flow parameters stated in Case 1 of Table 3.3. At

Table 3.3: Operational parameters of different simulation cases. For all cases, the mixture is 50%-50% by molecular number density, T_w=350K and T_{in}=300K.

	p_{in} (bar)	p_{out} (bar)	Kn_{in}	Kn_{out}	Re_{in}
Case 1	3.0	1.0	0.029	0.081	16.5
Case 2	1.0	0.5	0.090	0.199	3.1
Case 3	1.2	1.0	0.079	0.101	0.4
Case 4	0.6	0.5	0.158	0.211	0.2

the first step, velocity, temperature, heat transfer and pressure results obtained from both DSMC/M and DSMC/CE were compared to Wang et al. [15], as shown in Figures 3.14-3.15 respectively. An excellent agreement is observed for all flow properties investigated. Results of the present code for gas mixture slip flows (Kn <0.1) have also been verified in detail against Navier-Stokes simulations and reported in Qazi Zade et al. [45], which will not be repeated here.

3.3.3 Results and discussion

As indicated in Section 3.3.1, calculating $\dot{N}^+$ and $\dot{N}^-$ is the first step for applying the DSMC pressure boundary condition. Since the stream velocity is in the positive direction, $\dot{N}^+$ has a much greater value than $\dot{N}^-$ and therefore, using a higher order distribution is more critical for calculating $\dot{N}^-$. Hence, the rest of the discussion is focused on $\dot{N}^-$ which is used for implementing the outlet pressure boundary condition. It is observed in Figures 3.14-3.15 that adopting the Chapman-Enskog distribution for Case 1 does not affect the temperature and velocity fields. The reason lies in the high pressure ratio of this case which leads to a high velocity at the channel outlet. This means that the number flux of molecules leaving the domain (the value of $\dot{N}^+$ in Equation (3.5)) is so high that the outlet velocity is almost unaffected by the number flux of molecules diffusing upstream

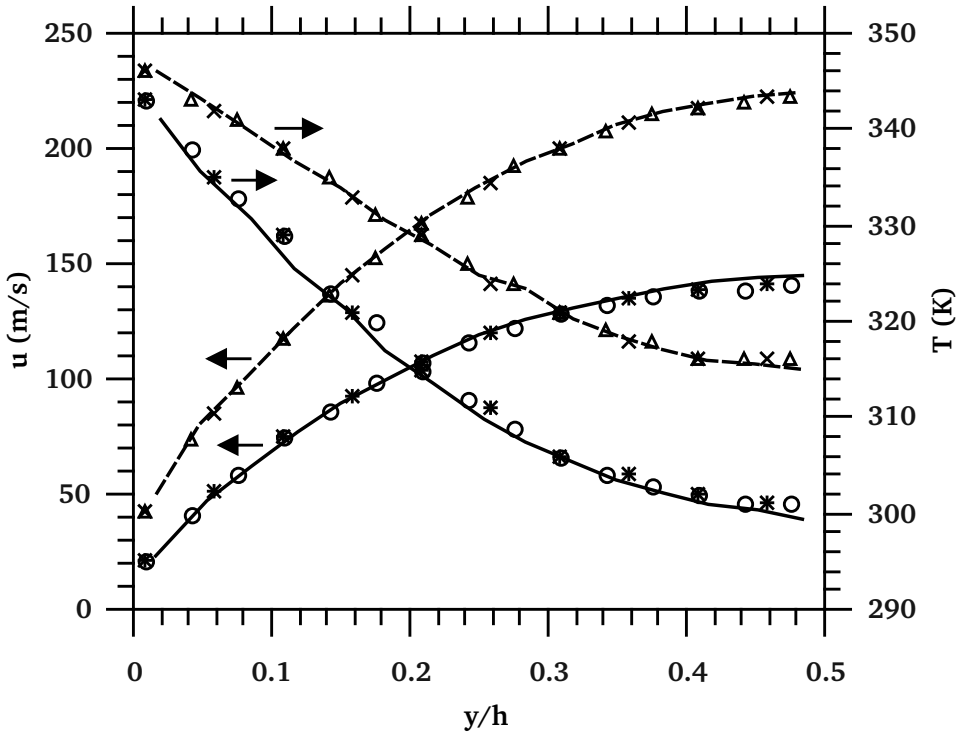

Figure 3.14: Verification of velocity and temperature cross-sectional profiles for Case 1 against Wang et al. [15] reported at $x/L_c = 0.1$ ("$\circ$" from Maxwell, "$*$" from Chapman-Enskog and continuous line [15]) and $x/L_c = 0.7$ ("$\triangle$" from Maxwell, "$\times$" from Chapman-Enskog and dash line [15]).

(the value of $\dot{N}^-$ calculated from Equation (3.19)) at the boundary. Applying a high temperature at the walls has the same effect since the resulting gas expansion produces a high stream velocity at the outlet. Decreasing the pressure ratio will increase the value of $\dot{N}^-$ and thus magnify the role of the boundary condition. Generally, the influence of a pressure boundary condition on a flow depends on Kn and the stream velocity (or p_r). In order to study their effects, four different cases are considered here as listed in Table 3.3: Case 1 deals with high stream velocity (p_r=3.0) and low Kn; Case 2 deals with high stream velocity (p_r=2.0) and high Kn; Case 3 deals with low stream velocity (p_r=1.2) and low Kn; and Case 4 deals with low stream velocity (p_r=1.2) and high Kn. The Kn range of these

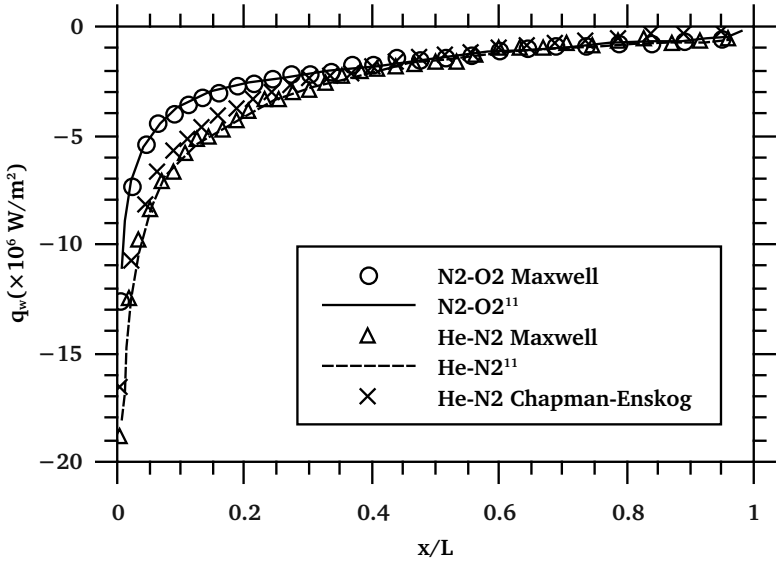

(a)

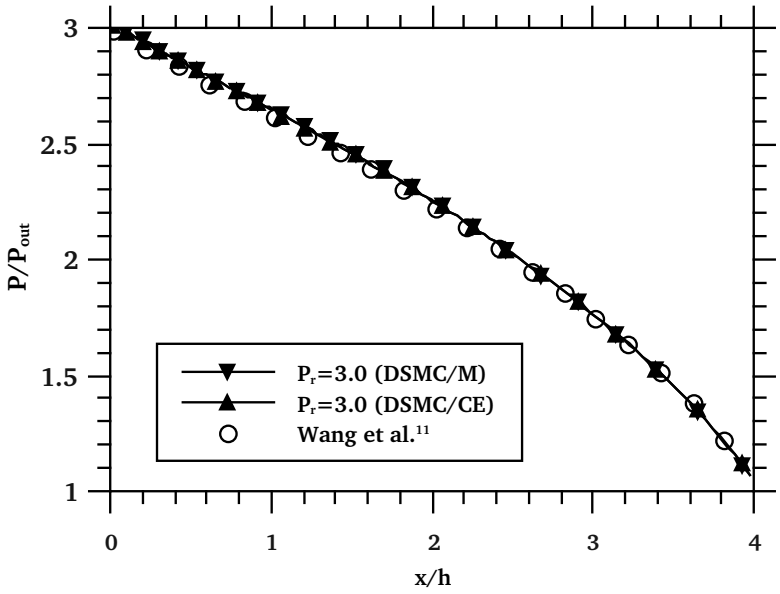

(b)

Figure 3.15: Comparison of (a) wall heat flux and (b) pressure distribution obtained from DSMC/M and DSMC/CE for Case 1 with Wang et al. [15] (negative heat flux represents heat being extracted from the wall).

cases covers the slip and the initial part of the transition regimes which are practically more important. The authors could not find any experimental data with the same or similar properties as Cases 2-4 in the available literature for verification purposes. An option is verification against DSMC results which are obtained from a full order velocity distribution used in the applied pressure boundary condition. For this purpose, a channel with the same hight but a length L_{ext} greater than $L_c = 4.0\mu$m was simulated and the results of the first 4.0μm of the channel are considered as the desired data, here forth called the "reference data". This way, the velocity distribution and hence $\dot{N}^-$ are naturally evaluated by DSMC itself across the channel at 4.0μm, and therefore, have a full order accuracy. In order to keep the pressure distribution throughout the first 4.0μm of the channel the same as the case under study, the pressure at 4.0μm was kept at the corresponding value by imposing an appropriately lower pressure at the outlet. This was achieved by correcting an initial guess for the outlet pressure as the simulation marched to steady state conditions. It should be noted that the outlet pressure is imposed by either DSMC/M or DSMC/CE. Therefore, possible inaccuracies present in the evaluation of $\dot{N}^-$ can affect reference results by upstream diffusion. To prevent this, the extended channel is lengthened and hence the pressure ratio and the outlet velocity are increased. As discussed earlier for Case 1, if the outlet velocity is high enough (adequately long channel) the value of $\dot{N}^-$ is negligible.

In order to determine whether the velocity distribution function affects the evaluation of $\dot{N}^-$, the difference between the values of $\dot{N}^-$ crossing the vertical face of the cells adjacent to the walls obtained from DSMC and the Maxwell distribution are shown in Figure 3.16 for Case 2 as an example. The values corresponding to DSMC were obtained by direct sampling of the number of molecules crossing the cell face. For calculating $\dot{N}^-$ values from the Maxwell distribution (zero line) equations of DSMC/M and flow properties from the DSMC simulation were used. As expected, the DSMC results deviate from equilibrium conditions with the maximum departure around 8% near the outlet. This deviation suggests that a velocity distribution with a higher order than the Maxwell distribution (which is used in the conventional pressure boundary condition, DSMC/M) is required to calculate the molecular flux accurately. As will be shown, this is especially necessary in a correct implementation of a constant pressure boundary condition for gas mixtures. Figure 3.16 also shows that non-equilibrium effects are higher near the outlet which is due to higher rarefaction effects

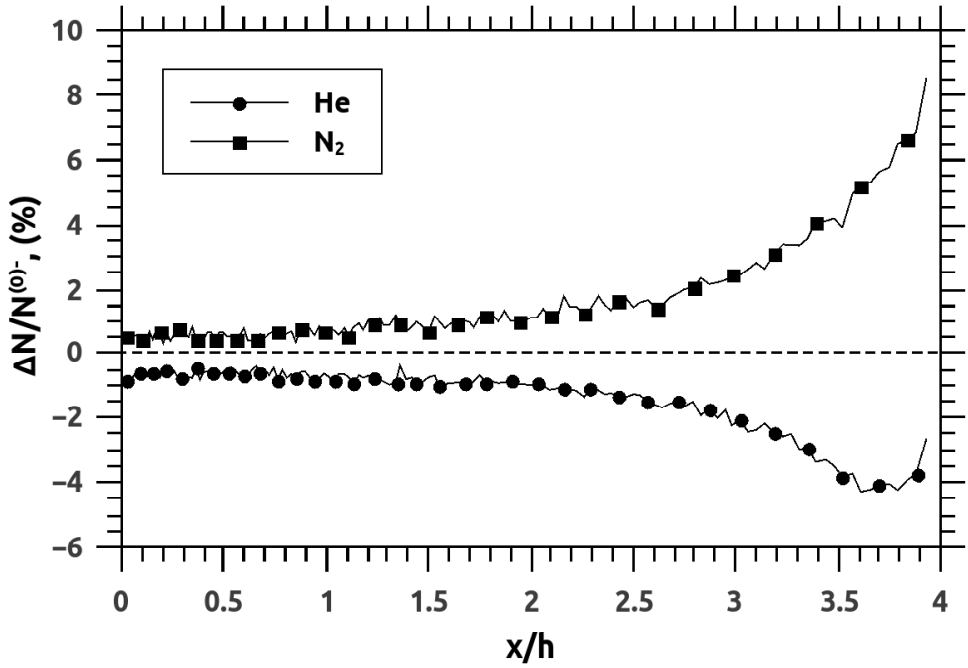

Figure 3.16: Variations of $\Delta N = \dot{N}^{-}_{DSMC} - \dot{N}^{(0)-}$ relative to $\dot{N}^{(0)-}$ along the channel for Case 2; $\dot{N}^{-}_{DSMC}$ is the number flux calculated by DSMC and $\dot{N}^{(0)}$ the one calculated from DSMC/M crossing the vertical face of the cells adjacent to the walls.

present there in this flow. This fact is clearly seen in Figure 3.17 in which Kn continuously increases along the channel. These non-equilibrium effects are taken into account by first order using the Chapman-Enskog velocity distribution (DSMC/CE), which should result in a behavior closer to the DSMC reference solution. Figure 3.17 also shows that simulation results are insensitive to DSMC/M or DSMC/CE for the high speed conditions of Case 1 and Case 2.

Figure 3.18 presents the contour plots of the He concentration in a gas mixture of He-N_2 for Case 2 obtained from DSMC/M and DSMC/CE. As shown, the concentration distribution is almost the same for both methods. A notable point is an accumulation of N_2 between the middle and the outlet of the channel. This behaviour can either be a physical phenomenon or produced by inaccuracies in calculating $\dot{N}^{-}$ using DSMC/M or

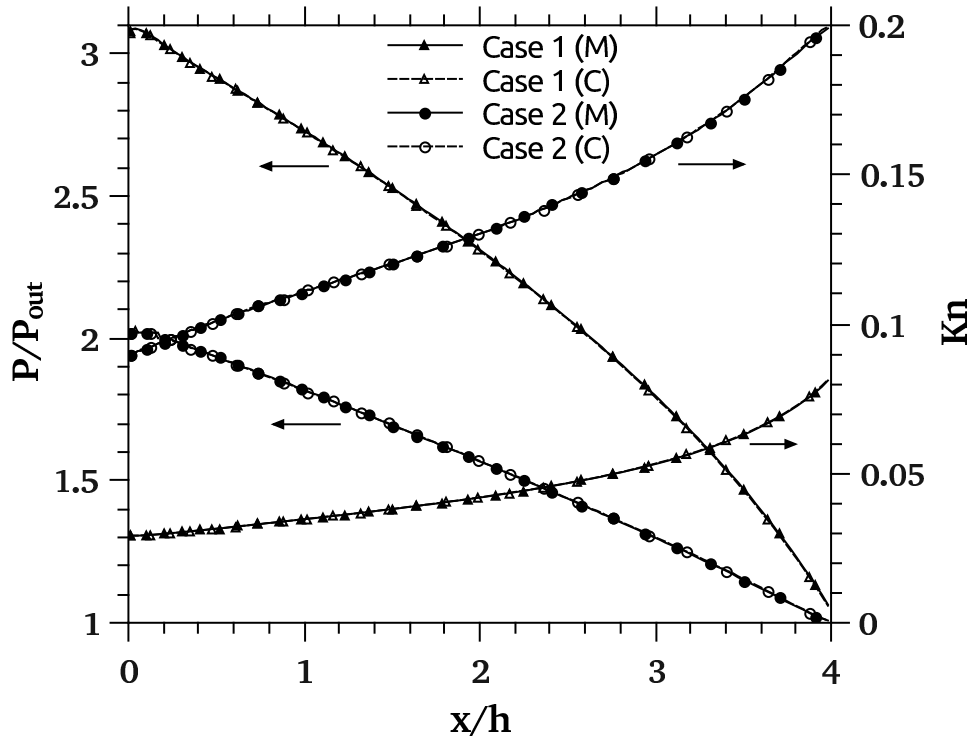

Figure 3.17: Pressure and Kn distributions for higher speed cases, i.e. Case 1 and Case 2; (M) and (C) represent the results of DSMC/M and DSMC/CE respectively.

DSMC/CE. In order to resolve this, the results are compared to the "reference data" as indicated before.

Concentration results of simulating two extended channels with L_{ext} of 5.0μm and 6.0μm (L_c+h and L_c+2h respectively) are presented in Figure 3.19. In both cases, the pressure at 4.0μm is kept at 0.5bar as described earlier. A N_2 accumulation zone similar to the one seen in Figure 3.18 still exists in 5.0μm long channel of Figure 3.19(a); however, it has moved to a location beyond 4.0μm. In addition, this accumulation zone vanished completely in the 6.0μm channel of Figure 3.19(b). This shows that such accumulation was a result of inaccuracies in the calculation of $\dot{N}^-$ used in the outlet pressure boundary condition. It is worth noting that the pressure distributions in the first 4.0μm of both channels shown in Figure 3.19 are the same. Our further studies revealed that the value

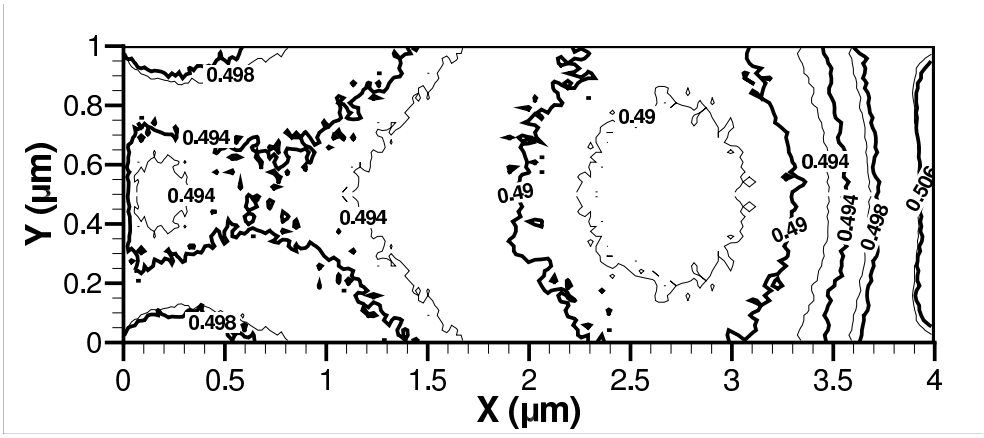

Figure 3.18: The contour plot of the number density of He in gas mixture flow of He-N_2 for Case 2; thicker line: DSMC/M and thinner line: DSMC/CE

of $\dot{N}_j^-$ is underestimated for the species with heavier molecules. Furthermore, the pressure ratio at which such behaviour emerges, depends directly on the molecular masses of the species in the gas mixture (p_r ≈2.5 for He-N_2 and p_r ≈1.5 for N_2-O_2). The 6.0μm channel of Figures 3.19(b) is long enough that the high velocity produced at the outlet minimizes the effect of $\dot{N}_j^-$ as discussed earlier in this section. Therefore, results of the first 4.0μm of this case is used as the reference solution (DSMC/R) for the rest of the present study.

Contour plots of the He concentration for the low velocity cases, i.e., Case 3 and Case 4, are presented in Figure 3.20(a) and Figure 3.20(b) respectively. In this figure, the results of DSMC/M and DSMC/CE (shown in the lower half of the channel) and the reference data (shown in the upper half of the channel) are compared to each other. As shown, the concentration is predicted almost the same using DSMC/M and DSMC/CE for lower Kn, i.e., Case 3. For higher Kn, Case 4, however, results of the two methods considerably deviate from each other both at the inlet and the outlet and DSMC/M fails to follow the reference data. The trend of DSMC/CE results are closer to the reference and as well, it is more accurate. The effectiveness of using DSMC/CE for high Kn and low velocity flows is also seen in Figure 3.21. This figure shows pressure and Kn changes along the mid-plane of the channel for lower speed cases. For Case 3 with lower Kn, DSMC/M and DSMC/CE

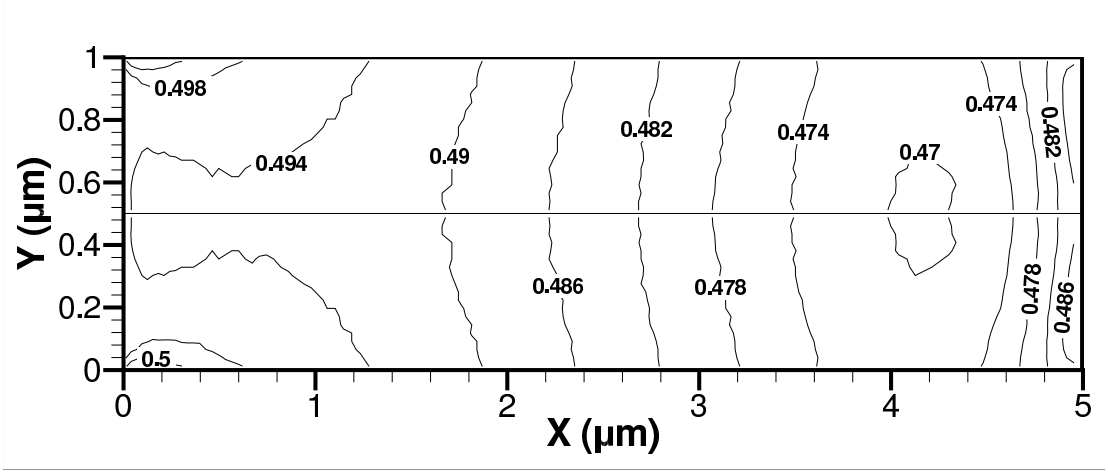

(a)

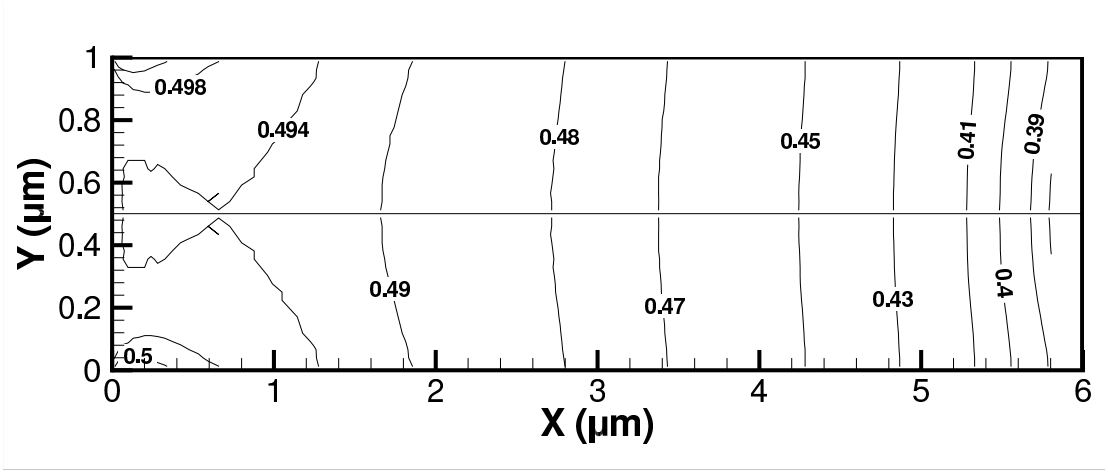

(b)

Figure 3.19: Contour plots of the He concentration for two extended channels with different L_{ext} of (a) 5.0μm and (b) 6.0μm and properties of Case 2.

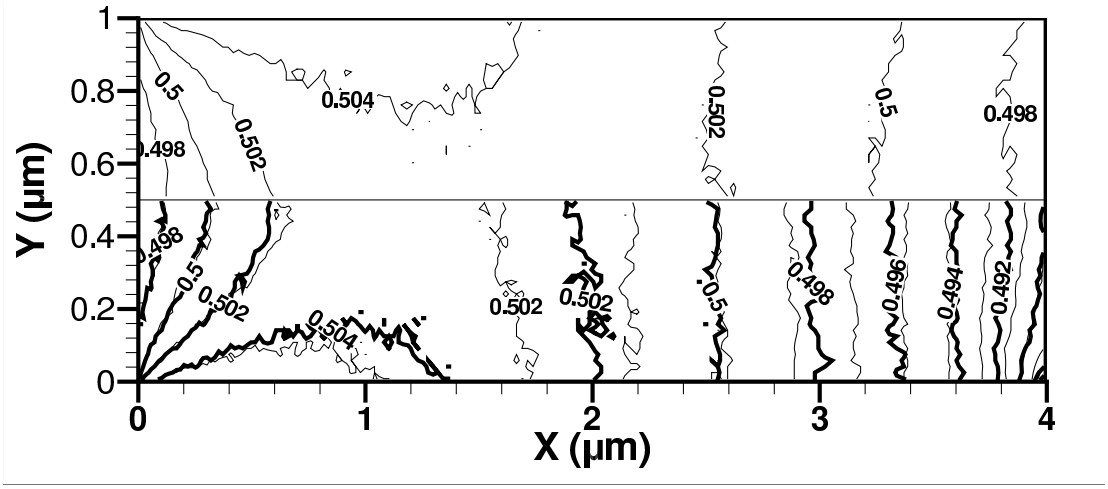

(a)

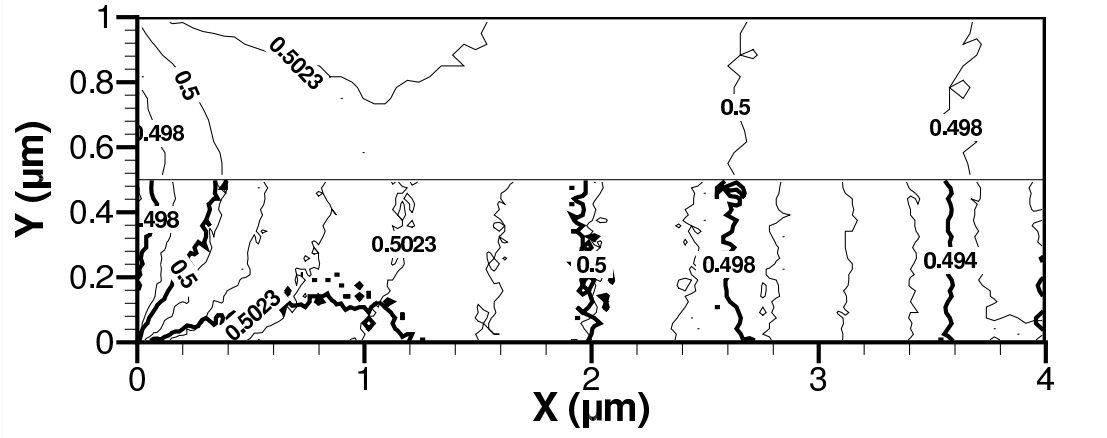

(b)

Figure 3.20: Contour plots of the He concentration calculated from DSMC/M (thinner lines, lower half), DSMC/CE (thicker lines, lower half), and the reference data (upper half) for (a) Case 3 and (b) Case 4.

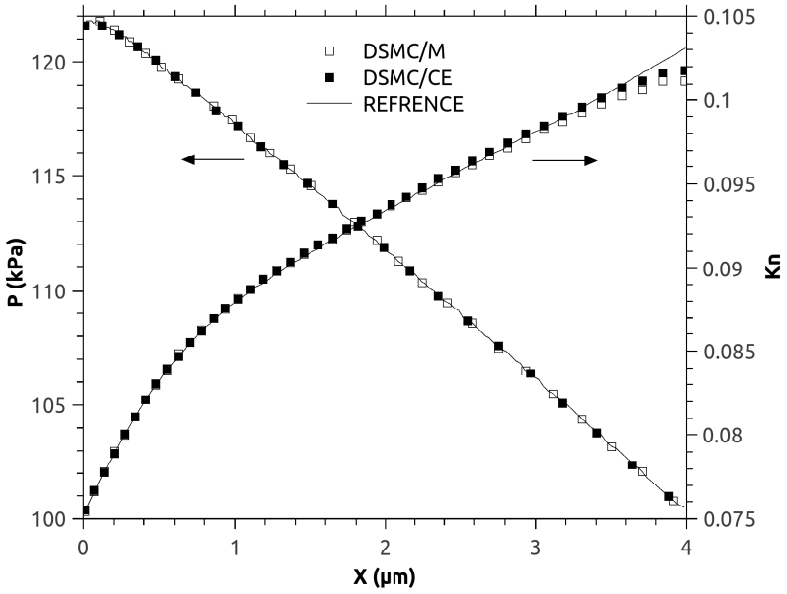

(a)

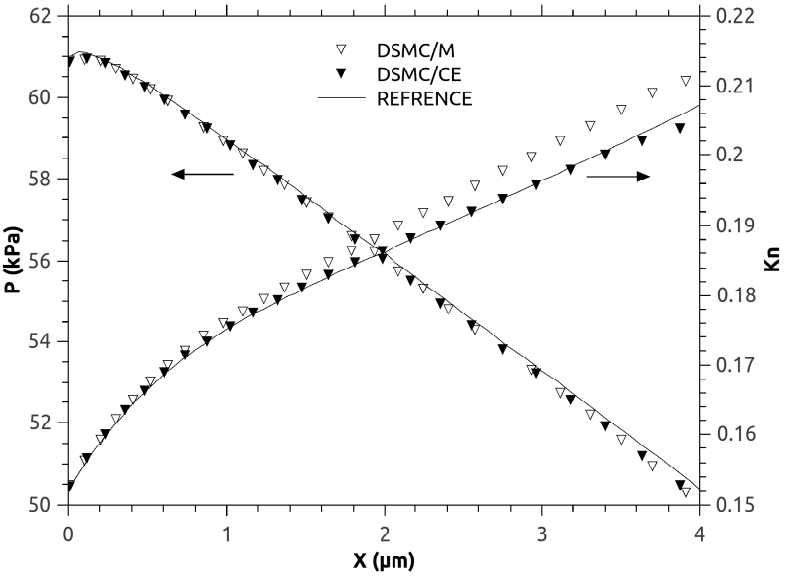

(b)

Figure 3.21: Variations of pressure and Kn along the mid-plane of the channel for lower speed cases, i.e. (a) Case 3 and (b) Case 4.

simulations are almost the same, but DSMC/CE results for Kn are closer to the reference data near the outlet. However, as shown in Figure 3.21(b), DSMC/M digresses considerably from the reference results at higher Kn (Case 4) starting early in the channel. On the other hand, using DSMC/CE results in almost exact Kn predictions. This observation that both DSMC/CE and DSMC/M calculate the pressure distribution accurately conveys the fact that number of molecules entering the channel at the outlet boundary is predicted well by both methods; however, the composition of these molecules for participating species is only calculated correctly by the higher order method, DSMC/CE, and that is why only DSMC/CE is successful in simulating Kn accurately. This is fully consistent with the results shown in Figure 3.20.

So far it is determined that adopting DSMC/CE works for low velocity and high Kn flows; however, it can improve the results of high velocity or low Kn cases as well. Figure 3.22(a) shows that the slip velocity calculated by both DSMC/CE and DSMC/M deviate from the reference solution near the outlet; however, applying DSMC/CE results in closer behaviour to the reference data compared to DSMC/M. As expected, employing the Chapman-Enskog distribution leads to partial improvements. It is worth noting that a similar behavior has been observed in single component gas flows modelled with the Maxwell pressure boundary condition [13, 53]. This supports the idea of the current study that the velocity distribution function plays an important role in implementing pressure boundary conditions.

Similarly, pressure values obtained from DSMC/CE are closer to the reference solution for Case 2 (Figure 3.22(b)). As shown, the results obtained from both distributions are essentially the same for the rest of the channel and agree well with the reference data.

Another observation from Figure 3.22(a) is the initial unexpected drop in the slip velocity right after the inlet before it begins to increase with increasing Kn along the channel. This behaviour, which is present in isothermal flows as well, is magnified as the inlet Kn increases. It is in fact a numerical artifact caused by the uniform pressure enforced at the inlet. As mentioned before, uniform pressure is the most practical inlet/outlet boundary condition for DSMC in the absence of reservoirs. However, a perfectly uniform pressure across the channel cross-section is not physically justified especially close to the walls. Therefore, enforcing such a condition at the inlet results in an entrance adjustment

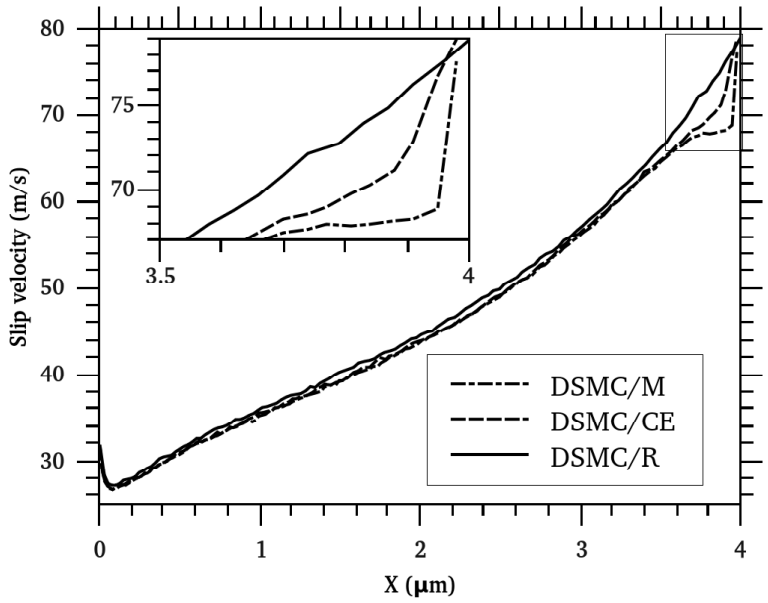

(a)

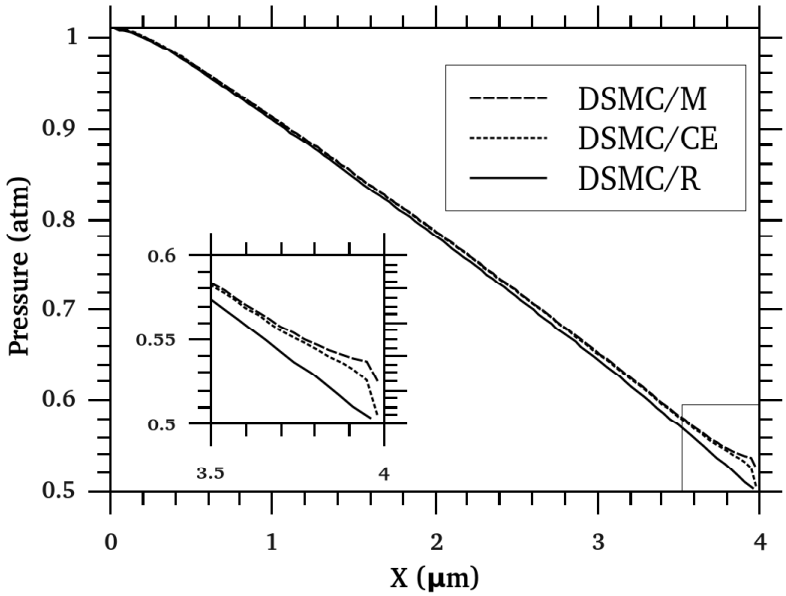

(b)

Figure 3.22: Velocity slip (a) and pressure variations (b) along the channel wall for Case 2 based on the Maxwell distribution (DSMC/M), the Chapman-Enskog distribution(DSMC/CE), and the reference data (DSMC/R).

zone, where pressure and velocity distributions transform into their physical form. A solution suggested by Roohi et al. [38] is to consider 10% of the channel as an entrance region with specular molecular reflection at the walls. This increases the statistical scatter in the results as well as the computation time, and therefore, not followed in this study. Similar slip velocity drops close to the inlet have also been reported by Wang and Li [14] and Fang and Liou [13].

For further understanding of the velocity distribution effects on calculating the molecular number flux, a comparison was made similar to the one in Figure 3.16, including the number flux obtained directly from DSMC/CE, as shown in Figure 3.23. For Case 2, as seen in Figure 3.23(a), the Chapman-Enskog distribution results follow the same trend of DSMC and can accurately replicate the DSMC number flux results in the entrance region where rarefaction effects are comparatively lower. The results from the two methods, however, depart from each other along the channel with the maximum difference near the outlet, and this difference is higher for He molecules. Figure 3.23(b) shows the same comparison for Case 4. It can be seen that DSMC/CE produces a more accurate distribution for He in comparison to Case 2. This figure shows that DSMC/CE results for N_2 are higher than DSMC and generally mean values of the difference between DSMC/CE and DSMC results is less that one third of the corresponding values for Case 2. This explains why DSMC/CE results are closer to the reference data (see Figures 3.20 and 3.21). From Figure 3.23, it is also clear that the value of $\dot{N}_j^-$ for He, calculated from DSMC/CE or DSMC for Case 2 is lower than the DSMC/M results and that is why the value of $\dot{N}_j^-$ is overestimated for He in Figure 3.18. Similar results have been achieved for H_2 in a gas mixture of O_2-H_2. These observations again suggest that for the species with heavier molecules, a velocity distribution of higher order than the Chapman-Enskog is required in order to match the distribution naturally produced by DSMC. Due to the complexity and the numerical effort required for the implementation of even the first order correction, a utilization of higher order terms seems not feasible. Furthermore, higher order distribution functions will not necessarily give the desired results for the conditions of Case 2.

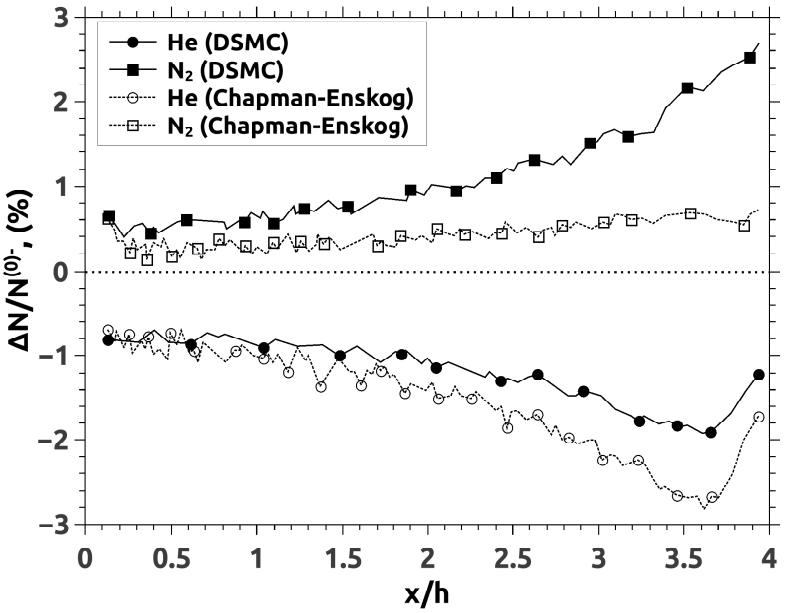

(a)

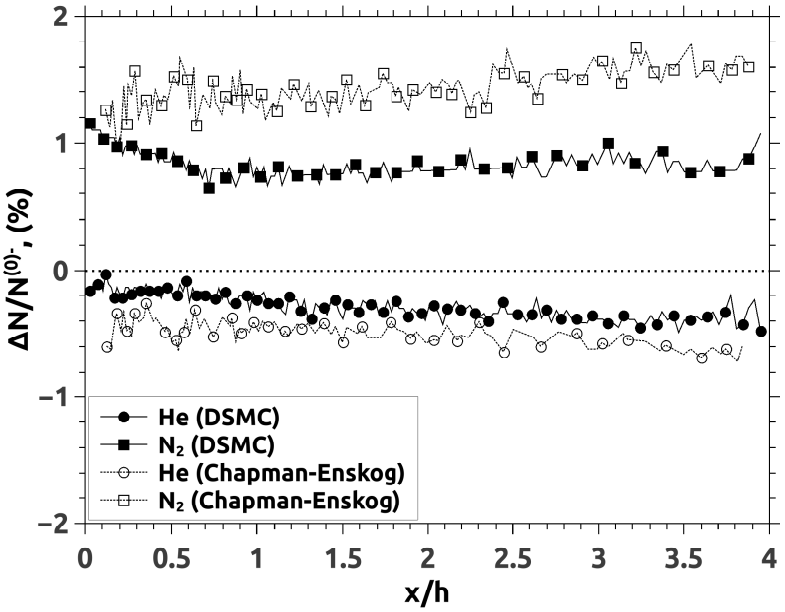

(b)

Figure 3.23: The variation of $\Delta N = \dot{N}^{-} - \dot{N}^{(0)-}$ relative to $\dot{N}^{(0)-}$ along the channel for (a) Case 2 and (b) Case 4; $\dot{N}^{(0)-}$ is the number flux calculated from the Maxwell (DSMC/M) distribution.

3.3.4 Summary

First, a pressure boundary condition has been proposed for the DSMC method in order to simulate multi–species gaseous micro–flows. This pressure boundary condition was implemented in the DSMC code previously verified against Navier–Stokes. The results were also compared to other available DSMC results reported in the literature. Next, the accuracy of the proposed pressure boundary condition was improved by adopting the Chapman–Enskog distribution. Some cases with different Re and Kn ranges were studied using the new boundary condition, and the results revealed that the velocity distribution plays an important role in accuracy of the calculations at flow boundaries. In addition, it was found that the molar fraction data obtained from the new boundary condition are more accurate for low velocity and high Knudsen number (Kn) flows.

Chapter 4

Heterogeneous catalytic reacting flows in transition regime

In this section, the intention is twofold: (1) to develop a numerical model applicable for coupling surface chemical reactions and the flow field for highly rarefied flows (transition flows) based on DSMC capabilities, and (2) to study the effects of geometrical and flow specifications on the behaviour of catalytic reactions and as well on the flow variables.

The method used here is specially developed to couple the stochastic nature of DSMC outputs with the conventional surface catalytic reaction analysis for steady-state conditions and is described in Section 4.1. The resulting method is first used to simulate a flow of a lean H_2/Air flow in a parallel channel with platinum coated walls, and the results are compared to those obtained from Navier-Stokes equations with slip-jump boundary conditions. Next, the effects of different geometrical and boundary specifications are investigated using the verified code.

4.1 Modelling surface catalytic chemical reactions

Heterogeneous chemical reactions take place on the catalytic walls of the channel. In the present work, chemical reactions on the walls are modeled using a standard produc-

tion/consumption ODE system. This provides the flexibility of using available mechanisms and taking advantage of DSMC. The general form of a production/consumption ODE is:

$$\frac{d\theta_i}{dt} = \Sigma k_j \theta_m \theta_n + r_{ads,i} - r_{des,i} \tag{4.1}$$

where $\Sigma k_j \theta_m \theta_n$ is the summation of Arrhenius reaction rates over all the sub–reactions which participate in production/consumption of the species "i". Thus, the range of "j" can vary for different species. $r_{ads,i}$ and $r_{des,i}$ are adsorption and desorption rates respectively. The number of ODEs for a chemical reaction is equal to the number of species involved in the reaction, making an ODE system for an available reaction mechanism. Such an ODE system has mostly stiff characteristics and requires a special solver in which the variable time step method is utilized. The adsorption and desorption terms in Equation (4.1) are responsible for exchanging molecules between the surface and the gas. These terms are treated differently in the method introduced in this work to comply with the DSMC algorithm. In general, the adsorption term for species i has the form:

$$r_{ads,i} = K_{ads,i} \left(X_{Pt^*}\right)^m \tag{4.2}$$

where, r_{ads} is the rate of adsorption (mol/m^2·s), X is the molar concentration on the surface (mol/m^2), subscript Pt^* denotes the free platinum catalytic sites, superscript m is the stoichiometric coefficient of the surface species, and K_{ads} is the Arrhenius equivalent rate constant which is of the form [54]:

$$K_{ads,k} = \frac{\gamma_k}{\Gamma^m} F_k \tag{4.3}$$

where, γ_k is the sticking coefficient of the species k, Γ is the density of total catalytic surface sites (mol/m^2) and F_k is the Mean Collision Rate (MCR) of the species k with a unit area of the catalytic surface (mol/m^2·s). Equations (4.2) and (4.3) imply that a molecule hitting the surface is adsorbed with two probabilities: the sticking factor, γ_k, which is the probability of being adsorbed if the molecule hits a free site, and the probability of hitting a free site calculated from $(X_{Pt^*}/\Gamma)^m$. In the continuum methods, F_k is calculated by a relation derived from the Maxwell distribution. Some correction coefficients are also applied to account for non-equilibrium effects on the surface due to adsorption. In the DSMC method, however, F_k is directly sampled for each boundary cell

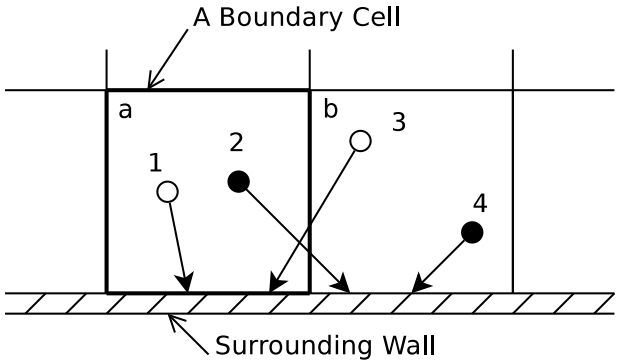

Figure 4.1: Different states of molecular collisions with the wall. This figure shows four particles initially located in two boundary cells and hitting a surrounding wall. If the collision is sampled based on initial position, particles 1 and 2 are considered to hit the wall inside cell "a" and as well particles 3 and 4 for will be considered for cell "b". However, if the collision is sampled based on the collision spot on the surface, particles 1 and 3 will be sampled for cell "a" and particles 2 and 4 are sampled for cell "b". Obviously the latter method should be used to evaluate MCR correctly.

by counting the number of simulating particles crossing catalytic walls during one Δt. This way, non-linearity inside the Knudsen layer and the effect of molecular adsorption on the velocity distribution right above the surface are taken into account. Special care should be taken for sampling F_k to collect the information of the molecules hitting the surface based on the location at which the collision takes place on the surface (see Figure 4.1). If the sampling is performed based on initial position, the collision distribution will not be captured correctly. This is especially important for those cells located close to the inlet and the outlet boundaries where directed movement of molecules increases the chance of error.

For the numerical implementation, $r_{ads,i}$ is calculated at each Δt. This term is directly used in the ODE system for simulating surface reactions. On the gas side, the number of species i molecules to be adsorbed on each cell is evaluated from $r_{ads,i}\Delta t A A_v/S_n$ where, A is the area of the cell face at the wall surface and A_v is Avogadro's number. This value is accumulated for each species and each cell adjacent to the walls and a simulating particle

hitting the wall surface is adsorbed if the accumulated value is greater than one (since a partial molecule is meaningless). In case of an adsorption event, accumulated value of the corresponding species is reduced by one and the simulating particle is removed from the solution domain, otherwise, it will be reflected back to the gas using a diffuse approach (in random direction towards the gas and with a random velocity).

Adsorbed atoms or molecules (particles) can be activated due to an adequately high temperature and diffuse to available and immediate neighboring catalytic sites. Depending on the wall temperature magnitude, activated particles can also diffuse beyond immediate catalytic sites [55]. This is a short–range surface diffusion and continues until the adsorbed particle reaches another adsorbed particle suitable for a chemical reaction. The short–range surface diffusion directly affects the reaction rate [56] and is considered in the reaction rate constants included in the reaction mechanism. A long–range surface diffusion derived by species concentration gradients on the surface can also be expected. Although the surface diffusion coefficients for the species studied in this work are considerable at high temperatures on a smooth platinum surface (10^{-2} cm^2/s for oxygen at 650°C [57]), it dramatically decreases for porous platinum catalysts to a point that it can be neglected (3×10^{-7} cm^2/s for oxygen at 730°C [57]). Considering the fact that porous platinum configurations (e.g. platinum nano particles deposited on a substrate) are mostly used for platinum catalytic surfaces due to their higher surface area, the long–range diffusion is not studied in the present work. Good agreements between numerical simulations and experimental data for larger channel geometries have also been observed without considering the surface diffusion [58, 42]. Moreover, as of now, a reliable and complete data for surface diffusion coefficients is not available due to experimental complexities. Reported values have a variation of one or two orders of magnitude [57] preventing accurate analyses in this regard.

The desorption process is treated using an Arrhenius rate on the surface based on the chemical reaction mechanism. On the gas side, the number of molecules desorbing from the surface is calculated from $r_{des}\Delta t A A_v/S_n$ in which, r_{des} is the rate of desorption. This value is not necessarily an integer number, and hence, values of $r_{des}\Delta t$ are accumulated for each gas species. A molecule leaves the surface in a diffuse manner as soon as the corresponding accumulation is greater than one.

The resulting stiff ODE system is solved over a large enough time period to reach the

steady-state solution. Initial values for the surface concentrations, X_k, are adopted from the previous time step. This ODE system is solved using the DVODE (Variable-coefficient Ordinary Differential Equation solver) package [59].

In the next section, results of the DSMC code is verified against corresponding results of a Navier-Stokes code developed in a different study [21] for a reacting micro-flow in the slip flow regime.

4.2 Problem definition

The flow between parallel plates is studied in this section. The inlet boundary condition of each channel is considered as constant mass flux $\dot{m}''_{in}$ calculated from dividing $\dot{m}_{in}$ by the total perforated area. Molar concentrations X_i and then number densities n_i for the fuel/air mixture species are evaluated using the specified ϕ and the pressure taken from the cell adjacent to the inlet. The stream velocity is calculated from $u_{in} = \dot{m}''_{in}/\rho$, where ρ is the density of the gas mixture taken from the interior cells. Using values of n_i and u_{in}, molecular flux of each species towards downstream $\dot{N}_i^+$ is determined from [1]

$$\dot{N}_i^+ = \frac{n_i S_n V_{mp,i}}{2\sqrt{\pi}} \left(\exp\left(-s_i^2\right) \pm \sqrt{\pi} s_i \left(1 \pm erf\left(s_i\right)\right)\right) \tag{4.4}$$

where, $s_i = u_{in}/V_{mp,i}$ and $V_{mp,i}$ is the most probable molecular velocity of the species i. Thus, the number of molecules that enter the boundary cell face with area A at the current time step Δt is obtained from $N_i = \dot{N}_i^+ A \Delta t$. Velocities of the entering molecules are assigned based on an acceptance-rejection method [1]. Due to the micro/nano geometry of the channels, the flow encounters high rate of upstream diffusion. Therefore, many particles leave the channel at the inlet boundary. If those particles belong to fuel/air species (reactant or neutral), they are removed and the number of molecules inside the domain is corrected correspondingly. Otherwise, if they belong to the product species, they will return to the channel anyway after entering the inlet plenum. This is because no molecule in reality has the opportunity to continue moving upstream by diffusion and enter the pressure tanks. Therefore, all such molecules will inevitably return to the channels with the inlet stream. In other word, the molecular flux of the product species p diffusing out

at the inlet $\dot{N}_p^-$ is equal to the molecular flux of the same type entering the channel with the stream $\dot{N}_p^+$. This means that mass flux of each product species is equal to zero at the inlet since [22]

$$n_p u_p = \dot{N}_p^+ - \dot{N}_p^- \tag{4.5}$$

It is obvious that if $\dot{N}_p^- = \dot{N}_p^+$, molecular flux of species p, $\dot{N}_p = n_p u_p$ becomes zero. Hence, the inlet boundary condition for product species is $\dot{N}_p = 0$. In order to impose this condition, time average value of $\dot{N}_p^-$ is evaluated by sampling number of molecules leaving the channel at the inlet during the simulation. This value is equal to $\dot{N}_p^+$ to satisfy the zero molecular flux condition. Having $\dot{N}_p^+$, number of species p molecules entering at the inlet can be calculated using the same procedure described under Equation 4.4.

A constant pressure is a common outlet boundary condition in channel flow modelling. In addition, pressure is a controllable flow property in practice since a number of parallel reaction channels typically discharge to a common reservoir maintained at a constant pressure in micro-reactors. The gas entering a reactor channel at the outlet is composed of different species and this makes it difficult to introduce an appropriate DSMC boundary condition which can account for multi-species diffusion while maintaining a constant pressure. The difficulty here is that in the conventional pressure boundary conditions, a Maxwellian velocity distribution is used which is of zero order while DSMC requires a distribution with a higher order of accuracy. Furthermore, modelling reasonably large reservoirs at the channel exit is numerically very expensive. These issues have been addressed and a solution was proposed in a different study [22]. In this approach, a non-catalytic extension with a proper length is added to the outlet of the channel. The pressure at the outlet of the extension is kept at a suitable lower value in order to obtain the desired pressure at the outlet of the channel. This way, DSMC produces an accurate distribution at the channel outlet cross section.

A constant temperature is considered on the catalytic walls. Due to small length of the channels used in this study and high thermal conductivity of platinum, temperature gradients at the wall along the channel are expected to be reasonably low and thus, the constant temperature assumption is justified. In order to keep the wall temperature at a constant value some of the reaction heat production is transfered to the walls and is removed via heat conduction through the walls. The amount of this heat is obtained

following similar procedure under Equation 3.3 and is calculated from:

$$q'' = \Delta H + \frac{\sum_{i=1}^{N_{r+d}} e_i^* - \sum_{i=1}^{N_g} e_i}{A \cdot \Delta t} \tag{4.6}$$

where ΔH is the heat of reaction produced on the surface of the incident cell and $\sum_{i=1}^{N_{r+d}} e_i^*$ covers both reflected and desorbed molecules.

The DSMC simulation is considered as converged when the relative difference of the mass flow at the outlet and at the inlet boundaries is less than 1%. Reasonable level of statistical scatter was obtained using this criterion. DSMC simulations were carried out in series on the SHARCNET computational network. The computational time for each DSMC run was typically about 10-14 days. The Navier–Stokes simulations were run on a desktop with an Intel® processor at 3GHz speed and each run took about 4-5 days.

4.3 Verifications

The DSMC code used in the present work has already been verified against other available DSMC and Navier-Stokes results for non-reacting micro-channel flows [21]. The Navier–Stokes code is the same one used in [60]. The Navier–Stokes equations, slip–jump boundary conditions and a brief description of the numerical implementation are demonstrated in Appendix C. For modeling surface chemical reactions using continuum methods, a concentration jump boundary condition should also be considered on the walls [61]. The formulation of this boundary condition employed for the present work is shown in Equation C.8 and is adopted from Qazi Zade *et* al. [42]. It is worth mentioning here again that the input data for Navier–Stokes formulations are fluid properties and the accommodation coefficient taken from experimental resources. Thus, the DSMC method and the Navier–Stokes simulations employed here are prepared independently.

Here, the DSMC method is applied to a gas flow undergoing catalytic hydrogen oxidation between parallel plates with 4μm separation height and 40μm length. The platinum coated walls have a constant temperature of 1000K, and the outlet of the channel is kept at atmospheric pressure. One half of the channel is simulated and the symmetry condition

(specular reflection of molecules) is applied at the midplane. This domain is divided into 440×55 cells. 6×10^5 simulating molecules were initially distributed among the cells and the time step is set equal to 6×10^{-12}s. For the conditions described, Kn varies from 0.02 at the inlet to 0.08 at the outlet. A lean Hydrogen/Air mixture with an equivalence ratio of ϕ=0.28 flows into the channel at an inlet temperature of 300K and a constant mass flux of 25kg/m^2·s. The inlet mass flux is distributed among fuel/air species using the method described in Section 4.2. This is done in such a way that the composition of the inlet fuel/air mixture follows reactants of the reaction: $2\phi H_2+(O_2+3.76N_2)\rightarrow 2\phi H_2O+3.76N_2+(1\text{-}\phi)O_2$. The heterogeneous reaction mechanism used in the present work is shown in table 4.1. The total density of catalytic sites is $\Gamma=2.7\times10^{-5}$ mol/m^2.

In the present work, homogeneous reactions in the gas are neglected due to the small size of the channel. The reason for neglecting gas reactions in this study is that the probability of proper molecular collisions leading to a chemical reaction is very low due to the rarefaction that the contribution of gas reaction to the total reactions (gas and surface reactions) is negligible. The study conducted by Qazi Zade *et* al. [60] clearly shows that for flow conditions similar to the present study, homogeneous hydrogen consumption is almost zero for channel heights lower than 400μm. Desorption and adsorption of hydroxyl ions (OH) are not modeled in this study since their concentration is so low that they do not affect the flow properties considering the fact that gas reactions are neglected.

Figure 4.2 shows variations of surface coverage of the species along the channel predicted by the two methods. Overall, the surface coverage of O and Pt are in excellent agreement. Surface coverage is defined as the fraction of total number of catalytic sites occupied by the corresponding species. The surface coverage of H has the highest deviation of about 10% at the inlet but shows good agreement for the rest of the channel. This results in an underestimation for OH which is very sensitive to reactant concentrations. Surface coverage of water is also affected by lower H coverage but is in very good agreement. The reason for this behaviour is higher non-equilibrium effects for H due to its low concentration in gas (around 8×10^{-3} by mass) and light molecule. These effects are especially intensified close to the inlet due to the rapid development of the flow and higher molecular adsorption on the surface. These conditions will lead to some error in MCR calculated by Navier-Stokes equations which is basically derived from equilibrium distributions. As it was mentioned

Table 4.1: Surface reaction mechanism for hydrogen oxidation on platinum [58]. Surface species are denoted by a superscript "*".

	Reaction	A[a][mol,cm,sec]	γ[b]	E_a [kJ/mol]
1	$H_2 + 2Pt^* \rightarrow 2H^*$	-	0.046[c]	-
2	$O_2 + 2Pt^* \rightarrow 2O^*$	-	0.07[d]	-
3	$H_2O + Pt^* \rightarrow H_2O^*$	-	0.75	-
4	$H^* + O^* \rightarrow OH^* + Pt^*$	3.7×10^{21}	-	11.5
5	$OH^*+Pt^* \rightarrow H^* + O^*$	3.7×10^{21}	-	24.5
6	$H^* + OH^* \rightarrow H_2O^* + Pt^*$	3.7×10^{21}	-	17.5
7	$H_2O^* + Pt^* \rightarrow H^* + OH^*$	3.7×10^{21}	-	113.5
8	$OH^* + OH^* \rightarrow H_2O^* + O^*$	3.7×10^{21}	-	48.2
9	$H_2O^* + O^* \rightarrow OH^* + OH^*$	3.7×10^{21}	-	131.4
10	$2H^* \rightarrow H_2 + 2Pt^*$	3.7×10^{21}	-	$67.4\text{-}6\theta_{H^*}$
11	$2O^* \rightarrow O_2 + 2Pt^*$	3.7×10^{21}	-	$213.2\text{-}60\theta_{O^*}$
12	$H_2O^* \rightarrow H_2O + Pt^*$	1.0×10^{13}	-	40.3

[a] A and E_a are Arrhenius parameters for calculating rate constant from $k = A\exp(-E_a/RT)$

[b] γ is the sticking factor coefficient

[c] Hydrogen adsorption is first order in terms of Pt^*

[d] Oxygen sticking factor varies with temperature as γ_{O_2}=0.07(T_0/T) where T_0=300K.

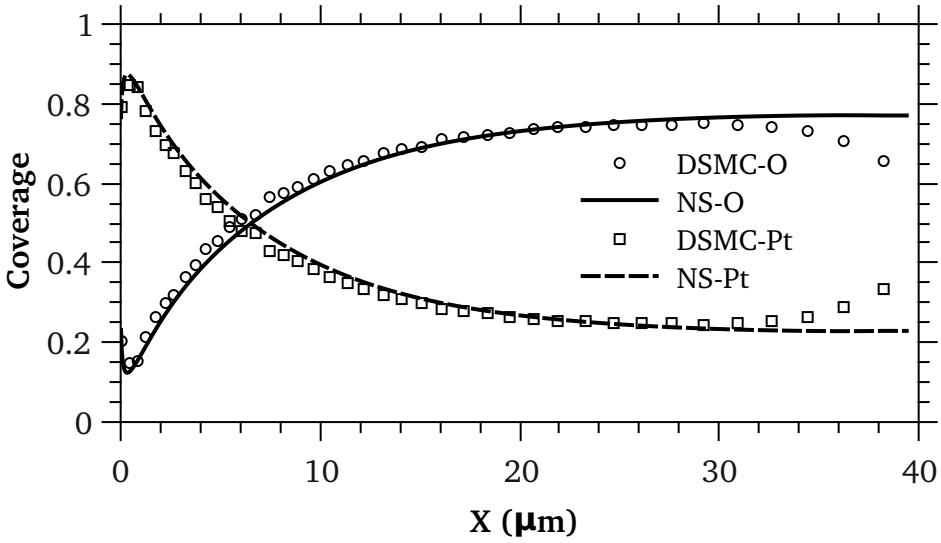

(a)

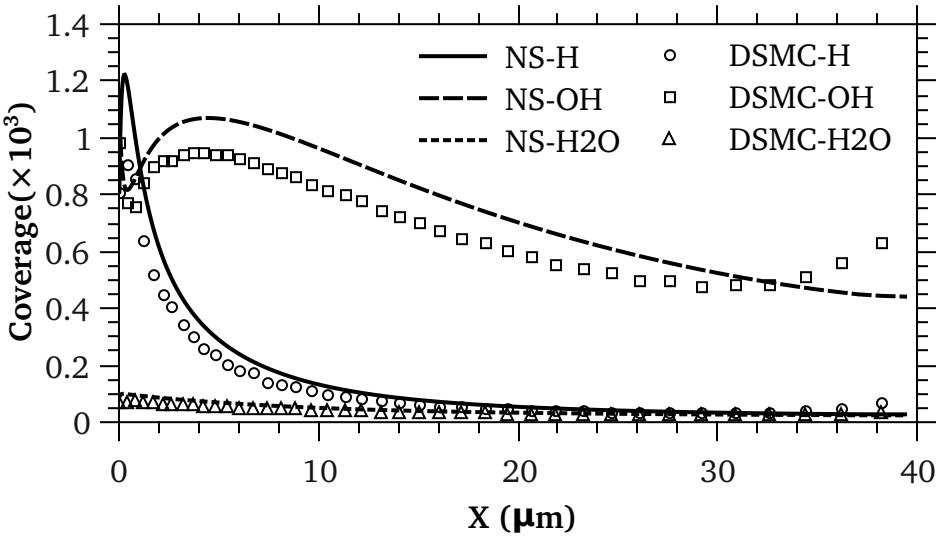

(b)

Figure 4.2: Variations of surface coverage of surface species; (a) Oxygen "O" and platinum "Pt", (b) Hydrogen "H", Hydroxyl "OH", and Water "H_2O"

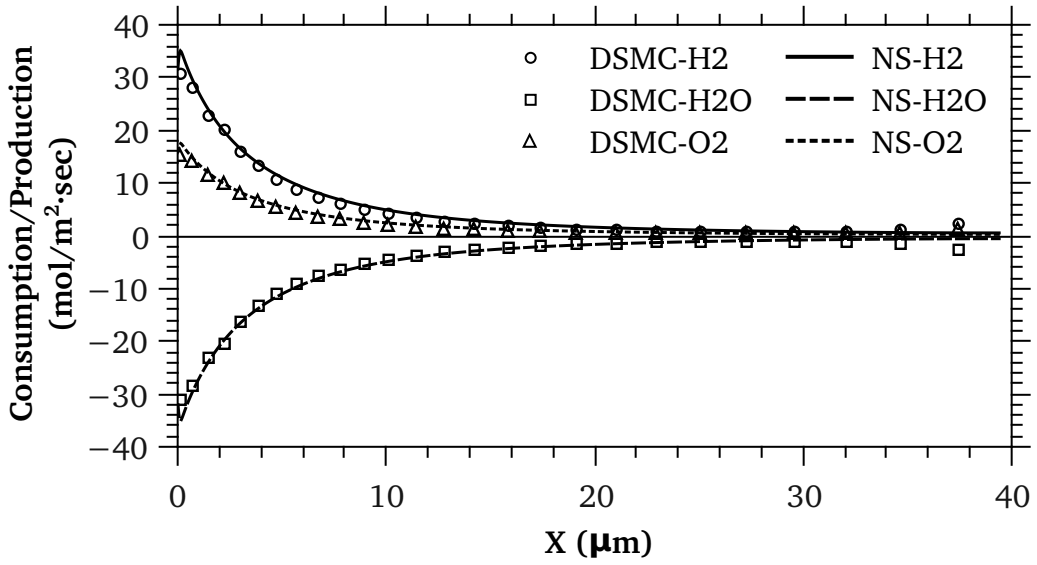

Figure 4.3: Consumption/Production rate of gas species on the catalytic surface. Positive and negative values denote consumption and production respectively.

earlier MCR couples the gas flow and reactions on the surface and therefore, can directly influence surface coverage values. Another observation from this figure is that H is almost fully consumed up to the middle of the channel; especially, within the first quarter. This shows that the majority of the surface reaction takes place at the first quarter of the channel.

Figure 4.3 shows the molar consumption and production of gas species per unit area and time. Generally, a very good agreement is achieved and as it was expected a maximum of 10% deviation occurs near the entrance due to non-equilibrium effects explained before. The magnitude of O_2 consumption at each section is half of H_2 and H_2O and this complies with the main reaction H_2+1/2 $O_2 \rightarrow H_2O$.

Verification of slip velocity results are represented in Figure 4.4a. Both methods predict the same value at the inlet and a good agreement is seen after the first 10% of the channel where the slip velocity continuously increases through out the channel. Within the first 10% of the channel results of the methods deviate from each other; DSMC shows a sudden

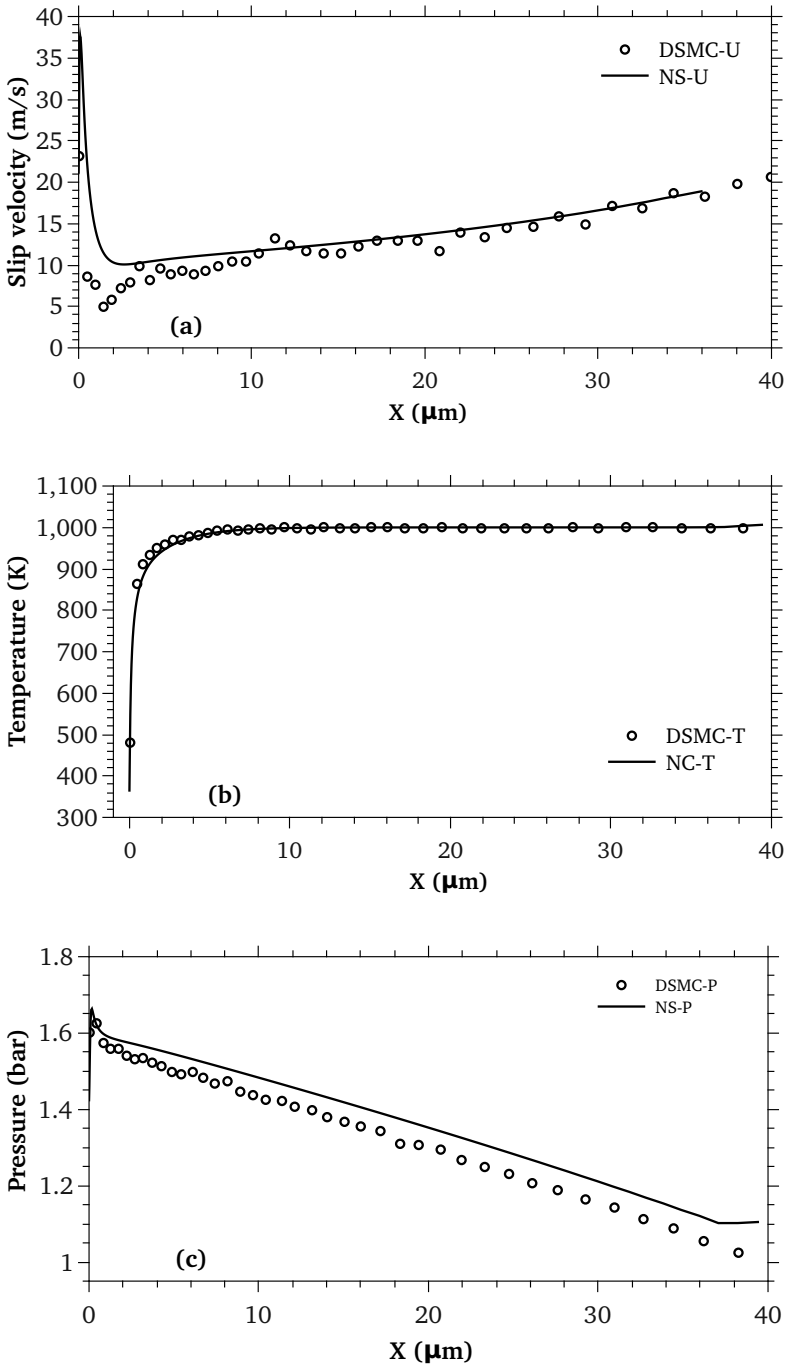

Figure 4.4: Variations of the slip velocity, gas temperature next to the wall and pressure at midplane of the channel.

decrease right after the inlet whereas Navier-Stokes shows a rapid increase followed by a sharp decrease. This behaviour is caused by the rapid development of the flow in the entrance region and its quality is related to the nature of the simulating method. Due to constant mass flux at the inlet, the slip velocity is expected to have a sharp drop next to the entrance before its continuous increase. This is close to DSMC simulations; however, as explained in [22] molecular interactions with the wall in DSMC will lead to a bit overestimation of the slip velocity drop. On the other hand, the velocity spike seen in Navier-Stokes results is caused by sudden increase in temperature at the wall making a singularity point for the differential equations. Therefore such behaviours are caused by numerical limitations of the methods and are not as a discrepancy in verifications. Gas temperature next to the wall shown in Figure 4.4b and the pressure at the midplane of the channel shown in Figure 4.4c are generally in very good agreement.

Figures 4.5a and 4.5b show the distribution of molar concentration of gas species along the channel. An excellent agreement is seen for all species. Due to lower consumption of H_2 shown in Figure 4.3 within the entrance region calculated by DSMC, molar concentration of this species in this region is slightly higher than Navier-stokes results. As a result DSMC predicts lower water production close to the inlet and in turn its molar concentration of water is slightly less than Navier-Stokes results.

Profiles of molar concentration of gas species along Y axis at different cross sections of the channel shown in Figure 4.5 also demonstrate a very good agreement. Effect of surface reaction on the gas concentration field is obviously seen at the inlet (Figure 4.6a) and gets weaker along the channel. DSMC data show higher H_2 concentration at the inlet because of its lower consumption as explained before.

4.4 Results and discussion

Effects of channel height, inlet and wall temperatures, and equivalence ratio on chemical reaction and flow properties are presented in this section. The same arrangement shown in Figure 1.1 is used in this section. The length of the perforated plate is considered to be constant for all cases and is equal to 10μm. The cases considered in this study is listed in

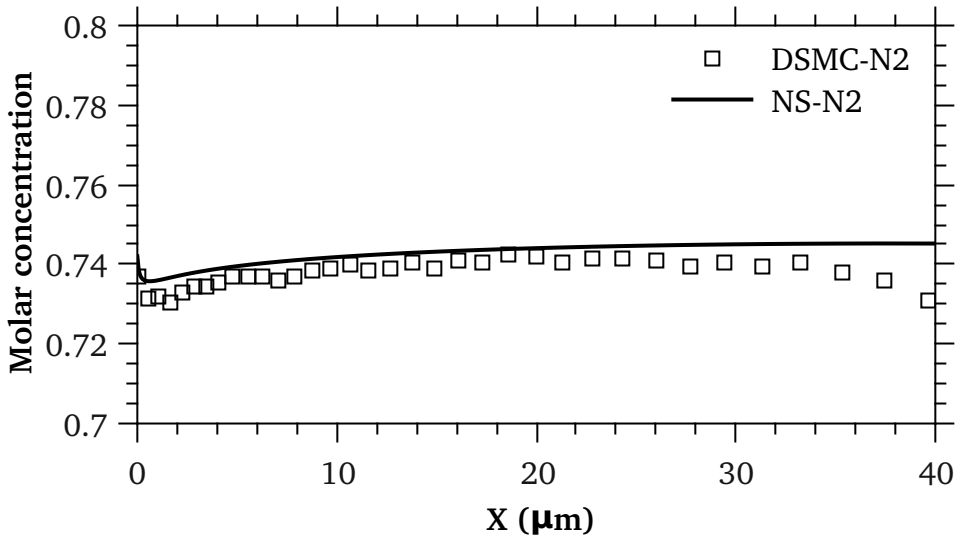

(a)

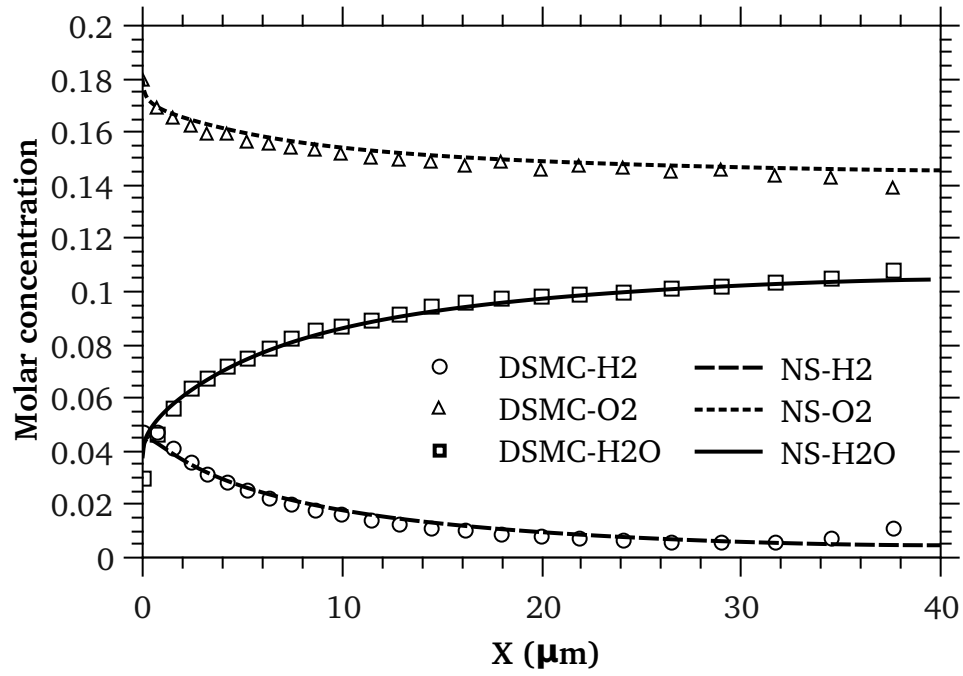

(b)

Figure 4.5: Variations of molar concentration of gas species; (a) N_2, (b) H_2, O_2, and H_2O

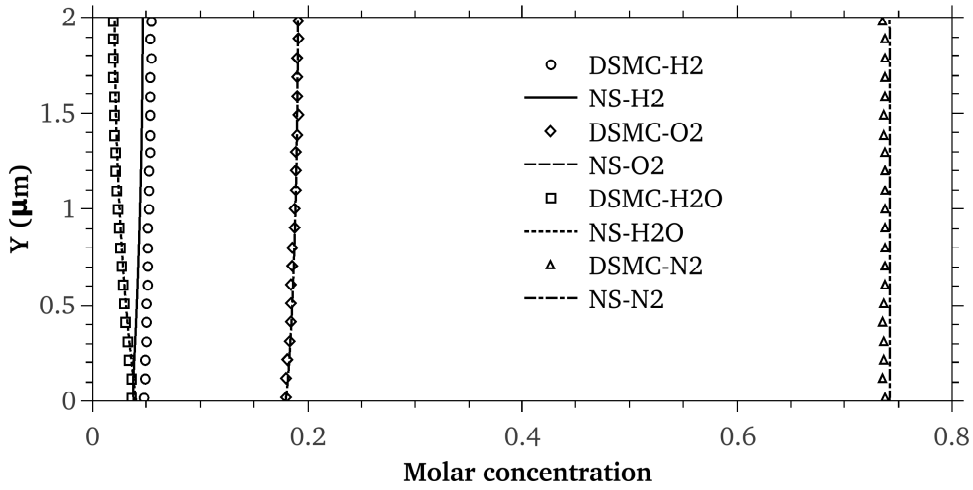

(a) Section at inlet

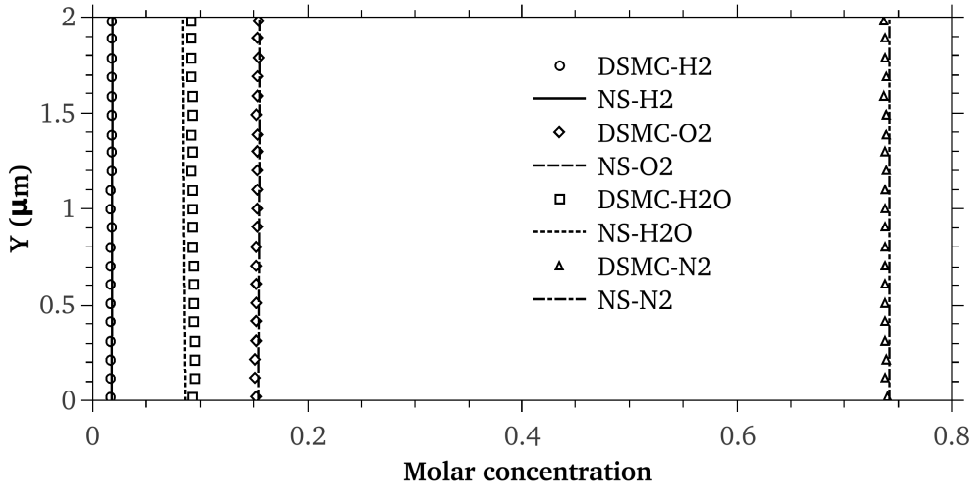

(b) Section at 25% of the channel length

Figure 4.6: Sectional verification of gas species mole fractions

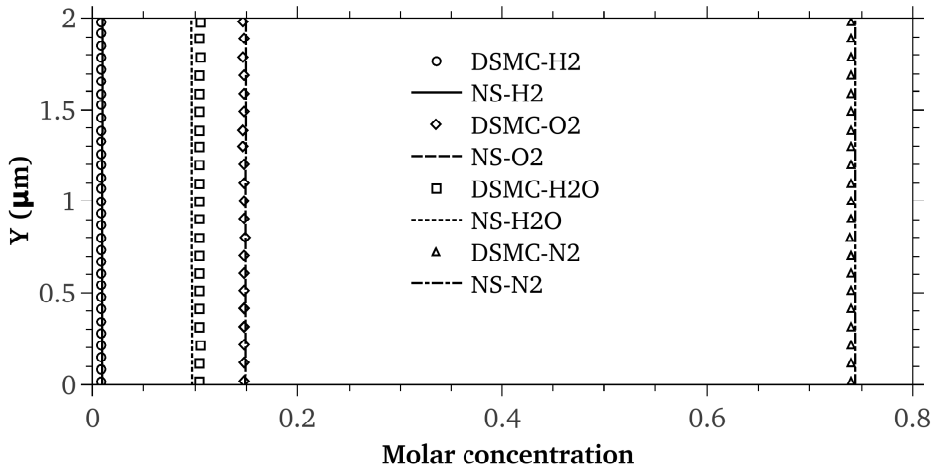

(c) Section at 50% of the channel length

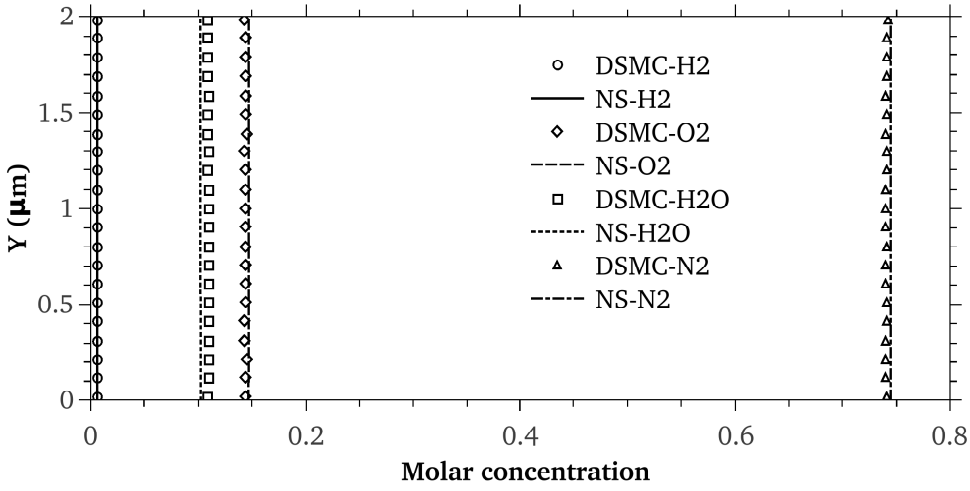

(d) Section at 75% of the channel length

Figure 4.5: Sectional verification of gas species mole fractions (continued)

Table 4.2. An atmospheric pressure is set at the outlet for all cases. The first 1μm of the channel is considered as non catalytic length avoiding entrance region effects on chemical reactions. The number of cells is assigned based on values of the mean free path at the inlet and the outlet, so that a cell face is not larger than one half of the local mean free path through out the channel. The initial number of forty simulating particles per cell is considered.

4.4.1 Effect of channel height

As shown in Table 4.2 the only variable in Cases 1-4 is the channel hight and the rest of the parameters are kept constant. The Kn range covered by these cases simulates initial part of the transition regime which is more likely to occur in practice. To ensure the accuracy of the boundary conditions imposed, variations of the mass flux and the equivalence ratio at the inlet section are shown in Figure 4.6. As seen in Figure 4.6a, total mass flux of the fuel/air is effectively maintained at the imposed value of 25 kg/m^2·s for all cases. In addition, mass flux of water is kept at zero using the method explained before. Figure 4.8b shows mass concentrations of fuel/air species at the inlet. These values are sampled based on the fuel/air particles regardless of the local amount of water. This is in conformance with the definition of the equivalence ratio. Solid lines represent the values calculated from the imposed equivalence ratio of ϕ=0.28. As seen, mass concentrations are efficiently controlled at specified values.

Distributions of the flow properties for Cases 1-4 are shown in Figure 4.7. As seen in Figure 4.7b, the outlet pressure is maintained well at the atmospheric value. In all Cases, the pressure decreases following a small increase right after the entrance. This small pressure rise is caused by the rapid gas heating due to the high inlet gas and wall temperature difference (see Figure 4.7d). Another observation is the higher inlet pressure for lower Kn cases due to constant mass flux applied at the inlet. As a result, the gas density has a greater value and therefore, slip velocity has a lower value at the inlet at higher Kn (see Figure 4.7c). This also leads to a higher heat conduction coefficient and consequently, as shown in Figure 4.7d, the temperature rises to wall temperature more rapidly at higher Kn.

Table 4.2: Surface reaction mechanism for hydrogen oxidation on platinum [58]. Surface species are denoted by a superscript "*".

Case	T_w [K]	T_{in} [K]	H [μm]	p_{in} [bar]	Kn_{in}	Kn_{out}	Re_{in}	Ma_{out}	ϕ	$\dot{m}''$ [kg/m^2·s]
C1	1000	300	2.0	1.12	0.025	0.095	3.6	0.19	0.28	25
C2	1000	300	1.0	1.29	0.044	0.19	1.8	0.19	0.28	25
C3	1000	300	0.75	1.4	0.054	0.25	1.3	0.19	0.28	25
C4	1000	300	0.5	1.56	0.072	0.375	0.9	0.19	0.28	25
C5	1000	300	0.5	1.56	0.072	0.375	0.9	0.19	0.35	25
C6	1000	300	0.5	1.56	0.072	0.375	0.9	0.19	0.5	25
C7	1000	300	0.5	1.56	0.072	0.375	0.9	0.19	1.0	25
C8	1000	300	0.5	1.56	0.072	0.375	0.9	0.19	1.5	25
C9	1000	500	0.5	1.85	0.101	0.375	0.7	0.15	0.28	25
C10	1000	700	0.5	2.13	0.123	0.375	0.6	0.12	0.28	25
C11	600	300	0.5	1.66	0.068	0.225	0.9	0.12	0.28	25
C12	700	300	0.5	1.64	0.069	0.262	0.9	0.14	0.28	25
C13	800	300	0.5	1.61	0.07	0.3	0.9	0.15	0.28	25
C14	300	300	0.5	1.7	0.066	0.112	0.9	0.06	0.28	25
C15	1000	300	0.5	1.33	0.072	0.375	0.5	0.12	0.28	15
C16	1000	300	0.5	1.11	0.072	0.375	0.2	0.04	0.28	5
C17	400	300	0.5	1.7	0.066	0.15	0.9	0.08	1.0	25
C18	600	300	0.5	1.66	0.068	0.225	0.9	0.12	1.0	25
C19	800	300	0.5	1.61	0.07	0.3	0.9	0.15	1.0	25
C20	400	300	0.5	1.7	0.07	0.15	0.9	0.08	1.5	25
C21	600	300	0.5	1.66	0.07	0.225	0.9	0.12	1.5	25
C22	800	300	0.5	1.61	0.07	0.3	0.9	0.15	1.5	25
C23	1000	300	1.0	1.29	0.04	0.187	1.8	0.19	1.0	25
C24	1000	300	2.0	1.12	0.025	0.095	3.6	0.19	1.0	25
C25	1000	300	1.0	1.29	0.04	0.187	1.8	0.19	1.5	25
C26	1000	300	2.0	1.12	0.025	0.095	3.6	0.19	1.5	25

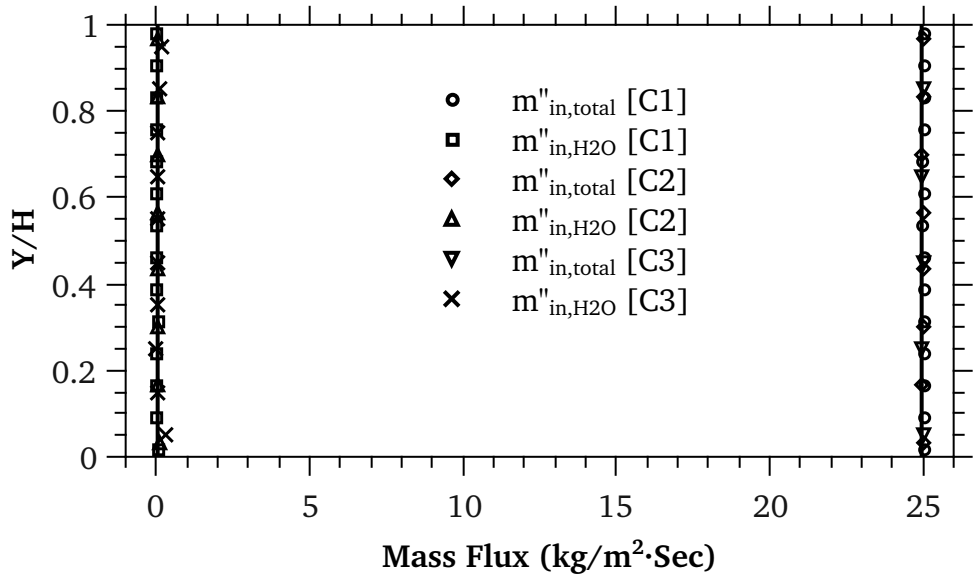

(a)

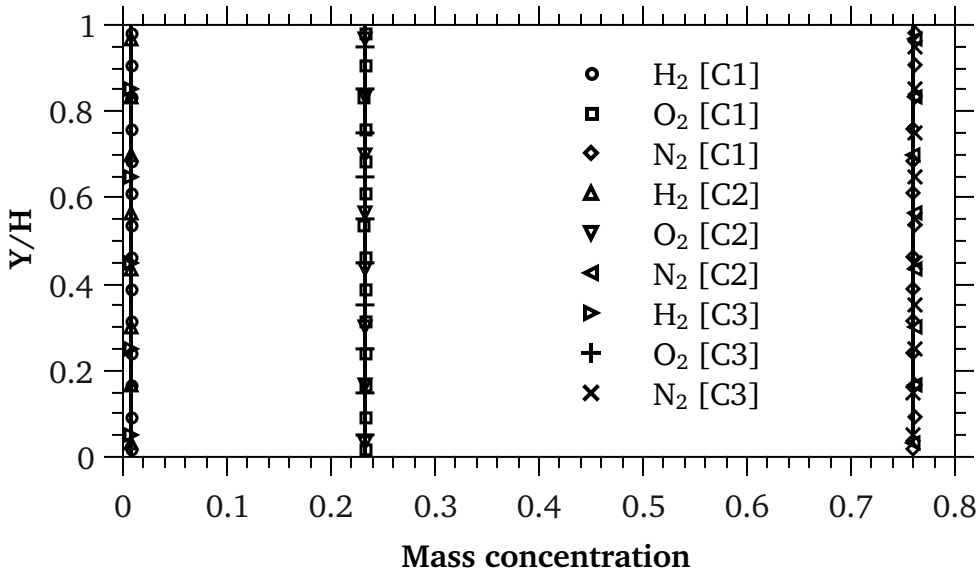

(b)

Figure 4.6: (a) Mass flux of fuel/air and water at the inlet of the channel. (b) Mass concentration of fuel/air species at the inlet of the channel. Solid lines represent mass concentrations calculated from the specified equivalence ratio

	T_w	T_{in}	H	p_{in}	Kn_{in}	Kn_{out}	Re_{in}	Ma_{out}	ϕ	$\dot{m}''$
C5	1000	300	0.5	1.56	0.072	0.375	0.9	0.19	0.35	25
C6	1000	300	0.5	1.56	0.072	0.375	0.9	0.19	0.5	25
C7	1000	300	0.5	1.56	0.072	0.375	0.9	0.19	1.0	25

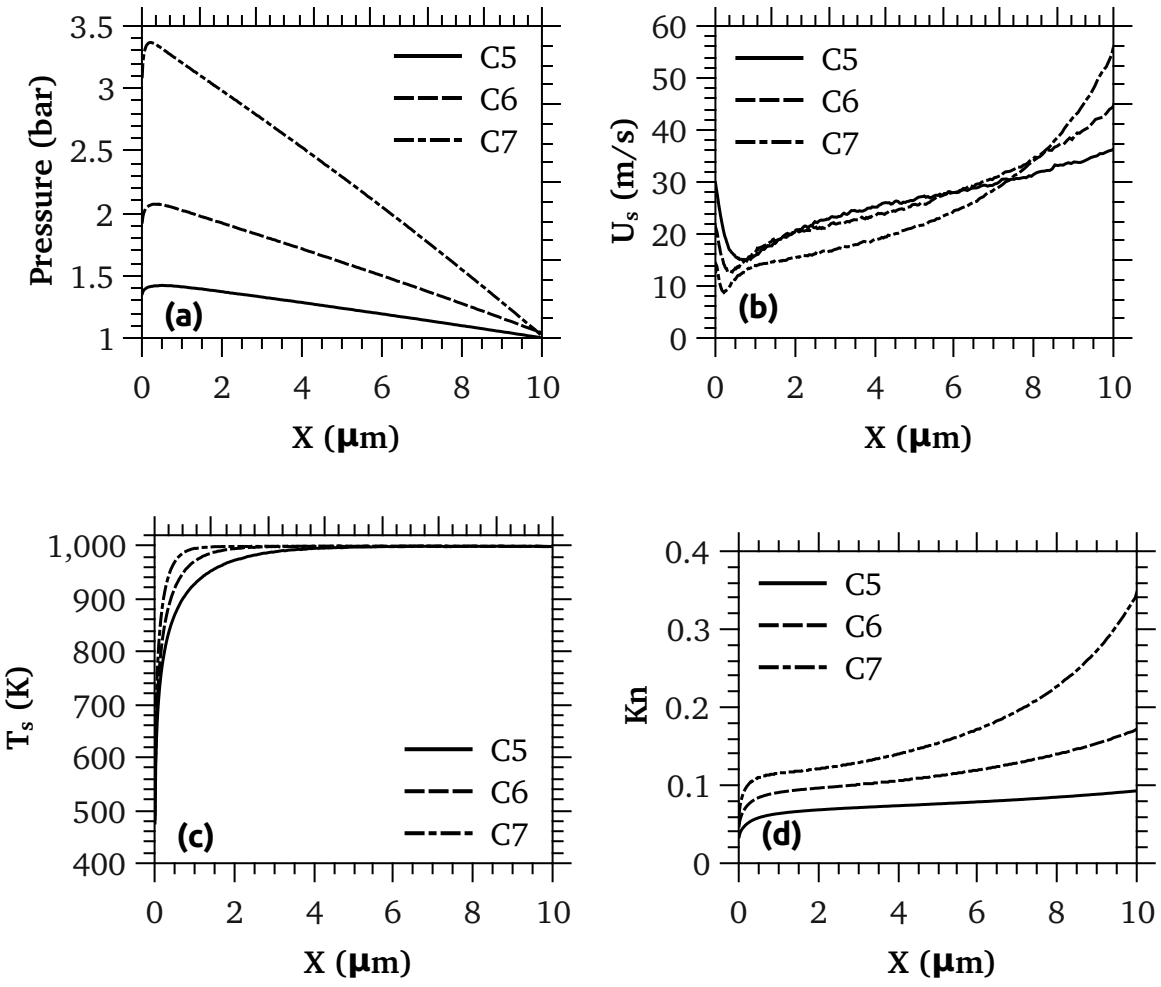

Figure 4.7: Effects of geometry on flow properties; Cases 5-7

Figures 4.8-4.13 show effects of various geometries on surface coverage of the species participating in heterogeneous reactions. Due to the close relation, surface coverage graphs of each species are followed by molar concentration graphs of the corresponding component in the gas. As it was mentioned earlier, catalytic reactions start at 1μm and therefore, the surface coverage of hydrogen θ_{H^*} steps up at this point, seen in Figure 4.8. The starting value of θ_{H^*} is not affected by the geometry and is a function of flow and surface properties. Generally, θ_{H^*} decreases from this constant value for all channel heights and gets close to zero at some distance. Due to the fact that all cases studied in this part are fuel lean ($\phi = 0.28$), the point at which θ_{H^*} approaches zero falls within the channel. At this point, the hydrogen concentration in the gas X_{H_2} is low enough so that the hydrogen adsorption rate is almost equal to the rate of hydrogen consumption on the surface. Thus, from this point on, small amount of adsorbed hydrogen molecules will be left on the surface at steady state conditions. This also reduces reaction rates for the rest of the channel and lack of θ_{H^*} becomes the limiting factor of surface reactions. Distributions of X_{H_2} in Figure 4.8 also turn into a constant value from where θ_{H^*} attains zero. Another notable point in this figure is that X_{H_2} has different values at the inlet for different channel heights despite the fact that equivalence ratio is constant. The reason is that molar density of water is also considered in evaluation of X_{H_2} where as equivalence ratio is calculated just from molar densities of reactants species.

While θ_{H^*} is diminishing along the channel, adsorbed oxygen molecules are consumed less and hence, θ_{O^*} sharply increases as shown in Figure 4.9. Both θ_{H^*} and X_{O_2} become constant from this point on, as expected. $\theta_{H_2O^*}$ increases up to this point due to high reaction rates and decreases afterwards, and X_{H_2O} becomes constant. The noticeable point here is that $\theta_{H_2O^*}$ for smaller channels is higher or almost equal to that of larger channels for the entire length of the channel. This guarantees higher X_{H_2O} throughout the channel due to higher desorption rate, confirmed by Figure 4.10. This can be explained by noting that higher pressure values at lower channel sizes cause higher MCR (mass diffusion to the surface). This leads to a higher adsorption rate for H_2 and O_2 and therefore, the conversion rate will be higher. For example, the conversion rate of H_2 is shown in Figure 4.11. It is observed that H_2 conversion rate is higher for smaller channels as expected; thus, higher production rate of H_2O results in greater values for $\theta_{H_2O^*}$, and X_{H_2O}. However, the

conversion rate dramatically diminishes at the point where θ_{H^*} goes to zero. This point occurs earlier for smaller channels as the higher conversion rate of these cases quickly consumes available H_2 molecules adsorbed on the surface (see Figure 4.8). Moreover, gas flow entering small channel sizes carries less amount of reactant molecules due to constant mass flux and equivalence ratio. This together with the fact that available surface sites is constant for all cases, result in even more reduction of the effective conversion length and lowers concentrations of the reactants as observed in Figures 4.8 and 4.9. As an additional result, greater portion of air/H_2 molecules will be converted to water and therefore, the water concentration for smaller channels is higher (see Figure 4.10). This directly points out that the efficiency of the reactor arrangement of Figure 1.1 with smaller perforations will be higher. Molar flow rate of H_2 shown in Figure 4.12 clearly reveals that as the channel height decreases the portion of H_2 consumed in the reactions is higher. If the efficiency for the reactor is defined as the ratio of H_2 moles participating in the reactions to the total amount of H_2 entering the channel, this value varies from 82% for Case 1 to 99% for Case 4.

Figure 4.13 shows distributions of θ_{OH^*} for different geometries. Due to the low coverage of OH^*, desorption of OH ions to the gas flow is negligibly small. Moreover, gas reactions are not simulated here as mentioned before and therefore, modelling OH desorption seems pointless.

4.4.2 Effect of equivalence ratio

So far all Cases studied above were fuel lean ($\phi < 1$). In this section effect of the higher equivalence ratio, stoichiometric, and fuel rich conditions are investigated. By increasing ϕ, a higher amount of H_2 molecules is carried into the channel with the flow; therefore, the effective reaction length (along which θ_{H^*} is greater than zero) is extended. As shown in Figure 4.14, for ϕ around 0.5 and higher, θ_{H^*} has non zero values throughout the channel. It is also observed that X_{H_2} is higher than zero at $\phi \geq 0.5$ for the entire channel length. The effect of higher values of ϕ on θ_{O^*} is shown in Figure 4.15. As expected, θ_{O^*} for Cases 4 and 5 rises rapidly right after θ_{H^*} diminishes on the surface. However, for the rest of the Cases, θ_{O^*} is less than 10^{-5}. This reveals that the limiting factor for the reactions

	T_w [K]	T_{in} [K]	H [μm]	p_{in} [bar]	Kn_{in}	Kn_{out}	Re_{in}	Ma_{out}	ϕ	$\dot{m}''$ [kg/m^2·s]
C1	1000	300	2.0	1.12	0.025	0.095	3.6	0.19	0.28	25
C2	1000	300	1.0	1.29	0.044	0.19	1.8	0.19	0.28	25
C3	1000	300	0.75	1.4	0.054	0.25	1.3	0.19	0.28	25
C4	1000	300	0.5	1.56	0.072	0.375	0.9	0.19	0.28	25

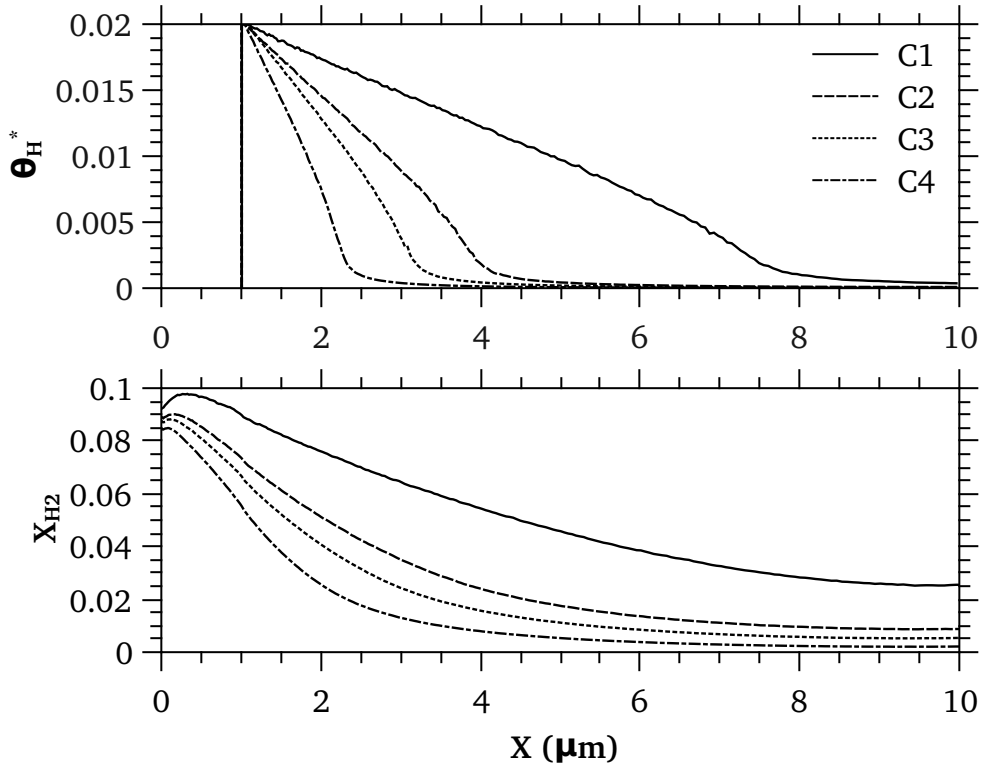

Figure 4.8: Effects of geometry on θ_{H^*} and X_{H_2}; Cases 1-4

	T_w [K]	T_{in} [K]	H [μm]	p_{in} [bar]	Kn_{in}	Kn_{out}	Re_{in}	Ma_{out}	ϕ	$\dot{m}''$ [kg/m^2·s]
C1	1000	300	2.0	1.12	0.025	0.095	3.6	0.19	0.28	25
C2	1000	300	1.0	1.29	0.044	0.19	1.8	0.19	0.28	25
C3	1000	300	0.75	1.4	0.054	0.25	1.3	0.19	0.28	25
C4	1000	300	0.5	1.56	0.072	0.375	0.9	0.19	0.28	25

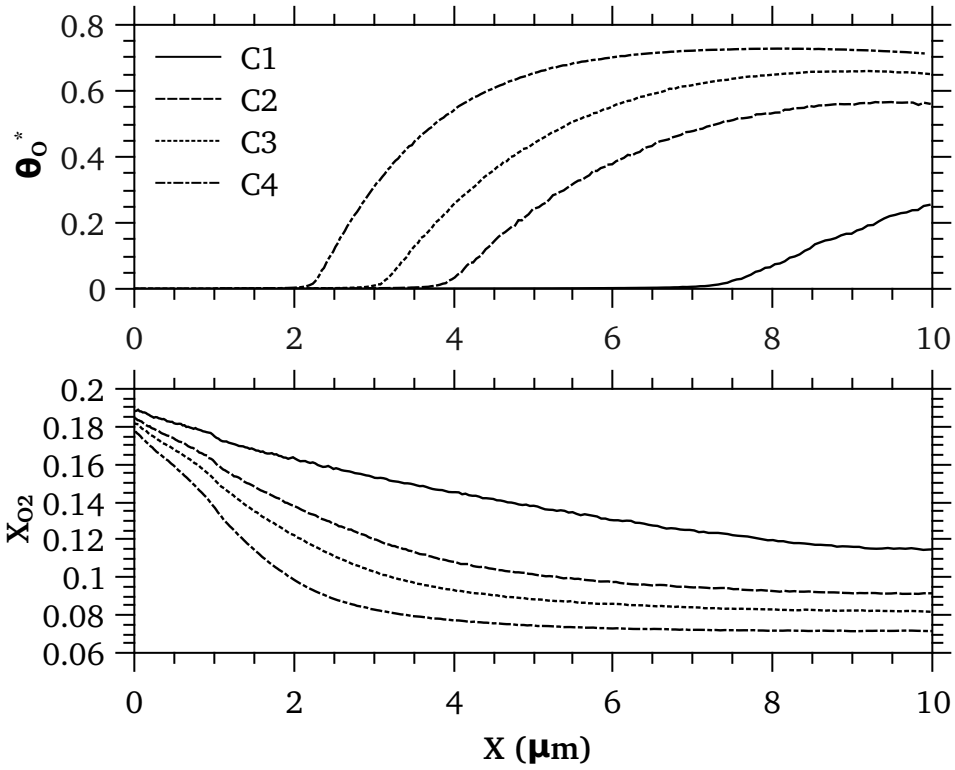

Figure 4.9: Effects of geometry on θ_{O^*} and X_{O_2}; Cases 1-4

	T_w [K]	T_{in} [K]	H [μm]	p_{in} [bar]	Kn_{in}	Kn_{out}	Re_{in}	Ma_{out}	ϕ	$\dot{m}''$ [kg/m^2·s]
C1	1000	300	2.0	1.12	0.025	0.095	3.6	0.19	0.28	25
C2	1000	300	1.0	1.29	0.044	0.19	1.8	0.19	0.28	25
C3	1000	300	0.75	1.4	0.054	0.25	1.3	0.19	0.28	25
C4	1000	300	0.5	1.56	0.072	0.375	0.9	0.19	0.28	25

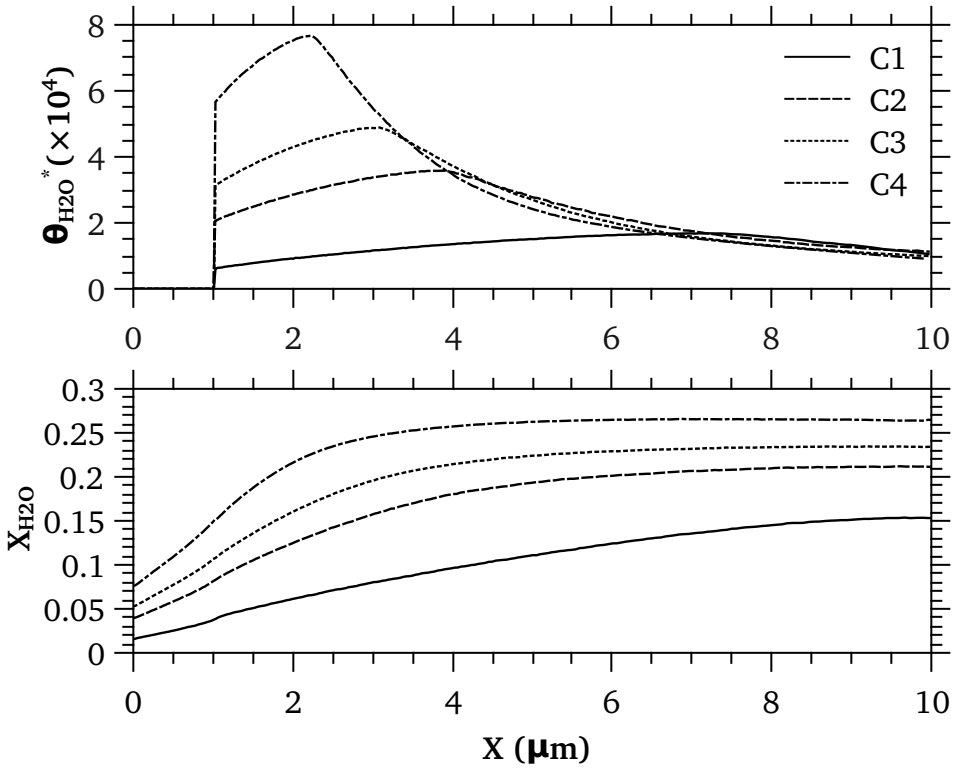

Figure 4.10: Effects of geometry on $\theta_{H_2O^*}$ and X_{H_2O}; Cases 1-4

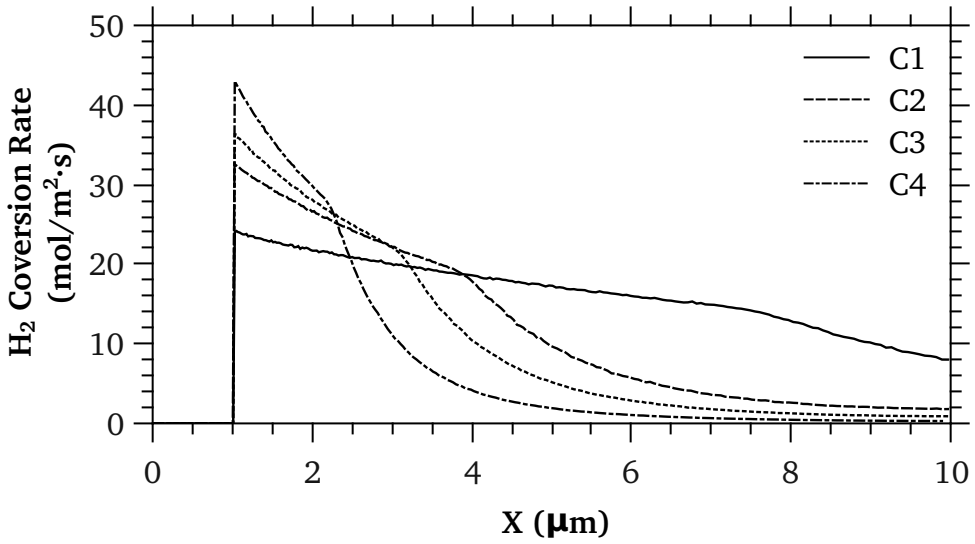

Figure 4.11: Effect of geometry on conversion rate of H_2; Cases 1-4

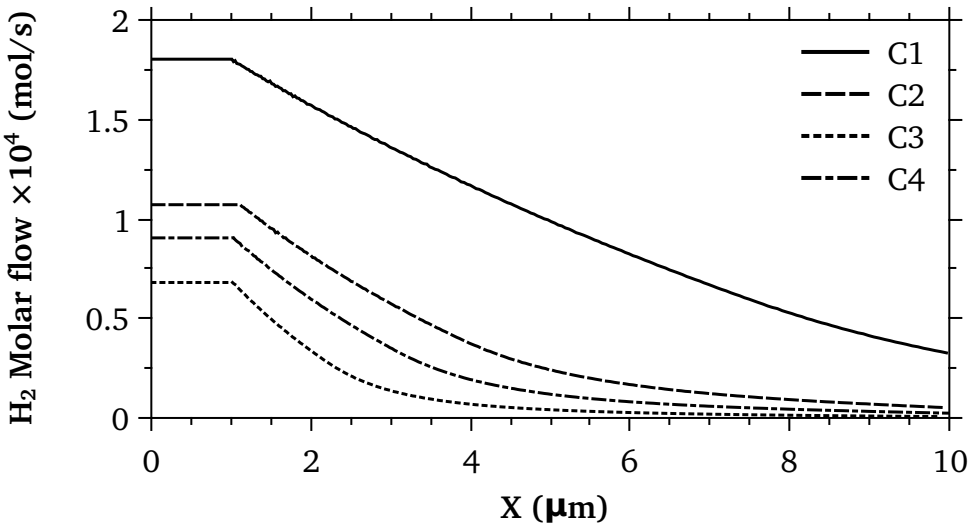

Figure 4.12: Effect of geometry on molar flow rate of H_2 through the channel; Cases 1-4

	T_w [K]	T_{in} [K]	H [μm]	p_{in} [bar]	Kn_{in}	Kn_{out}	Re_{in}	Ma_{out}	ϕ	$\dot{m}''$ [kg/m^2·s]
C1	1000	300	2.0	1.12	0.025	0.095	3.6	0.19	0.28	25
C2	1000	300	1.0	1.29	0.044	0.19	1.8	0.19	0.28	25
C3	1000	300	0.75	1.4	0.054	0.25	1.3	0.19	0.28	25
C4	1000	300	0.5	1.56	0.072	0.375	0.9	0.19	0.28	25

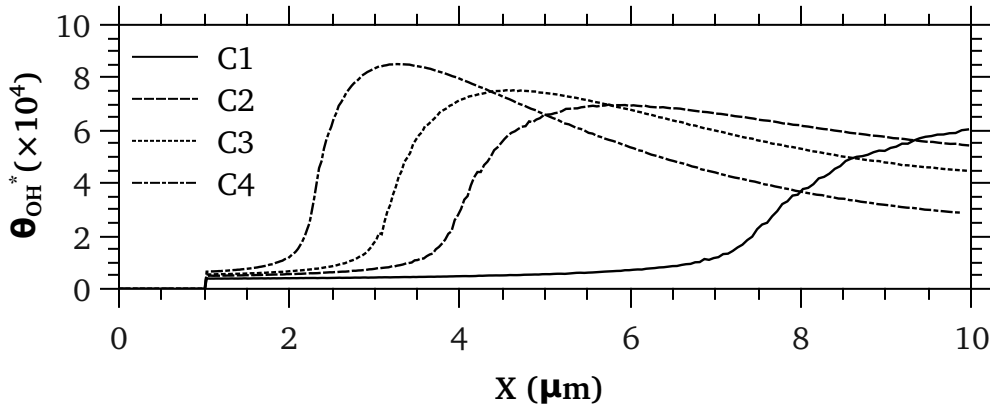

Figure 4.13: Effects of geometry on θ_{OH^*}; Cases 1-4

here is θ_{O^*} which itself is controlled by MCR of O_2 and θ_{Pt^*}. For fuel lean Cases, both of these controlling factors (MCR of O_2 and θ_{Pt^*}) are higher due to higher O_2 content of the gas flow and lower θ_{H^*}. Therefore, increasing fuel (H_2) content of the gas flow does not expectedly enhance reaction rates considerably. This is confirmed in Figure 4.14 as X_{H_2} is elevated by almost a constant amount with increasing ϕ. This shows that the conversion rate of H_2 has almost the same distribution for stoichiometric and fuel rich Cases.

Figure 4.16 shows that $\theta_{H_2O^*}$ is higher for Cases 4 and 5 (very fuel lean Cases) before they drop passing their effective reaction length. This proves the importance of the higher θ_{O^*} role for theses Cases. Another noticeable observation is that as ϕ increases from 0.5 for Case 6 to 1.0 and 1.5 for Cases 7 and 8 respectively, $\theta_{H_2O^*}$ decreases for the entire channel. This is also the result of the lower θ_{O^*} at higher values of ϕ. This behaviour causes X_{H_2O} at the channel outlet to have the greatest value for Case 6, an equal value for Cases 5 and 7, and almost an equal value for Cases 4 and 8. Efficiencies of these Cases are directly related to X_{H_2O} at the outlet and therefore, have the same distribution. As seen in Figure 4.16, X_{H_2O} for fuel lean Cases has higher initial values due to higher $\theta_{H_2O^*}$ and becomes constant after θ_{H^*} drops. On the other hand, X_{H_2O} for fuel rich Cases continuously increases along the channel but from a lower initial value. Overall, it can be concluded that there is a trade off between the amount of H_2 molecules available and the MCR of O_2, making an optimum value for ϕ which is about 0.5 for the current arrangement.

The cases studied so far had the same channel height of 500nm and as well all cases studied in Section 4.4.1 were on the fuel lean side (ϕ <1). To study mutual effects of geometry and ϕ, some cases with channel heights of 500nm, 1μm and 2μm at stoichiometric and fuel rich (ϕ=1.5) conditions are studied. As shown in Figure 4.18, decreasing the channel height amplifies the gradient of the θ_{H^*} distribution whereas increasing ϕ mostly elevates the θ_{H^*} distribution than changing its gradient. This pattern is also seen for θ_{O^*} in Figure 4.19. As discussed before, a steeper gradient of surface coverages means a higher surface reaction rate which itself augments the amount of products. Therefore, as clearly seen in Figure 4.20 decreasing the channel height has higher contribution on enhancing the product concentration and the conversion efficiency. Another observation is that the improvement made by increasing ϕ is higher for smaller channels due to higher surface to volume ratio.

	T_w [K]	T_{in} [K]	H [μm]	p_{in} [bar]	Kn_{in}	Kn_{out}	Re_{in}	Ma_{out}	ϕ	$\dot{m}''$ [kg/m^2·s]
C4	1000	300	0.5	1.56	0.072	0.375	0.9	0.19	0.28	25
C5	1000	300	0.5	1.56	0.072	0.375	0.9	0.19	0.35	25
C6	1000	300	0.5	1.56	0.072	0.375	0.9	0.19	0.5	25
C7	1000	300	0.5	1.56	0.072	0.375	0.9	0.19	1.0	25
C8	1000	300	0.5	1.56	0.072	0.375	0.9	0.19	1.5	25

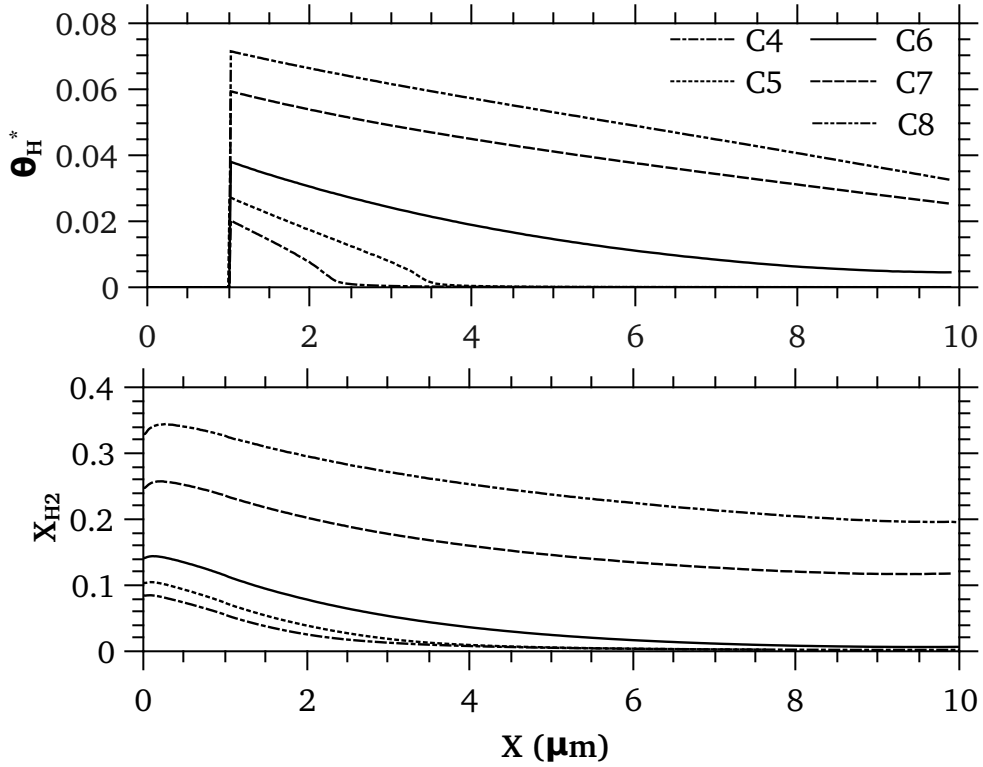

Figure 4.14: Effects of equivalence ratio on θ_{H^*} and X_{H_2}; Cases 4–8

	T_w [K]	T_{in} [K]	H [μm]	p_{in} [bar]	Kn_{in}	Kn_{out}	Re_{in}	Ma_{out}	ϕ	$\dot{m}''$ [kg/m^2·s]
C4	1000	300	0.5	1.56	0.072	0.375	0.9	0.19	0.28	25
C5	1000	300	0.5	1.56	0.072	0.375	0.9	0.19	0.35	25
C6	1000	300	0.5	1.56	0.072	0.375	0.9	0.19	0.5	25
C7	1000	300	0.5	1.56	0.072	0.375	0.9	0.19	1.0	25
C8	1000	300	0.5	1.56	0.072	0.375	0.9	0.19	1.5	25

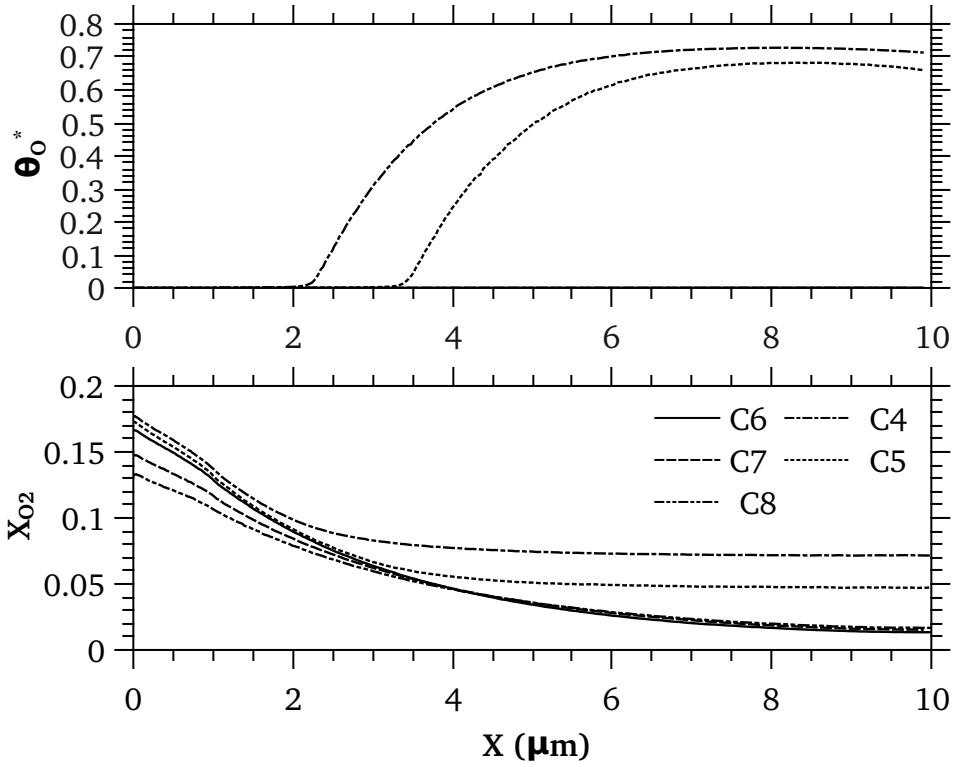

Figure 4.15: Effects of equivalence ratio on θ_{O^*} and X_{O_2}; Cases 4–8

	T_w [K]	T_{in} [K]	H [μm]	p_{in} [bar]	Kn_{in}	Kn_{out}	Re_{in}	Ma_{out}	ϕ	$\dot{m}''$ [kg/m^2·s]
C4	1000	300	0.5	1.56	0.072	0.375	0.9	0.19	0.28	25
C5	1000	300	0.5	1.56	0.072	0.375	0.9	0.19	0.35	25
C6	1000	300	0.5	1.56	0.072	0.375	0.9	0.19	0.5	25
C7	1000	300	0.5	1.56	0.072	0.375	0.9	0.19	1.0	25
C8	1000	300	0.5	1.56	0.072	0.375	0.9	0.19	1.5	25

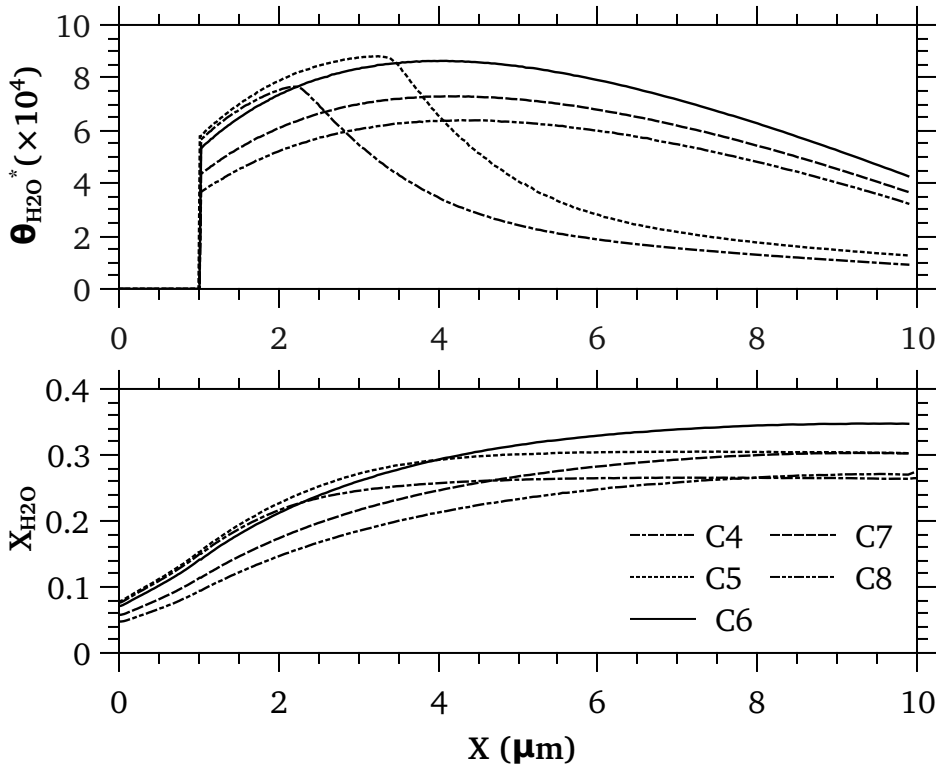

Figure 4.16: Effects of equivalence ratio on $\theta_{H_2O^*}$ and X_{H_2O}; Cases 4–8

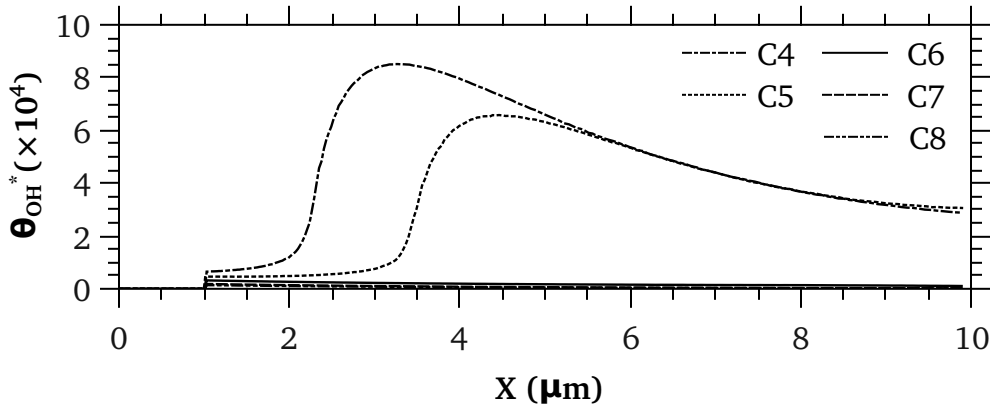

Figure 4.17: Effects of equivalence ratio on θ_{OH^*}; Cases 4–8

4.4.3 Effect of inlet temperature

Figure 4.21 demonstrates clearly that increasing inlet temperature from 300K (Case 4) to 700K (Case 10) has almost no effect on wall reactions and gas concentrations. The reason is that reactions on the surface is restrained by the molecular transfer from the gas to the surface and vice versa. Adsorption and desorption processes which create this molecular transfer are functions of the surface temperature and gas conditions adjacent to the wall. The only variable property here is the inlet temperature of the gas; however, as shown in Figure 4.7, the gas temperature next to the wall surface rises up to the wall temperature very quickly due to conductive nature of micro/nano flows. Hence, reactions on the surface has the same behaviour regardless of the inlet temperature. Practically, this is a favourable result; because, the gas contained in the inlet plenum of the hypothetical arrangement shown in Figure 1.1 will be affected by the high temperature of the perforated disk through conduction. Therefore, controlling the inlet temperature of the gas flow entering the channels is difficult if not impossible. The results of this section reveal that maintaining the temperature of the gas entering the perforated disk will not affect the performance of the reactions.

	T_w	T_{in}	H	p_{in}	Kn_{in}	Kn_{out}	Re_{in}	Ma_{out}	ϕ	$\dot{m}''$
C7	1000	300	0.5	1.56	0.072	0.375	0.9	0.19	1.0	25
C8	1000	300	0.5	1.56	0.072	0.375	0.9	0.19	1.5	25
C23	1000	300	1.0	1.29	0.04	0.187	1.8	0.19	1.0	25
C24	1000	300	2.0	1.12	0.025	0.095	3.6	0.19	1.0	25
C25	1000	300	1.0	1.29	0.04	0.187	1.8	0.19	1.5	25
C26	1000	300	2.0	1.12	0.025	0.095	3.6	0.19	1.5	25

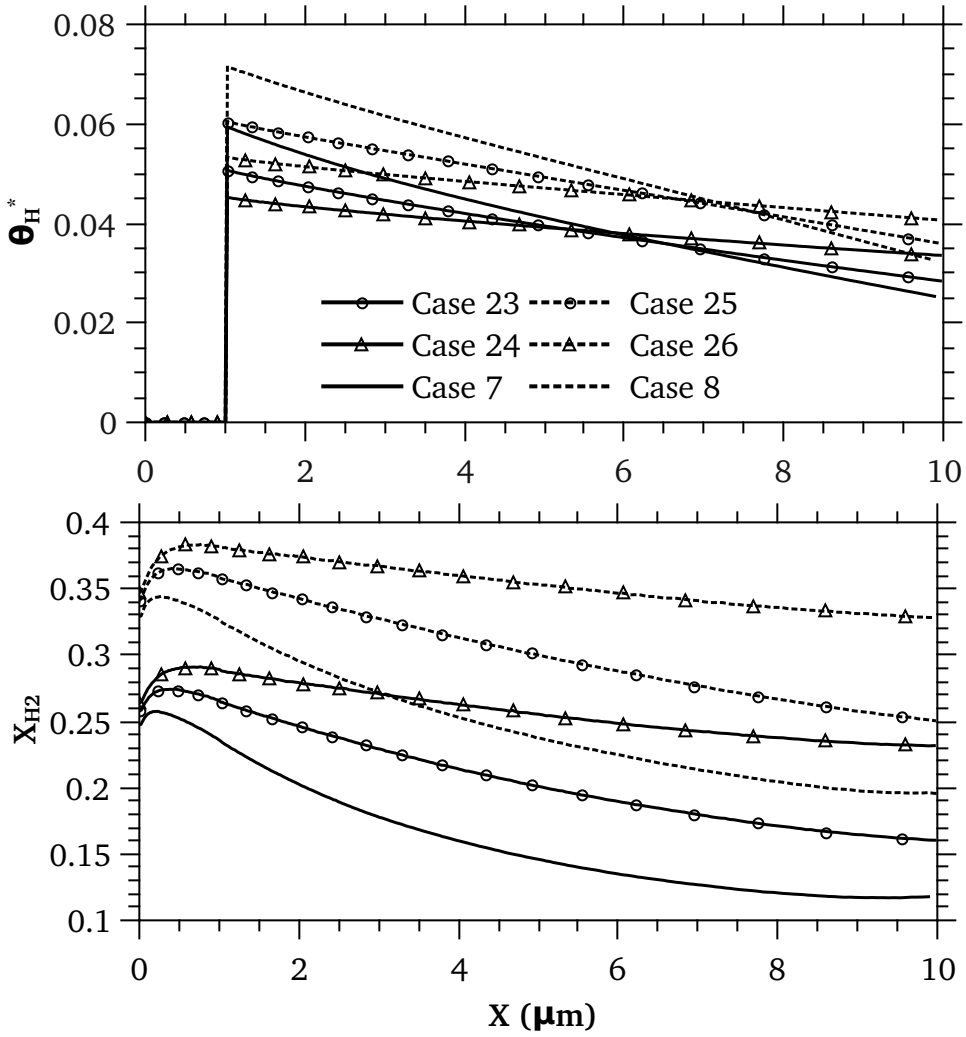

Figure 4.18: Effects of geometry on θ_{H^*} at stoichiometric and fuel rich conditions

	T_w	T_{in}	H	p_{in}	Kn_{in}	Kn_{out}	Re_{in}	Ma_{out}	ϕ	$\dot{m}''$
C7	1000	300	0.5	1.56	0.072	0.375	0.9	0.19	1.0	25
C8	1000	300	0.5	1.56	0.072	0.375	0.9	0.19	1.5	25
C23	1000	300	1.0	1.29	0.04	0.187	1.8	0.19	1.0	25
C24	1000	300	2.0	1.12	0.025	0.095	3.6	0.19	1.0	25
C25	1000	300	1.0	1.29	0.04	0.187	1.8	0.19	1.5	25
C26	1000	300	2.0	1.12	0.025	0.095	3.6	0.19	1.5	25

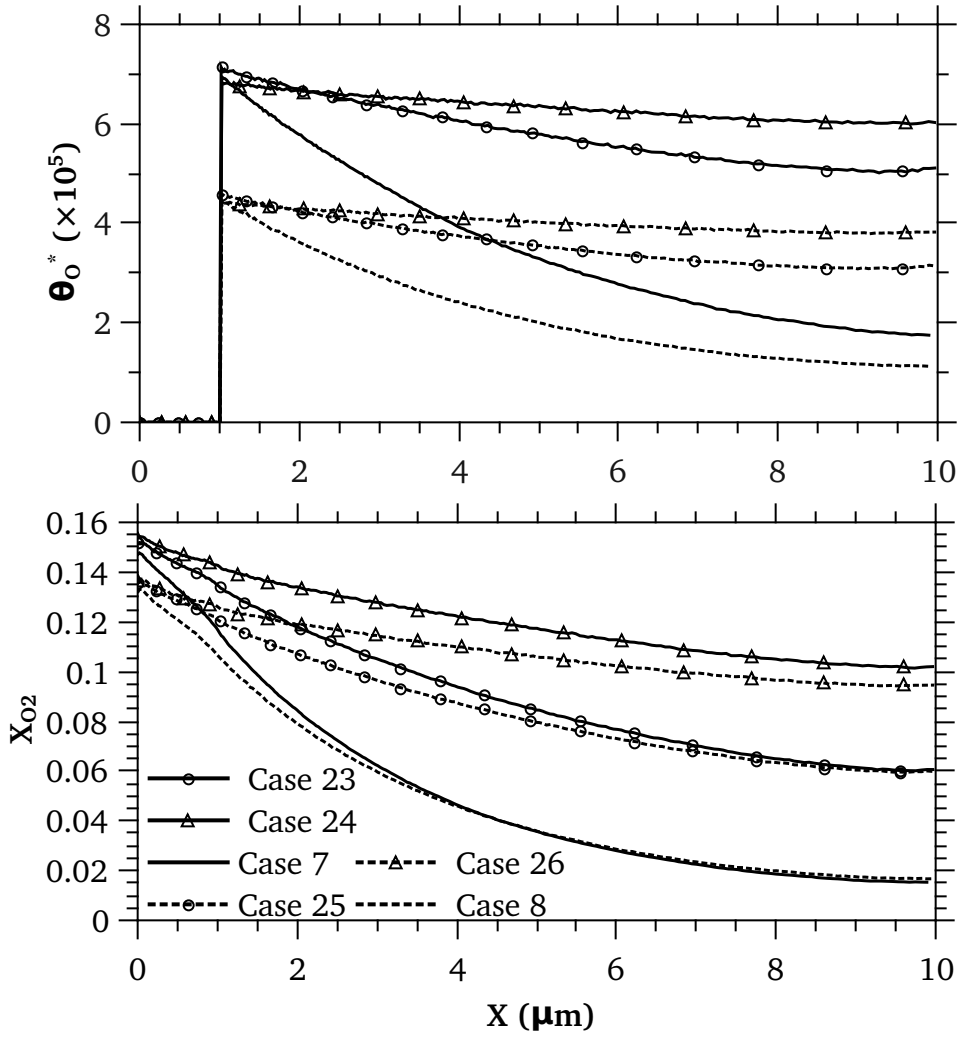

Figure 4.19: Effects of geometry on θ_{O^*} at stoichiometric and fuel rich conditions

	T_w	T_{in}	H	p_{in}	Kn_{in}	Kn_{out}	Re_{in}	Ma_{out}	ϕ	$\dot{m}''$
C7	1000	300	0.5	1.56	0.072	0.375	0.9	0.19	1.0	25
C8	1000	300	0.5	1.56	0.072	0.375	0.9	0.19	1.5	25
C23	1000	300	1.0	1.29	0.04	0.187	1.8	0.19	1.0	25
C24	1000	300	2.0	1.12	0.025	0.095	3.6	0.19	1.0	25
C25	1000	300	1.0	1.29	0.04	0.187	1.8	0.19	1.5	25
C26	1000	300	2.0	1.12	0.025	0.095	3.6	0.19	1.5	25

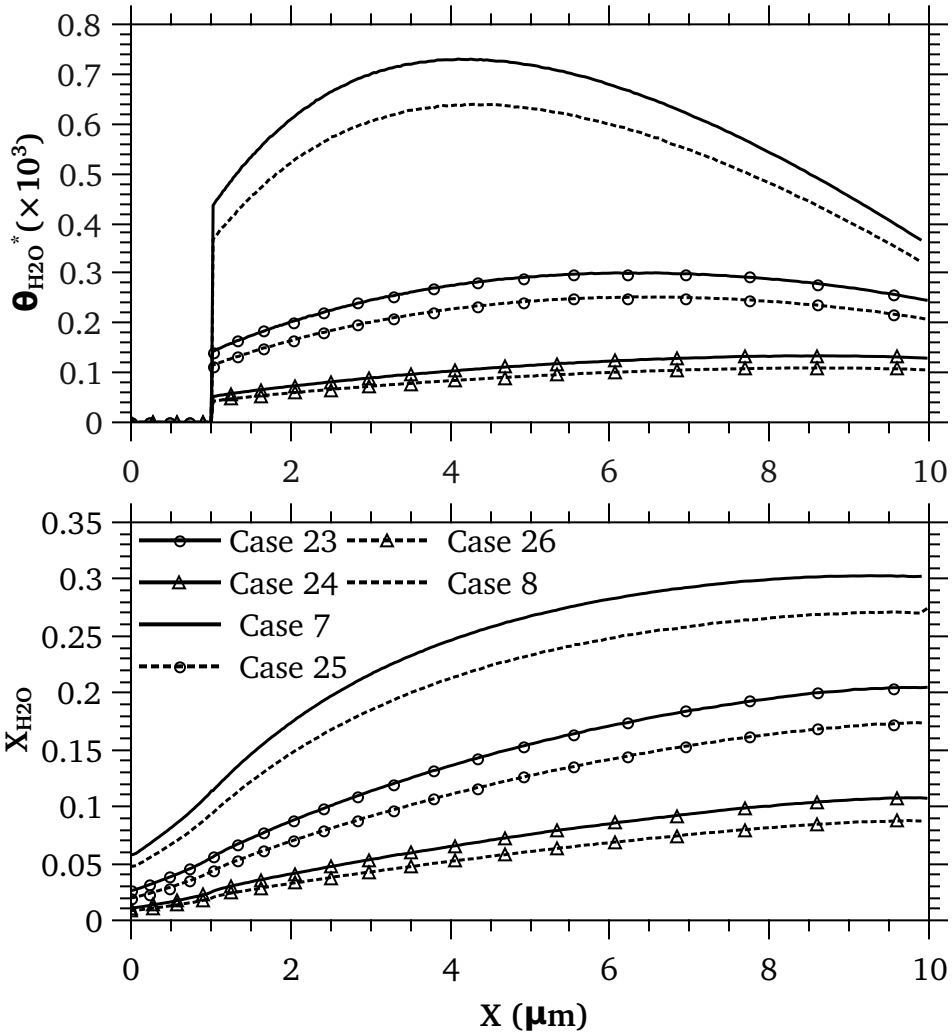

Figure 4.20: Effects of geometry on $\theta_{H_2O^*}$ at stoichiometric and fuel rich conditions

	T_w	T_{in}	H	p_{in}	Kn_{in}	Kn_{out}	Re_{in}	Ma_{out}	ϕ	$\dot{m}''$
C4	1000	300	0.5	1.56	0.072	0.375	0.9	0.19	0.28	25
C9	1000	500	0.5	1.85	0.101	0.375	0.7	0.15	0.28	25
C10	1000	700	0.5	2.13	0.123	0.375	0.6	0.12	0.28	25

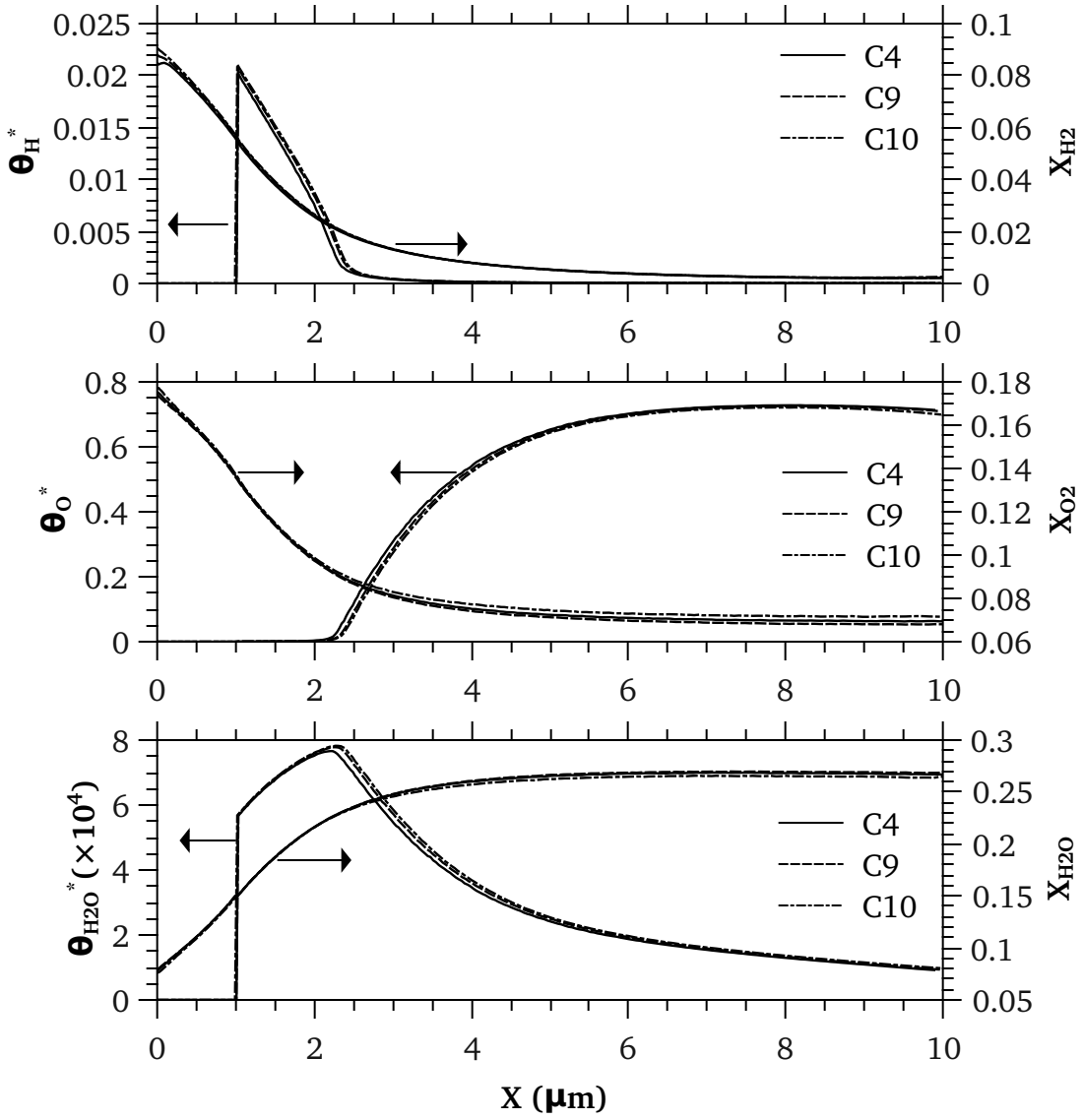

Figure 4.21: Effects of inlet temperature on surface coverages; Cases 4, 9, and 10

4.4.4 Effects of wall temperature

Fuel lean Cases

Figure 4.22 shows effects of the wall temperature ranging from 600K to 1000K on θ_{H^*}. As seen, increasing surface temperature decreases initial θ_{H^*} but lengthens effective reaction length. To find the reason of higher θ_{H^*} at lower wall temperatures, an isothermal flow of Case 14 in which T_{in}=T_w=300K is studied. At this temperature no reactions will take place on the surface and the results show that θ_{H^*} is almost equal to unity and θ_{O^*} is very close to zero. It happens because of two reasons: first, H_2 adsorption is of the first order in terms of θ_{Pt^*} and second, MCR of H_2 molecules at these conditions is more than twice as that of O_2. Consequently, H_2 molecules occupy free Pt^* sites on the catalytic surface faster and hence, θ_{Pt^*} decreases. Lower θ_{Pt^*} reduces the chance of adsorption for O_2 molecules even more, since it is of second order with regards to θ_{Pt^*}. The above process takes place when T_w <500K where surface reactions are inefficient. In such a case, surface reactions are not triggered from the beginning of the catalytic section and start in the middle of the channel. This leads to sudden changes in surface coverage values making the ODE system unstable. In addition, the point at which reactions are triggered is close to the outlet, leaving the reaction zone small and hence, inefficient. As T_w goes beyond 500K, H_2 molecules adsorbed on the surface will be consumed by catalytic reactions limiting θ_{H^*} to a maximum value. It is clear that by further elevation of T_w, the rate of H_2 conversion will increase and therefore, maximum value of the θ_{H^*} will be reduced. Another observation from Figure 4.22 is shorter effective reaction length for lower T_w Cases. The reason is the higher H_2 conversion rate for these Cases due to higher θ_{H^*} (see Figure 4.26). This reduces X_{H_2} next to the surface decreasing MCR of H_2 molecules to a point where the O_2 adsorption exceeds H_2 and as seen in Figure 4.23, θ_{O^*} rises afterwards. It seems the opposite effects of higher θ_{H^*} and shorter effective reaction length lead to a noticeable result that the X_{H_2} distribution is almost not affected by variations of θ_{H^*}. The X_{O_2} distribution also remains the same despite obvious changes of reactant surface coverages. lower T_w also neutralizes the acceleration caused by the upper bound of θ_{H^*}.

Similar behaviour is observed for $\theta_{H_2O^*}$ and X_{H_2O} distributions shown in Figure 4.24. As shown, increasing T_w from 600K to 1000K enhances X_{H_2O} at the outlet by about 8%.

In addition, $\theta_{H_2O^*}$ for lower T_w are significantly higher. This happens due to the lower desorption of H_2O at lower T_w. considering the fact that the conversion rate is almost the same for all the cases explained above, $\theta_{H_2O^*}$ increases in order to compensate the adverse effect of lower T_w. This is a noteworthy result suggesting that increasing T_w is not critical due to its negligible contribution to the reactor performance for the H_2 oxidation. Practically, it is desirable to design the reactor to work with the minimum T_w at which effective surface reactions is created saving energy and realizing the design. Figure 4.25 also shows higher θ_{OH^*} for lower T_w. This behaviour results in higher $\theta_{H_2O^*}$ through subreactions 6 and 8 listed in Table 4.1.

Stoichiometric and fuel rich Cases

To investigate effects of the wall temperature at higher values of ϕ, stoichiometric and fuel rich (ϕ=1.5) conditions are considered. As shown in Figure 4.29, there is no water production for T_w=400K since the H_2 desorption rate is almost zero leaving no room for O_2 molecules to be adsorbed. By increasing T_w to 600K, there is a big jump in water production as reactions start. Further elevation of T_w to 800K causes 18% more water production in comparison to 4% for fuel lean Cases (ϕ=0.28); however, if T_w is increased more to 1000K, there is almost no change in X_{H_2O} distribution for the catalytic length of the channel. This behaviour is similar to that seen for fuel lean Cases and comes from the same root. Figure 4.27 shows that θ_{H^*} and X_{H_2} dramatically decrease at high T_w. This largely countervails the higher reaction rate caused by higher T_w and therefore, increasing T_w does not considerably improve the conversion rate even at stoichiometric conditions.

Increasing the magnitude of ϕ to 1.5 also shows similar behaviour as represented in Figure 4.32. As T_w goes up from 600K to 800K, the value of X_{H_2O} at the outlet rises by 25% and further elevation of T_w from 800K to 1000K increases X_{H_2O} by less than 4%. In order to evaluate and compare the performance of the Cases studied in this section, molar flow distributions of water produced in surface reactions are shown in Figure 4.33. As observed, the water flow of Cases 7 and 19 have the same distributions. This again confirms that increasing T_w beyond 800K has no effect on the conversion rate. Having a fuel rich condition by increasing ϕ from 1 to 1.5 slightly decreases the water production

	T_w	T_{in}	H	p_{in}	Kn_{in}	Kn_{out}	Re_{in}	Ma_{out}	ϕ	$\dot{m}''$
C4	1000	300	0.5	1.56	0.072	0.375	0.9	0.19	0.28	25
C11	600	300	0.5	1.66	0.068	0.225	0.9	0.12	0.28	25
C12	700	300	0.5	1.64	0.069	0.262	0.9	0.14	0.28	25
C13	800	300	0.5	1.61	0.07	0.3	0.9	0.15	0.28	25

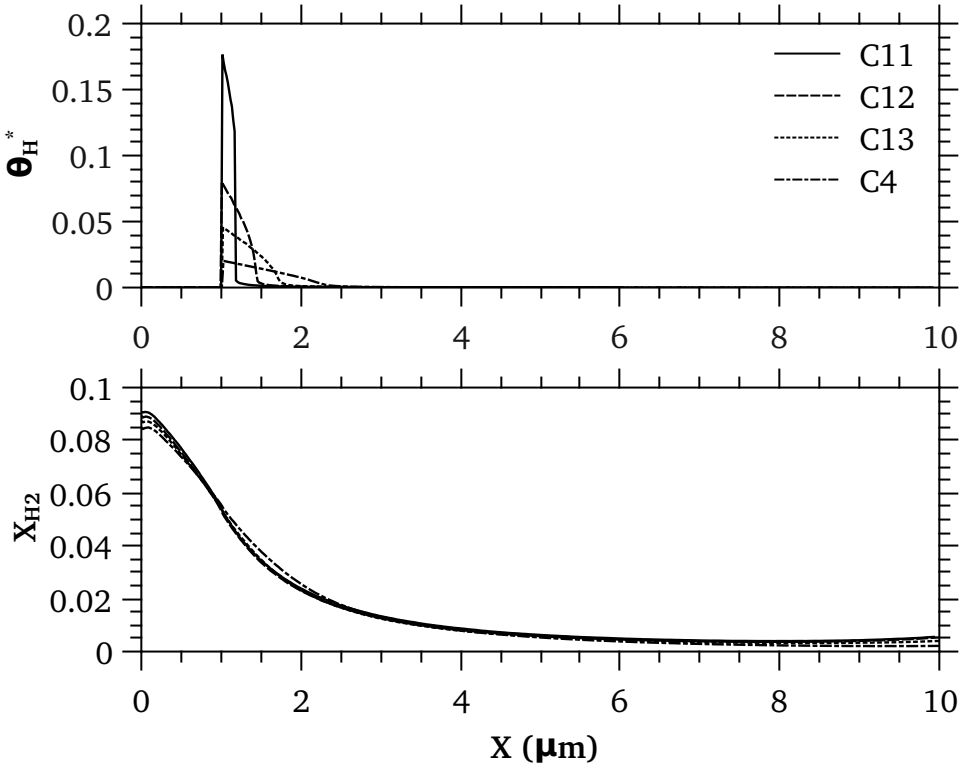

Figure 4.22: Effects of wall temperature on θ_{H^*} and X_{H_2}

	T_w	T_{in}	H	p_{in}	Kn_{in}	Kn_{out}	Re_{in}	Ma_{out}	ϕ	$\dot{m}''$
C4	1000	300	0.5	1.56	0.072	0.375	0.9	0.19	0.28	25
C11	600	300	0.5	1.66	0.068	0.225	0.9	0.12	0.28	25
C12	700	300	0.5	1.64	0.069	0.262	0.9	0.14	0.28	25
C13	800	300	0.5	1.61	0.07	0.3	0.9	0.15	0.28	25

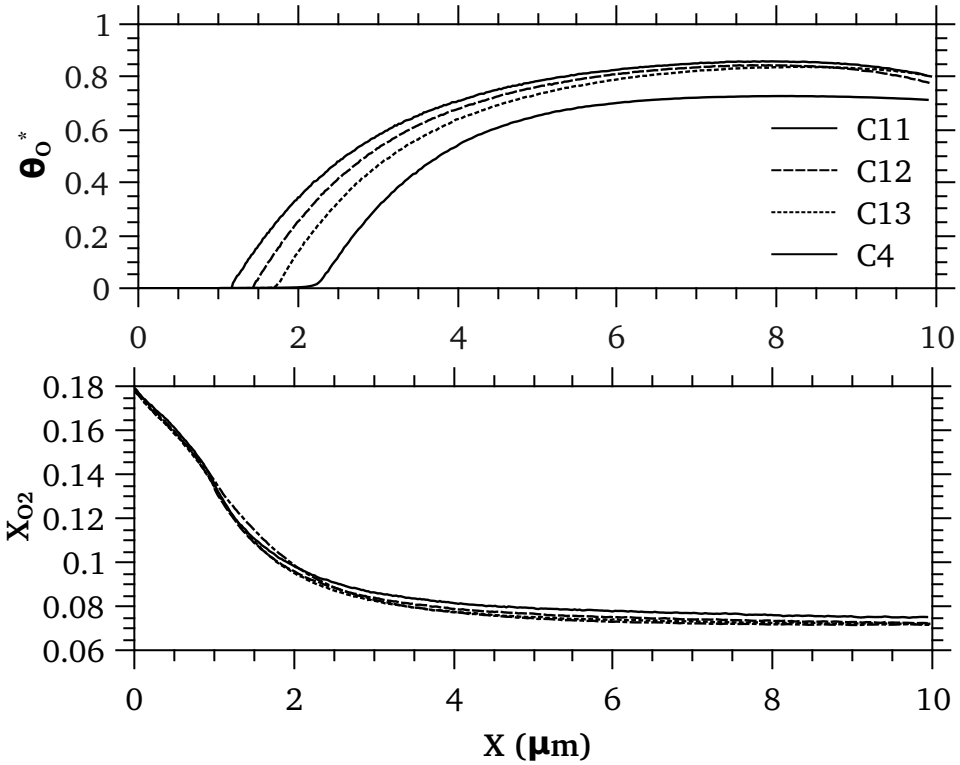

Figure 4.23: Effects of wall temperature on θ_{O^*} and X_{O_2}

	T_w	T_{in}	H	p_{in}	Kn_{in}	Kn_{out}	Re_{in}	Ma_{out}	ϕ	$\dot{m}''$
C4	1000	300	0.5	1.56	0.072	0.375	0.9	0.19	0.28	25
C11	600	300	0.5	1.66	0.068	0.225	0.9	0.12	0.28	25
C12	700	300	0.5	1.64	0.069	0.262	0.9	0.14	0.28	25
C13	800	300	0.5	1.61	0.07	0.3	0.9	0.15	0.28	25

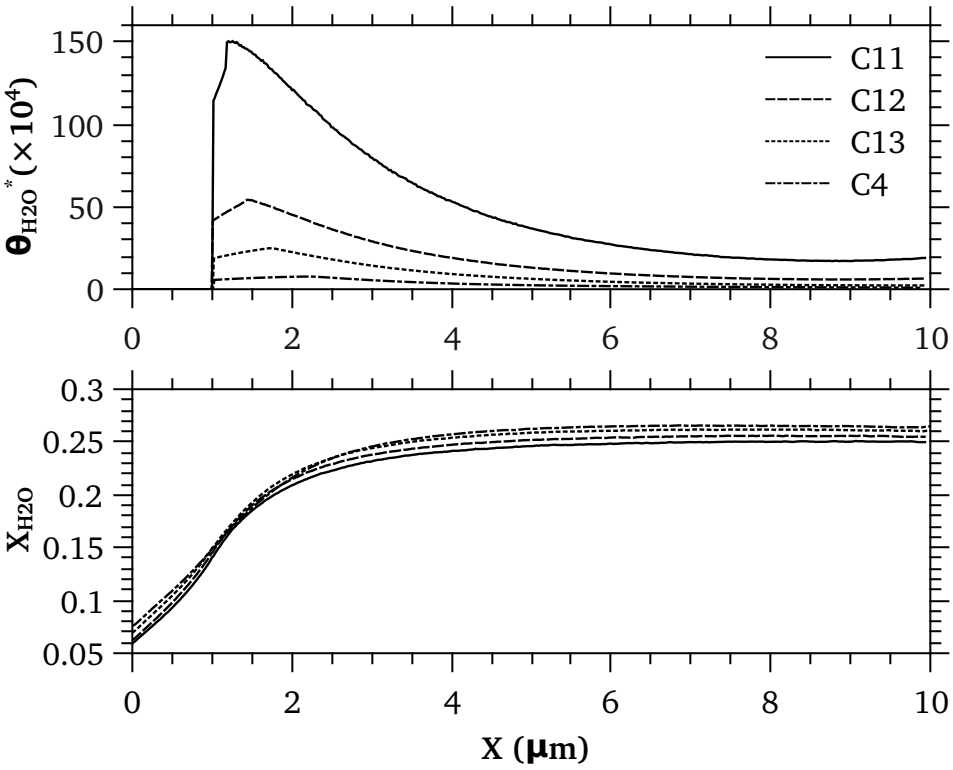

Figure 4.24: Effects of wall temperature on $\theta_{H_2O^*}$ and X_{H_2O}

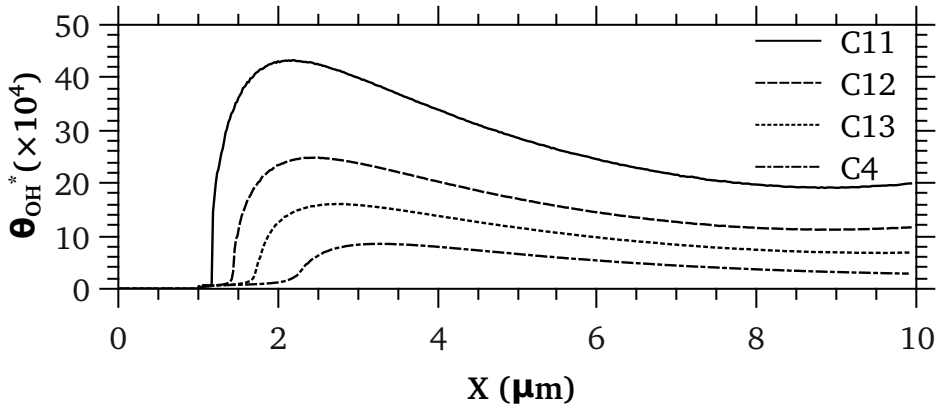

Figure 4.25: Effects of wall temperature on θ_{OH^*}

	T_w	T_{in}	H	p_{in}	Kn_{in}	Kn_{out}	Re_{in}	Ma_{out}	ϕ	$\dot{m}''$
C4	1000	300	0.5	1.56	0.072	0.375	0.9	0.19	0.28	25
C11	600	300	0.5	1.66	0.068	0.225	0.9	0.12	0.28	25
C12	700	300	0.5	1.64	0.069	0.262	0.9	0.14	0.28	25
C13	800	300	0.5	1.61	0.07	0.3	0.9	0.15	0.28	25

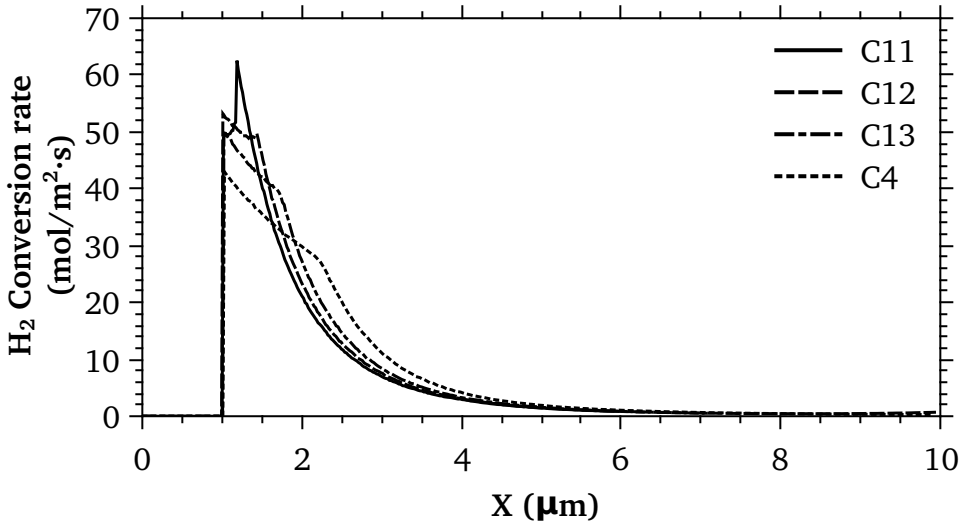

Figure 4.26: Effects of wall temperature on the conversion rate of H_2

rate for Cases 8 and 22 as seen in Figure 4.33. In addition, the difference of T_w for these two Cases makes very little change. Conversion efficiencies of Cases 7 and 19 are 65% and 64.7%, Cases 8 and 22 are 50% and 47%, and Cases 18 and 21 are 60% and 42%, respectively.

4.4.5 Effect of mass flux

Increasing the mass flux requires elevating inlet pressure as seen in Table 4.2 for Cases 4, 15, and 16. Higher inlet pressure results in higher MCR of gas molecules on the surface leading to higher reactant surface coverages as shown in Figure 4.34. This augments the surface reaction rate and therefore, H_2 molecules adjacent to the surface are adsorbed and converted more rapidly. This quickly lowers the MCR of H_2 molecules and θ_{H^*} along the channel and hence, shortens the effective reaction length. Figure 4.36 also shows that high reaction rate of Case 4 causes $\theta_{H_2O^*}$ to go initially higher than Case 15; however, $\theta_{H_2O^*}$ for Case 15 is higher for the rest of channel due to its longer effective reaction length. A notable observation here is that although the mass flux is increased by a constant amount from Case 16 to Case 4, results of Case 16 show larger differences from the other Cases. Especially, both X_{H_2O} and $\theta_{H_2O^*}$ in Figure 4.36 are considerably higher for Case 16. It seems that this behaviour is due to highly diffusive flow of this Case causing diffusion of H_2O molecules towards upstream. As shown in Figure 4.37, molar flow of H_2 for all of the cases drops to almost zero and it was found that efficiencies of them are all greater than 99%. This confirms that higher X_{H_2O} for Case 16 is not a result of a higher reaction rate or a higher conversion efficiency. In fact, the amount of converted H_2 molecules is higher as the inlet mass flux increases due to the greater inlet molar flow.

	T_w	T_{in}	H	p_{in}	Kn_{in}	Kn_{out}	Re_{in}	Ma_{out}	ϕ	$\dot{m}''$
C7	1000	300	0.5	1.56	0.072	0.375	0.9	0.19	1.0	25
C17	400	300	0.5	1.7	0.066	0.15	0.9	0.08	1.0	25
C18	600	300	0.5	1.66	0.068	0.225	0.9	0.12	1.0	25
C19	800	300	0.5	1.61	0.07	0.3	0.9	0.15	1.0	25

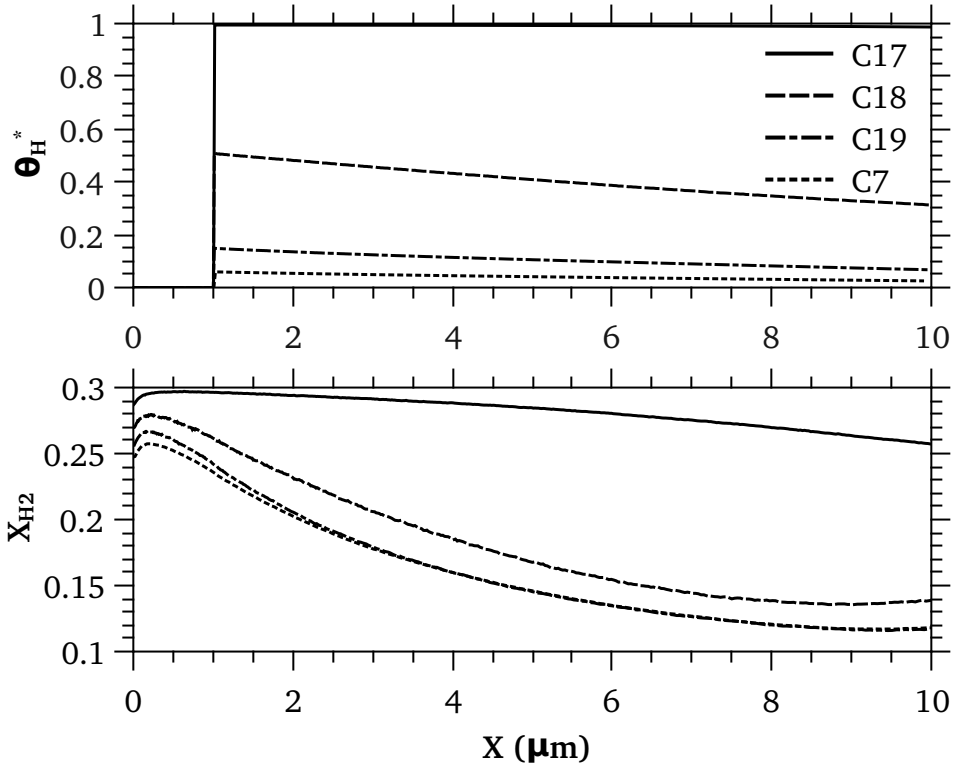

Figure 4.27: Effects of the wall temperature on θ_{H^*} at stoichiometric conditions.

	T_w	T_{in}	H	p_{in}	Kn_{in}	Kn_{out}	Re_{in}	Ma_{out}	ϕ	$\dot{m}''$
C7	1000	300	0.5	1.56	0.072	0.375	0.9	0.19	1.0	25
C17	400	300	0.5	1.7	0.066	0.15	0.9	0.08	1.0	25
C18	600	300	0.5	1.66	0.068	0.225	0.9	0.12	1.0	25
C19	800	300	0.5	1.61	0.07	0.3	0.9	0.15	1.0	25

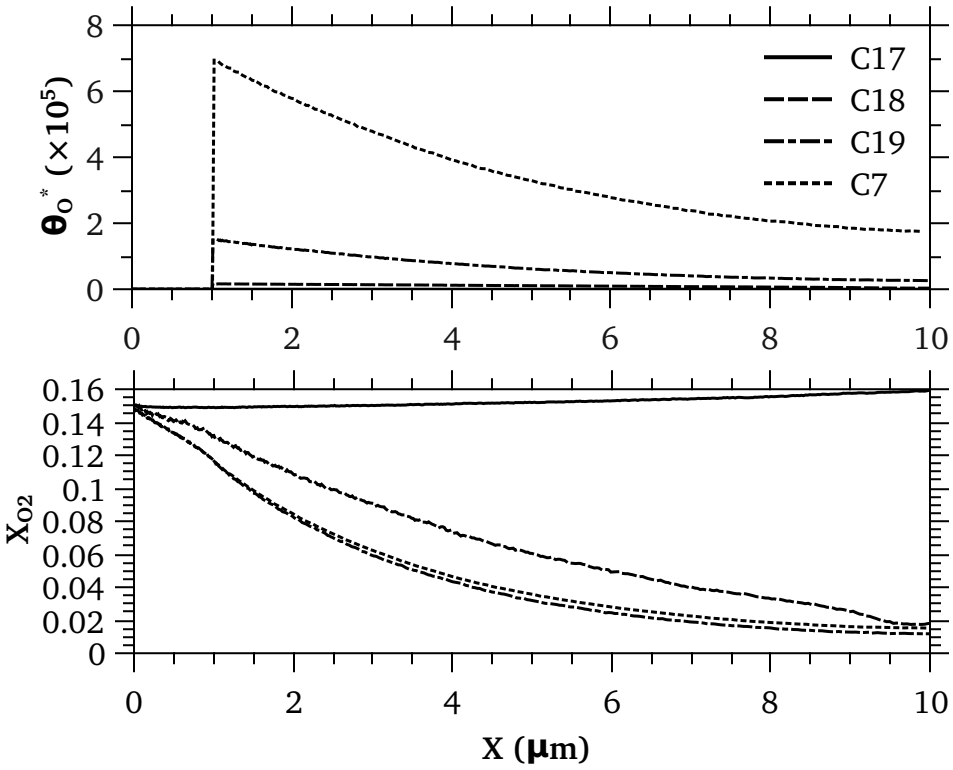

Figure 4.28: Effects of the wall temperature on θ_{O^*} at stoichiometric conditions.

	T_w	T_{in}	H	p_{in}	Kn_{in}	Kn_{out}	Re_{in}	Ma_{out}	ϕ	$\dot{m}''$
C7	1000	300	0.5	1.56	0.072	0.375	0.9	0.19	1.0	25
C17	400	300	0.5	1.7	0.066	0.15	0.9	0.08	1.0	25
C18	600	300	0.5	1.66	0.068	0.225	0.9	0.12	1.0	25
C19	800	300	0.5	1.61	0.07	0.3	0.9	0.15	1.0	25

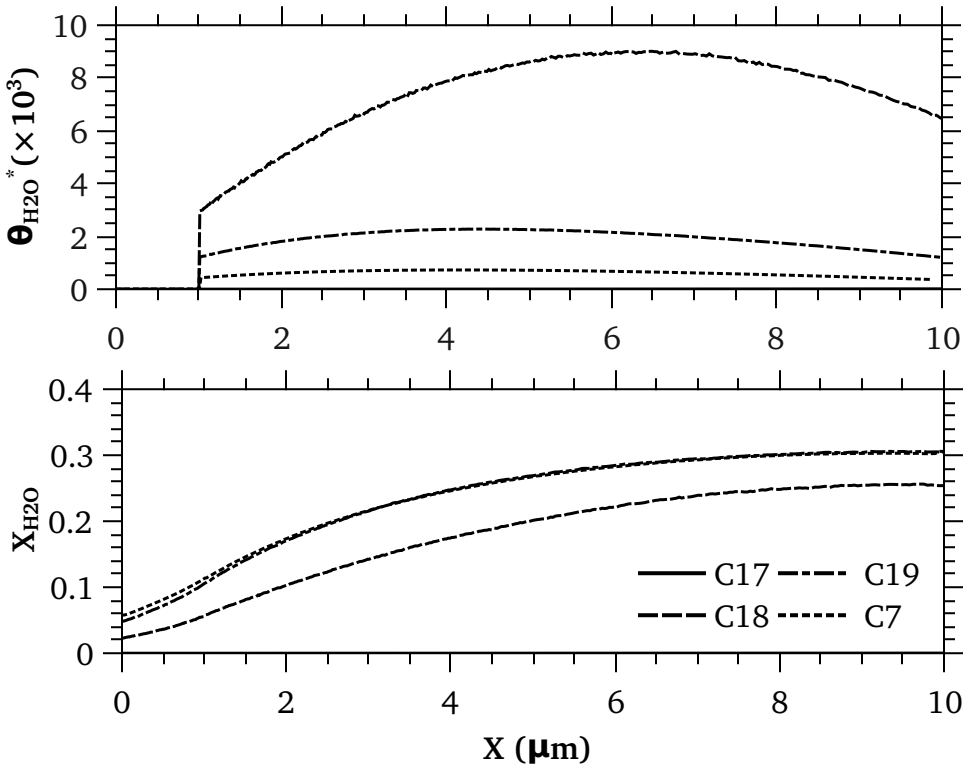

Figure 4.29: Effects of the wall temperature on $\theta_{H_2O^*}$ at stoichiometric conditions.

	T_w	T_{in}	H	p_{in}	Kn_{in}	Kn_{out}	Re_{in}	Ma_{out}	ϕ	$\dot{m}''$
C8	1000	300	0.5	1.56	0.072	0.375	0.9	0.19	1.5	25
C20	400	300	0.5	1.7	0.07	0.15	0.9	0.08	1.5	25
C21	600	300	0.5	1.66	0.07	0.225	0.9	0.12	1.5	25
C22	800	300	0.5	1.61	0.07	0.3	0.9	0.15	1.5	25

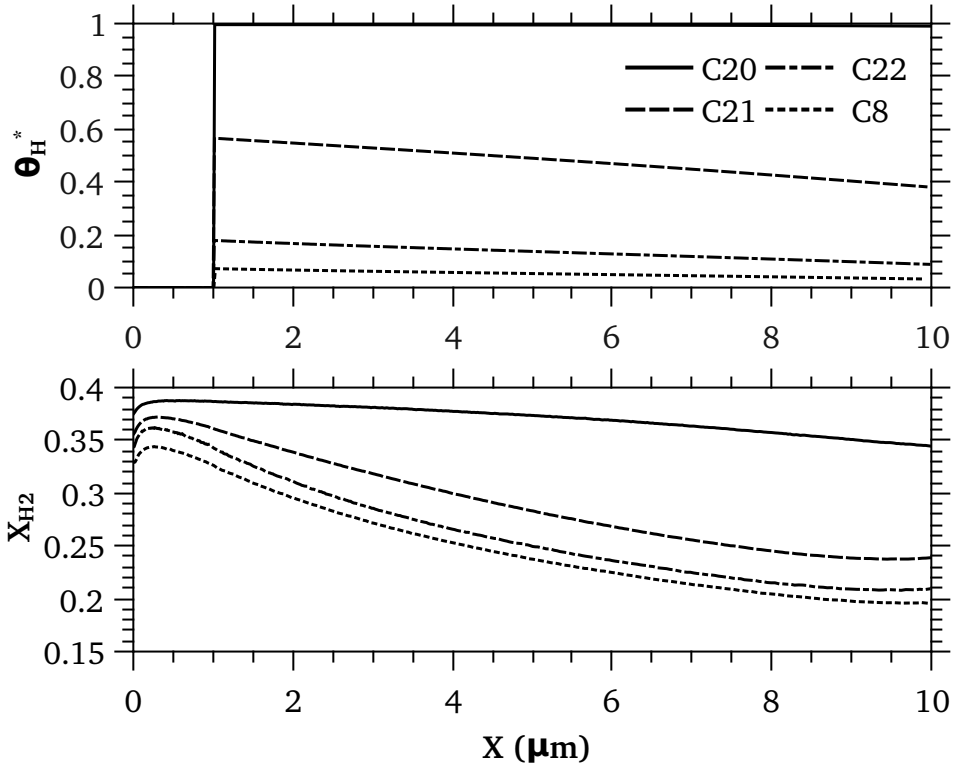

Figure 4.30: Effects of the wall temperature on θ_{H^*} at fuel rich conditions.

	T_w	T_{in}	H	p_{in}	Kn_{in}	Kn_{out}	Re_{in}	Ma_{out}	ϕ	$\dot{m}''$
C8	1000	300	0.5	1.56	0.072	0.375	0.9	0.19	1.5	25
C20	400	300	0.5	1.7	0.07	0.15	0.9	0.08	1.5	25
C21	600	300	0.5	1.66	0.07	0.225	0.9	0.12	1.5	25
C22	800	300	0.5	1.61	0.07	0.3	0.9	0.15	1.5	25

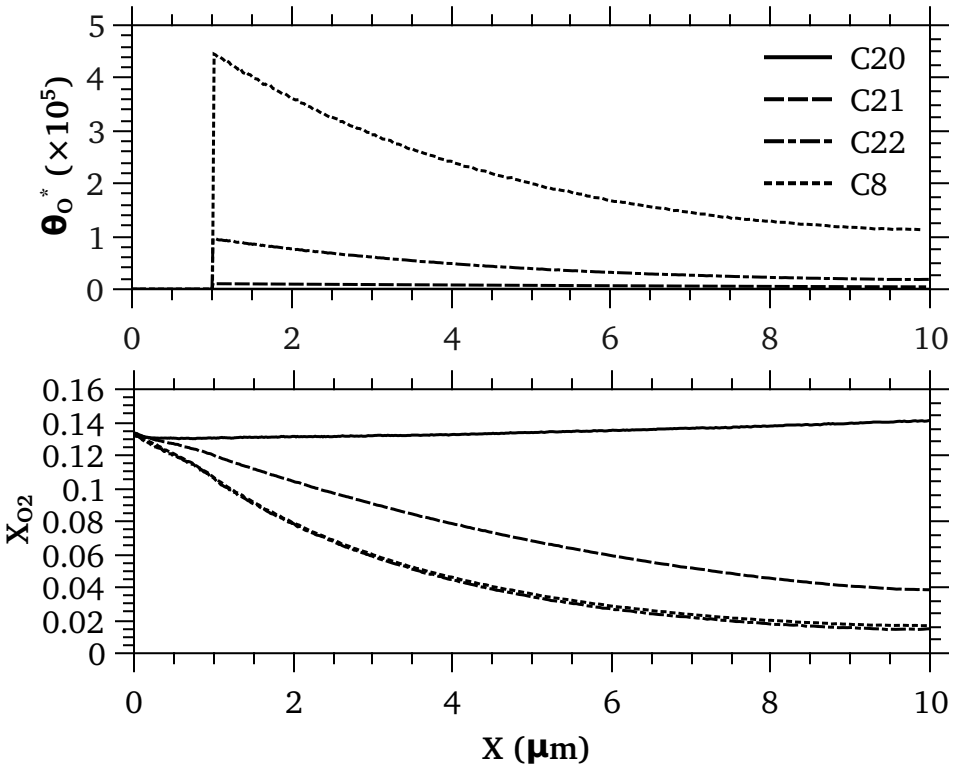

Figure 4.31: Effects of the wall temperature on θ_{O^*} at fuel rich conditions.

	T_w	T_{in}	H	p_{in}	Kn_{in}	Kn_{out}	Re_{in}	Ma_{out}	ϕ	$\dot{m}''$
C8	1000	300	0.5	1.56	0.072	0.375	0.9	0.19	1.5	25
C20	400	300	0.5	1.7	0.07	0.15	0.9	0.08	1.5	25
C21	600	300	0.5	1.66	0.07	0.225	0.9	0.12	1.5	25
C22	800	300	0.5	1.61	0.07	0.3	0.9	0.15	1.5	25

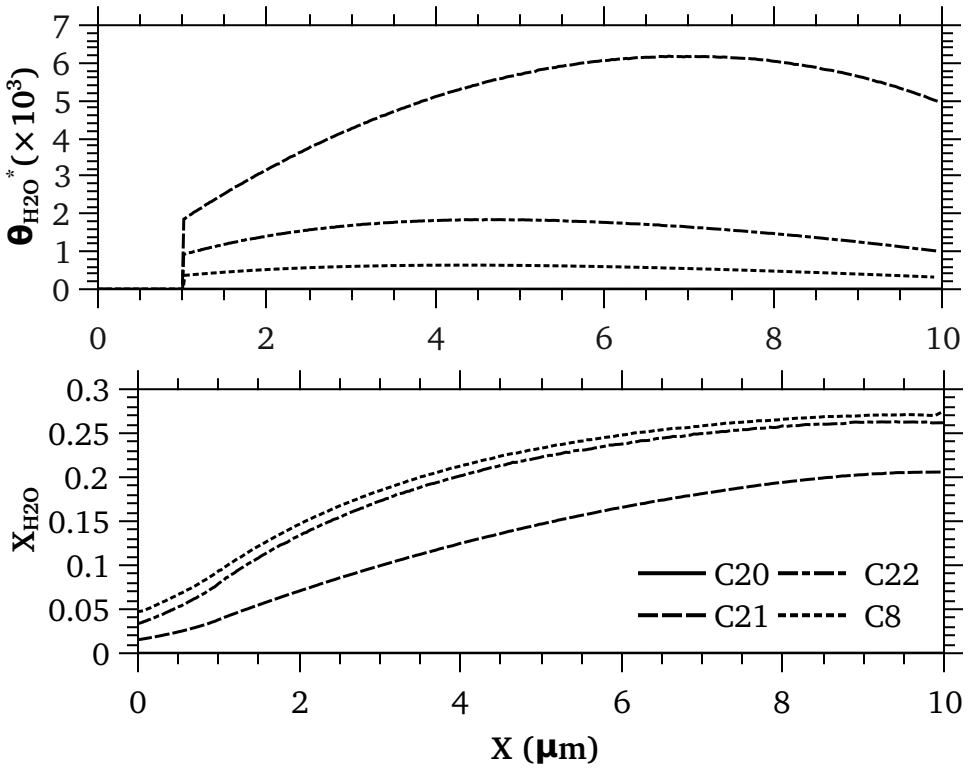

Figure 4.32: Effects of the wall temperature on $\theta_{H_2O^*}$ at fuel rich conditions.

	T_w	T_{in}	H	p_{in}	Kn_{in}	Kn_{out}	Re_{in}	Ma_{out}	ϕ	$\dot{m}''$
C7	1000	300	0.5	1.56	0.072	0.375	0.9	0.19	1.0	25
C8	1000	300	0.5	1.56	0.072	0.375	0.9	0.19	1.5	25
C18	600	300	0.5	1.66	0.068	0.225	0.9	0.12	1.0	25
C19	800	300	0.5	1.61	0.07	0.3	0.9	0.15	1.0	25
C21	600	300	0.5	1.66	0.07	0.225	0.9	0.12	1.5	25
C22	800	300	0.5	1.61	0.07	0.3	0.9	0.15	1.5	25

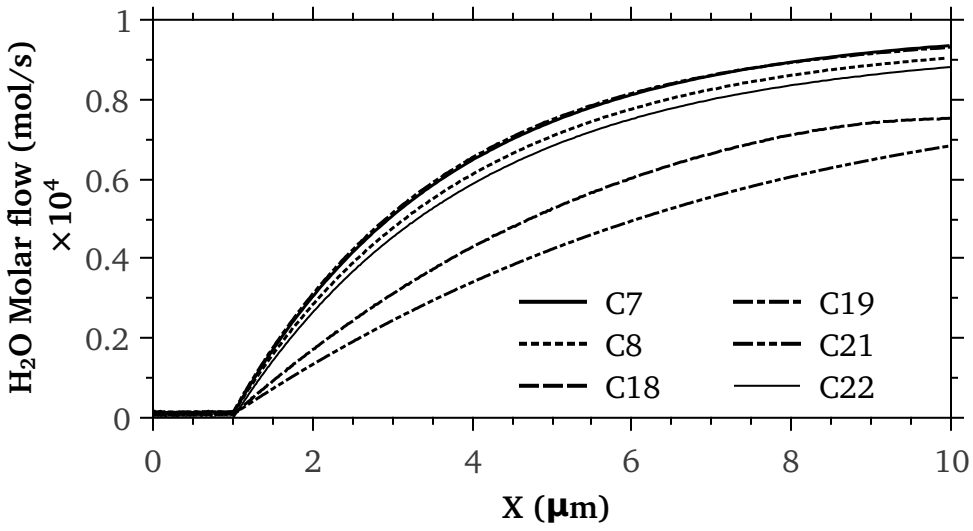

Figure 4.33: Molar flow of H_2O at different T_w under stoichiometric and fuel rich conditions.

	T_w	T_{in}	H	p_{in}	Kn_{in}	Kn_{out}	Re_{in}	Ma_{out}	ϕ	$\dot{m}''$
C4	1000	300	0.5	1.56	0.072	0.375	0.9	0.19	0.28	25
C15	1000	300	0.5	1.33	0.072	0.375	0.5	0.12	0.28	15
C16	1000	300	0.5	1.11	0.072	0.375	0.2	0.04	0.28	5

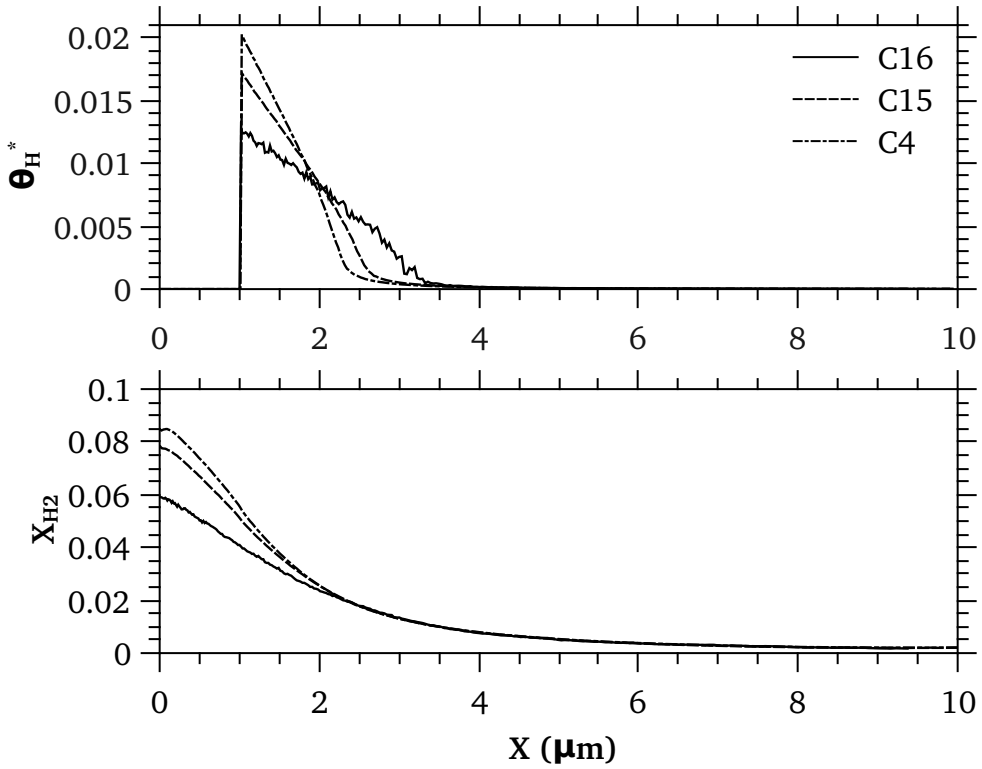

Figure 4.34: Effects of mass flux on θ_{H^*} and X_{H_2}.

	T_w	T_{in}	H	p_{in}	Kn_{in}	Kn_{out}	Re_{in}	Ma_{out}	ϕ	$\dot{m}''$
C4	1000	300	0.5	1.56	0.072	0.375	0.9	0.19	0.28	25
C15	1000	300	0.5	1.33	0.072	0.375	0.5	0.12	0.28	15
C16	1000	300	0.5	1.11	0.072	0.375	0.2	0.04	0.28	5

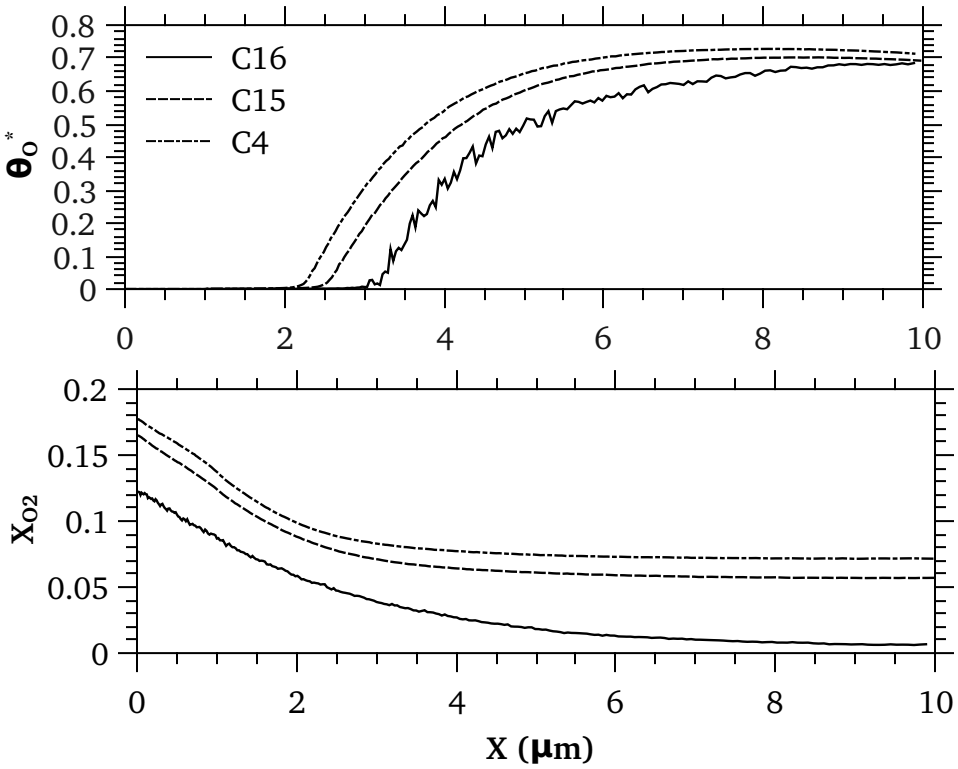

Figure 4.35: Effects of mass flux on θ_{O^*} and X_{O_2}.

	T_w	T_{in}	H	p_{in}	Kn_{in}	Kn_{out}	Re_{in}	Ma_{out}	ϕ	$\dot{m}''$
C4	1000	300	0.5	1.56	0.072	0.375	0.9	0.19	0.28	25
C15	1000	300	0.5	1.33	0.072	0.375	0.5	0.12	0.28	15
C16	1000	300	0.5	1.11	0.072	0.375	0.2	0.04	0.28	5

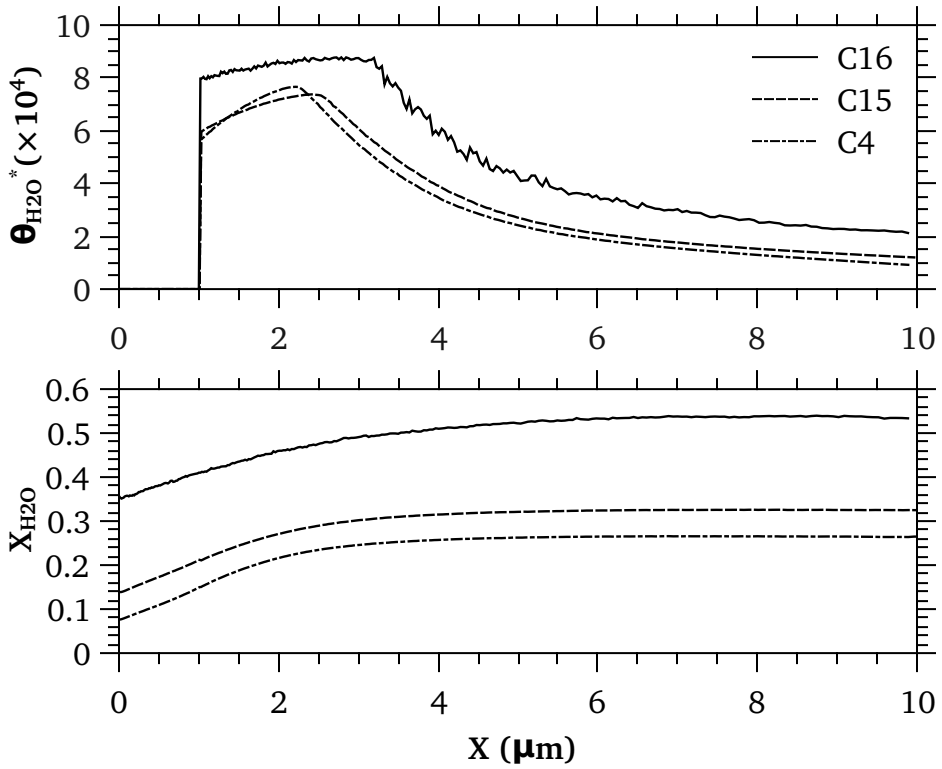

Figure 4.36: Effects of mass flux on $\theta_{H_2O^*}$ and X_{H_2O}.

	T_w	T_{in}	H	p_{in}	Kn_{in}	Kn_{out}	Re_{in}	Ma_{out}	ϕ	$\dot{m}''$
C4	1000	300	0.5	1.56	0.072	0.375	0.9	0.19	0.28	25
C15	1000	300	0.5	1.33	0.072	0.375	0.5	0.12	0.28	15
C16	1000	300	0.5	1.11	0.072	0.375	0.2	0.04	0.28	5

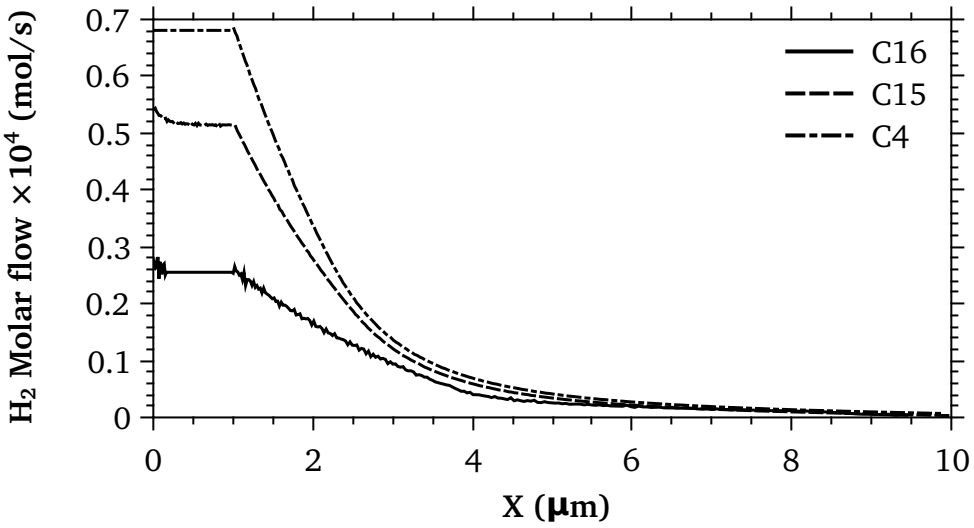

Figure 4.37: Effects of mass flux on molar flow of H_2

4.5 Summary

A method has been developed for coupling DSMC simulations with conventional modelling of heterogeneous chemical reactions on catalytic surfaces. The proposed method can be used in the transition regime ($0.1<Kn<10$) where Navier–Stokes equations break down. This method has been applied to several lean Hydrogen/Air mixture flows in flat channels with platinum coated walls. The results of a case in the slip regime have been compared to conventional Navier–Stokes simulations employing slip/jump boundary conditions and generally very good agreements were observed.

The accuracy of inlet and outlet boundary conditions have also been verified for some sample cases. It has been shown that the mass flux and the equivalence ratio are effectively kept constant at the inlet as well as atmospheric pressure at the outlet. Using the verified code, effects of geometry, equivalence ratio, inlet and wall temperatures, and inlet mass flux on the surface chemical reactions have been examined.

Chapter 5

Conclusions and future works

In this thesis, the fundamental behaviour of multi–component gas flows in micro/nano–channels undergoing heterogeneous catalytic chemical reactions has been studied numerically. This work is primarily focused on nano–scale flows with recent and future applications in mind; especially, miniaturized energy sources such as micro–fuel cells and batteries. Due to prevailing non–equilibrium conditions at these geometries, the DSMC method was employed for its intrinsic ability in modelling rarefied gas flows and its flexibility to incorporate chemical reactions. The objective was achieved in three main steps which are explained below followed by the observations:

1. *Fluid dynamics and heat transfer of multi–component gas micro/nano–flows were investigated and the results were compared with corresponding data from the solution of the Navier-Stokes equations with slip/jump boundary conditions:*

   Generally, very good agreements were observed for all the studied variables. For the slip velocity, the maximum deviation was seen for higher inlet mass flux at the inlet of the channel. The reason is the intense non–equilibrium conditions due to steep velocity gradients at the entrance. The two methods also slightly digress from each other close to the outlet boundary due to the rarefaction effects associated with the sudden pressure drop. It was also seen that the difference between the results becomes higher as the

Knudsen number Kn increases (e.g. reducing the channel height) and/or as the velocity and/or temperature gradients escalate.

Mass concentrations of the species showed very good agreement between the two methods. The maximum deviation was found to be about 8% for H_2. Two reasons contribute in building up this difference: first, the iterative nature of imposing constant mass flux at the inlet causes a little less amount of molecules entering at the boundary than the specified value. Second, the thermal velocity of H_2 is very high due to its very light molecules. This leads to high diffusion rates especially close to the walls where the gas temperature is higher. The resulting upstream diffusion of H_2 creates problems for the Navier–Stokes method in maintaining a constant mass flux, since exclusive data is not accessible in this method for each species.

Thermal results showed better agreement between the methods than fluid dynamics data. The maximum temperature jump was captured at the inlet due to high temperature and velocity gradients at that location. This quantity vanishes by approaching the outlet and it was found that zero temperature gradient at the outlet leads to zero temperature jump and as well, very good compliance of the methods. In addition, outlet conditions such as the pseudo–reservoir length do not affect the thermal variable distributions.

2. *A new pressure boundary condition was introduced for multi–component gas flows, and further improved using the Chapman–Enskog velocity distribution:*

   It is shown that velocity distribution plays an important role in calculating the number flux across a surface; the key part of controlling a boundary pressure. The Maxwell distribution is commonly used for this purpose, however, these values departed increasingly along the channel from the number flux values sampled directly from DSMC. The Chapman-Enskog distribution is employed as a remedy and the results are compared to the first equivalent part of an extended channel, chosen as the reference solution. It is found that this distribution has higher accuracy for simulating species compositions at high Kn and low Peclet number Pe flows compared to the Maxwell distribution. A distribution with higher order of accuracy, however, is required for heavier molecules in cases of lower Kn or higher stream velocity.

3. *A new method of coupling the flow field simulated by DSMC and surface chemical reactions simulated by conventional conservation ODE system was introduced, and the effects of geometrical and boundary specifications on surface reactions were investigated:*

   The conversion rate of the reactor is higher for smaller channels due to the higher inlet pressure caused by the constant mass flux, and the larger surface to volume ratio at nano scales. This reduces the Mean Collision Rate (MCR) of H_2 molecules on the surface more rapidly for smaller channels and therefore, for fuel lean cases, the hydrogen coverage θ_{H^*} reaches zero at a shorter distance from the entrance within the channel. Despite this, the water coverage $\theta_{H_2O^*}$ and the water molar concentration X_{H_2O} have higher values throughout the channel. The comparison of the molar flow of H_2 shows that greater portion of H_2 molecules entering the channel are converted inside smaller channels and hence their performance is higher. However, for the smallest channel Case 4, about 95% of H_2 is converted in the first half of the channel. This suggests that adjusting the equivalence ratio proportional to the channel height can result in more effective use of the channel length.

   The optimum value of the equivalence ratio ϕ leading to the maximum efficiency is on the fuel lean side with a value about 0.5. The reason is that a higher H_2 content will result in a lower θ_{O^*} which is the limiting factor of the reactions.

   Inlet temperature of the gas flow has almost no effect on the surface reactions. It was found that the important temperature influencing the surface reactions (apart from the wall temperature) is the gas temperature at the vicinity of the surface. This temperature rapidly rises to surface temperature minimizing the effect of its initial value. This is a favourable result for using micro-reactors in applications since, high surface temperatures of the channels will affect the upstream making it difficult to keep the inlet temperature at an arbitrary low value.

   It was observed that increasing the wall temperature T_w from 600K to 1000K makes a small improvement (about 8%) on the efficiency. Three factors contribute to this behaviour: higher θ_{H^*} at lower T_w, higher surface reaction rates at higher T_w, and shorter effective reaction length at lower T_w. These factors make complex distributions for surface coverages resulting in higher reaction rates at lower T_w; however, this

condition lasts for a shorter distance and therefore, overall amount of water produced remains almost the same. The results for cases at stoichiometric and fuel rich (ϕ=1.5) conditions showed about 20% rise in performance as T_w increases from 600K to 800K but almost no change from 800K to 1000K. This is also a favourable result since lower surface temperature will facilitate putting such reactors into application.

Increasing inlet mass flux increases surface coverages and therefore elevates reaction rates. It was found that this enhancement does not change linearly with the inlet mass flux and is higher for lower mass fluxes. The efficiency of the reactions however does not change with increasing the inlet mass flux from 5kg/m^2.s to 25kg/m^2.s inside a channel with 500nm height and remains about 99%. This means that by increasing the inlet mass flux, the flow rate of products will be augmented.

There is a potential for further research based on the work described in this thesis to examine different aspects of chemically reacting nano–flows. Some of the possibilities are listed as follows:

- Although parallel channels studied in this thesis seem easier for manufacturing and utilization in wafer–like structured micro/nano–reactors, different geometries such as circular or rectangular channel reactors can also be considered. Circular channel can still be modeled using a 2–dimensional geometry domain by making some modifications to the Direct Simulation Monte Carlo (DSMC) algorithm as suggested by Bird [1]. The same methodology of this thesis for modeling surface chemical reactions can be adopted on the catalytic walls. Possible applications can be thought of as using perforated plates or porous media with circular nano–passages for the reactor core. Rectangular channels with different aspect ratios are also of interest in practice. A 3–dimensional approach is required for modeling this type of channels and therefore, molecular movement and sampling routines should be modified.

- In this thesis, heterogeneous chemical reactions are modeled using species conservation ODE systems derived from the reaction mechanism. This gives the flexibility of using available mechanisms; however, it is also possible to simulate surface reactions using the generalized Monte Carlo method, mostly used for discrimination and extraction of

the reaction kinetics [62, 63]. There are two advantages associated with employing this method: first, the nature of DSMC conforms well with such modeling schemes; therefore, the implementation is easier and effective. Second, this will make the simulation capable of handling special reactions that may happen in molecular scales and it is difficult to distinct their mechanism with experiment. On the other hand, this kind of modeling will add considerable computational cost to DSMC which itself is very demanding in this regard.

- In this thesis only catalytic oxidation of hydrogen was simulated. It is possible to incorporate different kinds of reactions as long as their kinetics are known. The decomposition of ammonia on ruthenium or electro–chemical reactions taking place in micro–porous membranes of fuel–cells are useful examples which are beneficial for developing future miniaturized energy sources.

- Effects of using different catalytic surface configurations like porous surfaces and packed bed catalysts can also be studied using this method. Also, effects of diffusion of surface species on the distribution of surface coverages can be considered. Surface diffusions take place on the catalytic walls and are driven by surface coverage gradients.

- As shown in the reacting flow simulations, rapid consumption of hydrogen leads to lack of hydrogen molecules in the middle of the channel due to rarefaction. This makes distributions of surface coverages, gas concentrations, and consumption/production complicated. Based on our studies, as the rarefaction increases, these distributions become even more complicated since other reactant species especially oxygen will be totally consumed as well. Therefore, in the present study, $Kn < 0.4$ was considered to deal with the rarefaction effects on hydrogen. As the next step, reacting flows with higher values of Kn can also be modeled and the obtained results can be interpreted based on the explanations of the current work.

Appendices

Appendix A

Evaluation of tensors A, B, and C of the Chapman–Enskog expansion

In this section, the equations required to evaluate the components of the matrices $\underline{\underline{B}}$, $\underline{\underline{A}}$, and $\underline{\underline{D}}$ used in Section 3.3 are presented. The derivation of these equations is similar to [49, 50]; however, they are organized for easier implementation and to be consistent with the terminology of this thesis. In addition, in Section A.3, the results of the developed code for predicting the parameters involved in the equations are demonstrated and verified against [49, 50].

A.1 Evaluation of the tensor B

The tensors $\underline{\underline{B}}_1$ and $\underline{\underline{B}}_2$, associated to the components 1 and 2 can be expanded in terms of the following series:

$$\begin{aligned}
&\underline{\underline{B}}_1 = \sum_{\substack{p=-\infty \\ p\neq 0}}^{\infty} b_p \underline{\underline{b}}_1^{(p)}, && \underline{\underline{B}}_2 = \sum_{\substack{p=-\infty \\ p\neq 0}}^{\infty} b_p \underline{\underline{b}}_2^{(p)}, && \\
&\underline{\underline{b}}_1^{(p)} \equiv 0, && \underline{\underline{b}}_2^{(-p)} \equiv 0, && (p<0) \\
&\underline{\underline{b}}_1^{(p)} \equiv S_{5/2}^{(p-1)}(\mathscr{C}_1^2)\mathring{\underline{\underline{\mathscr{C}}}}_1\underline{\underline{\mathscr{C}}}_1, && \underline{\underline{b}}_2^{(-p)} \equiv S_{5/2}^{(p-1)}(\mathscr{C}_2^2)\mathring{\underline{\underline{\mathscr{C}}}}_2\underline{\underline{\mathscr{C}}}_2, && (p>0)
\end{aligned} \tag{A.1}$$

In which, $\underline{\mathscr{C}} = \underline{c}'/V_{mp}$ and $S_m^{(n)}(x)$ is defined as [28]:

$$S_m^{(n)}(x) = \sum_{p=0}^{n} \frac{(n+m)!}{p!\,(n-p)!\,(m+p)!}(-x)^p \tag{A.2}$$

The magnitudes of Sonine polynomial terms rapidly drop to zero as their order increases and therefore, we just consider the first order term $S_m^{(0)}(x)$ following the Chapman-Enskog methodology. This way, $\underline{\underline{B}}_1$ and $\underline{\underline{B}}_2$ are reduced to $\underline{\underline{B}}_1 = b_1 \mathring{\underline{\mathscr{C}}}_1 \underline{\mathscr{C}}_1$ and $\underline{\underline{B}}_2 = b_{-1} \mathring{\underline{\mathscr{C}}}_2 \underline{\mathscr{C}}_2$ and the values of b_1 and b_{-1} are obtained using the following system of equations:

$$\begin{bmatrix} b_{-1-1} & b_{-11} \\ b_{1-1} & b_{11} \end{bmatrix} \begin{bmatrix} b_{-1} \\ b_1 \end{bmatrix} = \begin{bmatrix} \beta_{-1} \\ \beta_1 \end{bmatrix} \tag{A.3}$$

where the values of β are:

$$\beta_{-1} = \tfrac{5}{2} n_2/n_0^2, \quad \beta_1 = \tfrac{5}{2} n_1/n_0^2, \tag{A.4}$$

The values of b_{pq} in Equation (A.3) are related to the molecular properties and the model of molecular interaction and are expressed as [49]:

$$\begin{aligned} b_{-1-1} &= x_2^2[4\Omega_2^{(2)}(2)] + x_1 x_2 \left\{ \tfrac{80}{3}(M_1 M_2)\Omega_{12}^{(1)}(1) + 8M_1^2 \Omega_{12}^{(2)}(2) \right\} \\ b_{-11} &= b_{1-1} = x_1 x_2 \left\{ -\tfrac{80}{3}(M_1 M_2)\Omega_{12}^{(1)}(1) + 8M_1 M_2 \Omega_{12}^{(2)}(2) \right\} \\ b_{11} &= x_1^2[4\Omega_1^{(2)}(2)] + x_1 x_2 \left\{ \tfrac{80}{3}(M_1 M_2)\Omega_{12}^{(1)}(1) + 8M_2^2 \Omega_{12}^{(2)}(2) \right\} \end{aligned} \tag{A.5}$$

where $\Omega_p^{(\ell)}(r)$ are defined as [28]:

$$\Omega_{12}^{(\ell)}(r) = \frac{1}{2}\sigma_{12}^2 \left(\frac{2\pi kT}{m_0 M_1 M_2} \right)^{1/2} W_{12}^{(\ell)}(r) \tag{A.6}$$

$$\Omega_1^{(\ell)}(r) = \sigma_1^2 \left(\frac{\pi kT}{m_1} \right)^{1/2} W_1^{(\ell)}(r) \tag{A.7}$$

$$\Omega_2^{(\ell)}(r) = \sigma_2^2 \left(\frac{\pi kT}{m_2} \right)^{1/2} W_2^{(\ell)}(r) \tag{A.8}$$

where W integrals are:

$$W_q^{(\ell)}(r) = 2 \int_0^\infty \exp(-g^2) g^{2r+3} \int_0^\pi \left(1 - \cos^\ell \chi\right) \left(\frac{b}{\sigma_q} \right) d\left(\frac{b}{\sigma_q} \right) dg \tag{A.9}$$

in which, parameters b and χ are associated with the molecular collision model. The Hard Sphere (HS) collision model is used in this study in which, b is related to χ as $b = -\sigma_{12} cos(\chi/2)$. Substituting this into Equation (A.9) gives:

$$W_q^{(\ell)}(r) = \frac{1}{4}\left[2 - \frac{1}{1+\ell}\left(1 + (-1)^{\ell}\right)\right](1+r)! \tag{A.10}$$

which is independent of q. Using the equations of this section, the procedure of determining tensor $\underline{\underline{B}}$ is to substitute values of b_{pq} and β calculated from Equation (A.5) and Equation (A.4) into equation Equation (A.3), and solving the corresponding system of linear equations. This gives the magnitudes of b_p by which the components of $\underline{\underline{B}}$ are calculated from Equation (A.1).

A.2 Evaluation of vectors A and D

The Chapman–Enskog solution of vectors $\underline{A}$ and $\underline{D}$, which are the remaining unknowns of the perturbation function Φ^1, starts with the definition of $\underline{\tilde{A}}$, as follows [28]:

$$\underline{\tilde{A}} = \underline{A} - k_T \underline{D} \tag{A.11}$$

where, k_T is the thermal diffusion coefficient for the gas mixture and will be independently evaluated from vector $\underline{D}$ components at the end of the solution. The vectors $\underline{\tilde{A}}$ and $\underline{D}$ are then expressed in terms of the following series:

$$\underline{\tilde{A}}_1 = \sum_{\substack{p=-\infty \\ p\neq 0}}^{\infty} a_p \underline{a}_1^{(p)}, \quad \underline{\tilde{A}}_2 = \sum_{\substack{p=-\infty \\ p\neq 0}}^{\infty} a_p \underline{a}_2^{(p)}, \tag{A.12}$$

$$\underline{D}_1 = \sum_{p=-\infty}^{\infty} d_p \underline{a}_1^{(p)}, \quad \underline{D}_2 = \sum_{p=-\infty}^{\infty} d_p \underline{a}_2^{(p)}, \tag{A.13}$$

where the components of the vector $\underline{a}^{(p)}$ are [28]:

$$\begin{array}{ll}
\underline{a}_1^{(p)} = \underline{a}_1^{(0)} = M_1^{1/2}\rho_2\underline{\mathscr{C}}_1/\rho_0, & (p=0),\\
\underline{a}_2^{(-p)} = \underline{a}_2^{(0)} = -M_2^{1/2}\rho_1\underline{\mathscr{C}}_2/\rho_0, & (p=0),\\
\underline{a}_1^{(p)} = S_{3/2}^{(p)}(\mathscr{C}_1^2)\underline{\mathscr{C}}_1, & (p>0),\\
\underline{a}_2^{(-p)} = S_{3/2}^{(p)}(\mathscr{C}_2^2)\underline{\mathscr{C}}_2, & (p>0),\\
\underline{a}_1^{(p)} = 0, & (p<0),\\
\underline{a}_2^{(-p)} = 0, & (p<0),
\end{array} \tag{A.14}$$

Using the same argument for evaluation of b_1 and b_{-1}, the first order terms of Sonine polynomials are kept, $S_m^{(0)}(x)$, and then the values of a_p and d_p shown in Equation (A.12) and Equation (A.13) are obtained from:

$$\begin{bmatrix} a_{-1-1} & a_{-11} \\ a_{1-1} & a_{11} \end{bmatrix} \begin{bmatrix} a_{-1} \\ a_1 \end{bmatrix} = \begin{bmatrix} \alpha_{-1} \\ \alpha_1 \end{bmatrix} \tag{A.15}$$

and:

$$\begin{bmatrix} a_{-1-1} & a_{-10} & a_{-11} \\ a_{0-1} & a_{00} & a_{01} \\ a_{1-1} & a_{10} & a_{11} \end{bmatrix} \begin{bmatrix} d_{-1} \\ d_0 \\ d_1 \end{bmatrix} = \begin{bmatrix} 0 \\ \delta_0 \\ 0 \end{bmatrix} \tag{A.16}$$

In the above equations, the values of α and σ for each species are calculated from:

$$\alpha_1 = -\frac{15}{4}\frac{n_1}{n_0^2}\left(\frac{2kT}{m_1}\right)^{1/2}, \alpha_{-1} = -\frac{15}{4}\frac{n_2}{n_0^2}\left(\frac{2kT}{m_2}\right)^{1/2} \tag{A.17}$$

and:

$$\delta_0 = -\frac{3}{2n_0}\left(\frac{2kT}{m_0}\right)^{1/2} \tag{A.18}$$

and the components of coefficient matrices are evaluated from [50]:

$$
\begin{aligned}
a_{-1-1} &= x_2^2\left\{4\Omega_2^{(2)}(2)\right\} + x_1x_2\left\{10(5M_1^3+6M_1M_2^2)\Omega_{12}^{(1)}(1)\right.\\
&\quad \left.-40M_1^3\Omega_{12}^{(1)}(2)+8M_1^3\Omega_{12}^{(1)}(3)+16M_1^2M_2\Omega_{12}^{(2)}(2)\right\}\\
a_{-10} &= x_1x_2\left\{-20(M_1^2M_2^{1/2})\Omega_{12}^{(1)}(1)+8(M_1^2M_2^{1/2})\Omega_{12}^{(1)}(2)\right\}\\
a_{-11} &= x_1x_2\left\{-110M_1^{3/2}M_2^{3/2}\Omega_{12}^{(1)}(1)+40M_1^{3/2}M_2^{3/2}\Omega_{12}^{(1)}(2)\right.\\
&\quad \left.-8M_1^{3/2}M_2^{3/2}\Omega_{12}^{(1)}(3)+16M_1^{3/2}M_2^{3/2}\Omega_{12}^{(2)}(2))\right\}\\
a_{00} &= x_1x_2\left\{8M_1M_2\Omega_{12}^{(1)}(1)\right\}\\
a_{10} &= x_1x_2\left\{20(M_1^{1/2}M_2^2)\Omega_{12}^{(1)}(1)-8(M_1^{1/2}M_2^2)\Omega_{12}^{(1)}(2)\right\}\\
a_{11} &= x_1^2\left\{4\Omega_1^{(2)}(2)\right\} + x_1x_2\left\{10(5M_2^3+6M_1^2M_2)\Omega_{12}^{(1)}(1)\right.\\
&\quad \left.-40M_2^3\Omega_{12}^{(1)}(2)+8M_2^3\Omega_{12}^{(1)}(3)+16M_2^2M_1\Omega_{12}^{(2)}(2)\right\}
\end{aligned}
\tag{A.19}
$$

where the omega functions are the same as Equation (A.6-A.8). It should be noted that the components of the coefficient matrix $\underline{\underline{a}}$ presented above, are off-diagonally symmetric, such that $a_{01} = a_{10}$, $a_{0-1} = a_{-10}$ and $a_{1-1} = a_{-11}$. Now, we are in a position to evaluate the vectors $\underline{A}$ and $\underline{D}$. This is done by substituting Equation (A.18) and Equation (A.19) into Equation (A.16), and also substituting Equation (A.17) and Equation (A.19) into Equation (A.15) and solving the corresponding system of linear equations. This way, the values of a_p and d_p are obtained, which are then used together with Equation (A.14) in order to evaluate the vectors $\underline{\tilde{A}}$ and $\underline{D}$ for each component. The value of k_T is required for further progression, which is calculated from [28]:

$$
k_T = -\frac{5}{2}\left(x_1M_1^{-1/2}d_1 + x_2M_2^{-1/2}d_{-1}\right)/d_0 \tag{A.20}
$$

Having the values of k_T, $\underline{\tilde{A}}$ and $\underline{D}$, it is then possible to evaluate vector $\underline{A}$ from Equation (A.11).

A.3 Chapman-Enskog parameters

The values of (b_{-1}, b_1) are compared with [49] and the values of (a_{-1}, a_1, d_0) are compared with [50] for two binary mixture of noble gases, He/Ne and Ar/Kr, as are shown in Ta-

Table A.1: The molecular mass and diameter data used in [49, 50]

	Molecular mass[a] (amu)	Molecular diameter[a] $\times 10^{-10}$ (m)
He	4.002602	2.193
Ne	20.1797	2.602
Ar	39.948	3.659
Kr	83.897	4.199

[a] The data are at 0°C and 1 atm.

ble A.2 and Table A.3 respectively. The agreement of the results implies that the procedure of calculating these parameters is correctly implemented in the prepared code for the current study. The first order values of (d_{-1}, d_1) are not listed in the mentioned references; however, the verification of the values of transport coefficients, ensures the accurate calculation of parameters correctly. The molecular masses and diameters of He, Ne, Ar and Kr used by Tipton et al. [49] are shown in Table A.1.

Table A.2: The comparison of (b_{-1}, b_1) calculated from Equation (A.3) with [49]

		Current study[a]		Tipton II[a]	
	x_1	b_1	b_{-1}	b_1	b_{-1}
He:Ne	0.1	2.997	1.382	2.998	1.382
	0.5	3.521	1.556	3.523	1.556
	0.9	4.230	1.758	4.232	1.758
Ar:Kr	0.1	2.309	1.694	2.310	1.694
	0.5	2.526	1.840	2.526	1.840
	0.9	2.781	2.009	2.782	2.009

[a] All values are scaled as 1×10^{10} (secˆ-1)

Table A.3: The comparison of (a_{-1}, a_1, d_0) calculated from Equation (A.15) and Equation (A.16) with [50]

		Current study[a]			Tipton III[a]		
	x_1	a_1	a_{-1}	d_0	a_1	a_{-1}	d_0
He:Ne	0.1	-15.844	-20.474	4.331	-15.849	-20.485	4.334
	0.5	-19.382	-20.971	1.535	-19.390	-20.983	1.536
	0.9	-26.193	-23.471	4.144	-26.206	-23.484	4.147
Ar:Kr	0.1	-7.644	-7.959	1.255	-7.649	-7.963	1.256
	0.5	-8.530	-8.418	4.474	-8.534	-8.422	4.477
	0.9	-9.924	-9.286	1.224	-9.929	-9.290	1.225

[a] The values of a_1 and a_{-1} are scaled as 1×10^8 (m) and the values of d_0 are scaled as 1×10^6 (m)

Appendix B

Statistical sampling procedure

During the DSMC solution, it is required to sample a random value from a probability distribution function. The method employed by DSMC is the inverse cumulative method in which, the cumulative distribution function of a variable like x is equated by a randomly generated number in the range of zero to one, and accordingly, the value of x is obtained. The distribution function is defined as the probability magnitude of the variable, x, between x and $x + dx$ which is $f_x dx$. Referring to the definition of the distribution function, its integration over the whole range of x is equal to one:

$$\int_a^b f_x dx = 1 \tag{B.1}$$

Accordingly, the cumulative distribution function is defined as:

$$F_x = \int_a^x f_x dx \tag{B.2}$$

The value of the F_x is restricted between zero and one; therefore, cumulative distribution can be considered as the probability of a property with the distribution of f_x at point x. To sample a random value from a distribution f_x, a random value is generated between 0 and 1 and substituted for F_x. Then, the corresponding value of x can be calculated from

the inverse of the cumulative function Equation (B.2). Such a procedure is straightforward whenever F_x has an explicit reversible form; otherwise, the acceptance–rejection method has to be used. This method is more efficient in comparison to other alternatives like the Newton iteration method [64]. As an example, the Maxwellian equilibrium distribution function Equation (3.7) for each component of the thermal velocity is considered:

$$f_{v'_x} = \left(\beta/\sqrt{\pi}\right) \exp\left(-\beta^2 v'^2_x\right) \tag{B.3}$$

Its corresponding cumulative distribution function is:

$$F_{v'_x} = \tfrac{1}{2}\left(1 + erf\left(\beta v'_x\right)\right) \tag{B.4}$$

in which, erf represents the standard error function that is not invertible, and $\beta = 1/V_{mp}$ where V_{mp} is obtained from Equation (2.36). In the acceptance–rejection algorithm, the distribution function is normalized by a general function e_x, which must be larger than f_x for the entire x domain. A random x is chosen among its range. If $f_x/e_x > R_f$ then the chosen x is accepted; otherwise, it is rejected and the loop must be restarted by choosing a new random x until an accepted value is attained. In order to obtain the optimum algorithm, e_x is normally chosen as $f_x)_{max}$, which can be predicted in the DSMC method functions. Using this procedure, $f_{v'_x}/f_{v'_x})_{max}$ for the Maxwellian velocity distribution is evaluated from:

$$f_{v'_x}/f_{v'_x})_{max} = \exp\left(-\beta^2 v'^2_x\right) \tag{B.5}$$

Choosing v'_x randomly from the $f'_{v'_x}$ distribution between $-3V_{mp}$ to $3V_{mp}$ (this range is the most effective restriction of -∞ to +∞ for the molecular velocity) is done by the direct method as:

$$f'_{v'_x} = 1/(3/\beta - (-3/\beta)) = \beta/6 \tag{B.6}$$

The corresponding cumulative distribution function is:

$$F'_{v'_x} = \int_{-3/\beta}^{x} f'_{v'_x} dv'_x = \beta v'_x/6 + \tfrac{1}{2} \tag{B.7}$$

Equating $F'_{v'_x}$ to a random number, R_{f1}, gives the explicit expression for v'_x as:

$$v'_x = 3\left(2R_{f1} - 1\right)/\beta \tag{B.8}$$

Substituting into Equation B.5 results in:

$$f_{v'_x}/f_{v'_x})_{max} = \exp\left(-9\left(2R_{f1}-1\right)^2\right) \tag{B.9}$$

After calculating $f_{v'_x}/f_{v'_x})_{max}$ the second random number, R_{f2}, is generated, and the process repeated from Equation B.8 until $f_{v'_x}/f_{v'_x})_{max} < R_{f2}$. The accepted v'_x is a random selection from the Maxwellian velocity distribution. A special case is available when selecting two or three components of molecular velocities from Maxwellian distribution in the initialization process, where a direct method can be used to circumvent the time consuming acceptance–rejection process. The probability of two values of components of thermal velocity simultaneously in an element of the velocity space is the product of both single probabilities:

$$\begin{aligned} &f_{v'_x}dv'_x \cdot f_{v'_y}dv'_y = \left(\beta^2/\pi\right)\exp\left(-\beta^2 v'^2_x\right)\exp\left(-\beta^2 v'^2_y\right)dv'_x dv'_y = \\ &\left(\beta^2/\pi\right)\exp\left(-\beta^2\left(v'^2_x + v'^2_y\right)\right)dv'_x dv'_y \end{aligned} \tag{B.10}$$

Changing the variables as follows:

$$\begin{aligned} v'_x &= r\cdot\cos(\theta) \\ v'_y &= r\cdot\sin(\theta) \end{aligned} \tag{B.11}$$

and substituting to the previous equation, gives:

$$\begin{aligned} &f_{v'_x}dv'_x \cdot f_{v'_y}dv'_y = \left(\beta^2/\pi\right)\exp\left(-\beta^2 r^2\right) r dr d\theta = \\ &\exp\left(-\beta^2 r^2\right) d\left(\beta^2 r^2\right) d\theta/(2\pi) \end{aligned} \tag{B.12}$$

therefore:

$$f_{-\beta^2 r^2} = \exp\left(-\beta^2 r^2\right) \tag{B.13}$$

so that r and θ are sampled by:

$$\begin{aligned} \theta &= 2\pi R_f \\ r &= \sqrt{-ln(R_f)}/\beta \end{aligned} \tag{B.14}$$

and then velocity components are obtained from Equation B.11 [1]. Another concern is to sample the Larsen–Borgnakke distribution with regard to the internal energy redistribution. Recently, a faster method has been developed by Sun et al. [64] to expedite the

process. They used a variable change as:

$$\begin{aligned} y &= \left(\frac{E_a}{E_a + E_b}\right)^{1/8} \\ g &= \log_2\left(\frac{\zeta_a}{\zeta_a + \zeta_b}\right) \end{aligned} \tag{B.15}$$

According to the definition of y, the Larsen–Borgnakke distribution [35] becomes:

$$f_y = \frac{g\Gamma(\zeta_a + \zeta_b)}{\Gamma(\zeta_a)\Gamma(\zeta_b)} (y^g)^{\zeta_a - 1/g} (1 - y^g)^{\zeta_b - 1} \tag{B.16}$$

And by integration and normalization, the probability ratio for a specific value of y is obtained as:

$$\frac{P}{P_{max}} = \left(\frac{\zeta_a + \zeta_b - 1 - 1/g}{\zeta_a - 1/g} y^g\right)^{\zeta_a - 1/g} \left(\frac{\zeta_a + \zeta_b - 1 - 1/g}{\zeta_b - 1}(1 - y^g)\right)^{\zeta_b - 1} \tag{B.17}$$

Although change of variables back and forth increases the computational demand, the average number of iterations is reduced considerably; especially, for low energy fraction.

Appendix C

Navier–Stokes equations with slip–jump boundary conditions

The equations of this sections are adopted from the author's paper [21].

C.1 Navier-Stokes equations

The governing mass, momentum, energy, and species continuity equations for steady, laminar, non–reacting multi–component gas flows are [65]:

$$\nabla \cdot (\rho \mathbf{V}) = 0 \tag{C.1}$$

$$\nabla \cdot (\rho \mathbf{V}\mathbf{V}) = -\nabla p + \nabla \cdot \left[\mu \left(\nabla \mathbf{V} + \nabla \mathbf{V}^T \right) - \frac{2}{3} \mu \left(\nabla \cdot \mathbf{V} \right) \mathbf{I} \right] \tag{C.2}$$

$$\nabla \cdot (\rho \mathbf{V} h) = -\nabla \cdot \left(-\lambda \nabla T + \sum_{k=1}^{N_g} h_k \mathbf{J}_k \right) + \Phi \tag{C.3}$$

$$\nabla \cdot (\rho \mathbf{V} Y_k) = -\nabla \cdot \mathbf{J}_k \tag{C.4}$$

Here, ρ is the mixture density, $\mathbf{V}$ is the mass–averaged velocity vector, p and μ are pressure and viscosity, $\mathbf{I}$ is the identity tensor, λ is the mixture conductivity, h is the mixture

enthalpy, Φ is the viscous dissipation term, N_g is the total number of gas phase species, J_k is the mass diffusion flux, Y_k is the mass fraction, $c_{p,k}$ is the specific heat capacity, and h_k is the enthalpy of the k^{th} species. The species diffusion mass flux $\mathbf{J}_k$ is determined using the multi-component diffusion equation as [65]:

$$\mathbf{J}_k = \frac{\rho w_k}{\bar{w}^2} \sum_{j=1}^{N_g} w_j D_{kj} \nabla X_j - D_k^T \frac{1}{T} \nabla T \tag{C.5}$$

In this equation, X_k is the mole fraction and w_k is the molar mass of species "k", $\bar{w}$ is the mixture molar mass, D_{kj} is the tensor of ordinary diffusion coefficients, and D_k^T are the thermal diffusion coefficients [66].

Boundary Conditions

At the channel inlet, the mass flux of each species is constant. Since the mass flux of each species is constant at the channel inlet, the overall inlet mass flux will also remain constant. The inlet mass flux of each species consists of the diffusion mass flux and the convective mass flux of that species. When there is a positive diffusive flux of one species into the channel, in order to keep the mass flux constant, the inlet mass fraction of that species should be adjusted (lowered) accordingly. This way, the total mass flux of that species, $\vec{m}_k'' = \rho Y_k \mathbf{V} + \mathbf{J}_k$ remains constant. This procedure eliminates the inaccuracy in ignoring the incoming (or outgoing) inlet diffusive mass flux of species especially at low Péclet number flows. At each iteration, the inlet mass fraction of all species Y_k and the mass-averaged inlet velocity $\mathbf{V}$ are calculated using $\vec{m}_k'' = \rho Y_k \mathbf{V} + \mathbf{J}_k = \text{const}$ (N_g constraints) along with $\sum_{k=1}^{N_g} Y_k = 1$. The diffusive fluxes of species $\mathbf{J}_k$ are calculated from the previous iteration.

In the slip flow regime, the continuum equations for mass, momentum and energy conservation, described earlier, can still be employed but proper slip/jump boundary conditions should be specified to account for non–equilibrium effects in the Knudsen layer. In the present work, the set of velocity slip and temperature jump boundary conditions, proposed by Qazi Zade *et* al. [45] for multicomponent mixtures (including reacting mixtures [42]), are employed at the wall. These boundary conditions, developed based on the kinetic theory of gases, can be summarized as:

$$u_s = \frac{\sum_{k=1}^{N_g} \frac{\rho_{k,s}}{\sqrt{w_k}} \left[\theta_k \left(\frac{\lambda_k}{5\rho R} \frac{\partial \ln T}{\partial x} - \frac{J_{kx}}{\rho_k} \right) - (2-\theta_k) \frac{\bar{w} \tau_k^{xy}}{\rho w_k} \sqrt{\frac{\pi}{2R_k T}} \right]_s}{\sum_{k=1}^{N_g} \frac{\rho_{k,s}}{\sqrt{w_k}} \left[\theta_k \left(1 + \frac{\tau_k^{yy}}{2p} \right) + (2-\theta_k) \frac{J_{ky}}{\rho_k} \sqrt{\frac{\pi}{2R_k T}} \right]_s} \tag{C.6}$$

$$\frac{T_s}{T_w} = \frac{\sum_{k=1}^{N_g} \frac{\rho_k}{w_k^{3/2}} \left[\frac{\bar{\gamma}+1}{4(\bar{\gamma}-1)} + \frac{U^2}{4R_k T_w} \right] \left[\theta_k \left(1 + \frac{\tau_k^{yy}}{2p} \right) + \frac{J_{ky}(2-\theta_k)}{\rho_k} \sqrt{\frac{\pi}{2R_k T}} \right]_s}{\sum_{k=1}^{N_g} \frac{\rho_k}{w_k^{3/2}} \left[\frac{5(2-\theta_k)}{4} \sqrt{\frac{\pi}{2R_k T}} \left(\frac{J_{ky}}{\rho_k} - \frac{2\lambda_k}{5\rho R} \frac{\partial \ln T}{\partial y} \right) + \theta_k \mathcal{J}_1 \right]_s} \tag{C.7}$$

$$\frac{(\rho Y_k)_w}{(\rho Y_k)_s} \left(\frac{T_w}{T_s} \right)^{1/2} (\theta_k - \gamma_k) = \theta_k \left(1 + \frac{\tau_k^{yy}}{2p} \right) + (2-\theta_k) \frac{J_{ky}}{\rho_{k,s}} \sqrt{\frac{\pi}{2R_k T_s}} \tag{C.8}$$

where u_s and T_s are the velocity and temperature of the gas at the edge of the Knudsen layer, $\bar{\gamma}$ is the specific heat ratio, R_k is the gas constant of the k^{th} species and:

$$\tau_k^{xy} = -\mu_k \left(\frac{\partial U_x}{\partial y} + \frac{\partial U_y}{\partial x} \right) \tag{C.9a}$$

$$\tau_k^{yy} = \frac{2\mu_k}{3} \left(\frac{\partial U_x}{\partial x} + \frac{\partial U_z}{\partial z} - 2\frac{\partial U_y}{\partial y} \right) \tag{C.9b}$$

$$\mathcal{J}_1 = \frac{\bar{\gamma}+1}{4(\bar{\gamma}-1)} + \frac{\tau_k^{yy}}{8p} \frac{(3\bar{\gamma}-1)}{(\bar{\gamma}-1)} + \frac{5-3\bar{\gamma}}{4(\bar{\gamma}-1)} \frac{J_{ky}}{\rho_k} \sqrt{\frac{\pi}{2R_k T}} \tag{C.9c}$$

The diffusion flux of species in these equation are only important in catalytic reacting flows where some species are produced or consumed at the wall. These terms are only retained for completeness and obviously are zero in the present work. The accommodation coefficient θ is equal to zero for specular reflection at the wall and equal to 1 for diffuse reflection [28]. For most engineering applications they are close to unity and for comparison purposes they are assumed to be equal to 1 in the present work.

Numerical Implementation

The governing equations were discretized using the finite volume method. A non-staggered (colocated) arrangement was employed for the solution of the flow field following the Rhie and Chow [67] formulation. Implementing the Pressure Weighted Interpolation Method

(PWIM), the control volume face velocities are related to nodal pressure values. A linear deferred correction scheme is also used to improve the upwind approximation in descretizing the advection terms. The mixture transport properties as well as the pure species properties are obtained using the CHEMKIN database [68].

The finite volume code has been validated in the no–slip regime by comparing the simulation results with experimental and numerical data of Appel *et* al. [69]. The details can be found in Qazi Zade *et* al. [60], and therefore, are not repeated here.

References

[1] G. Bird, Molecular Gas Dynamics and the Direct Simulation Monte Carlo, Oxford Science Publication, 1994.

[2] G. Karniadakis, A. Beskok, N. Aluru, Microflows and Nanoflows; fundamentals and simulation, Springer, 2005.

[3] T. Doi, Numerical analysis of oscillatory Couette flow of a rarefied gas on the basis of the linearized Boltzmann equation, Vacuum 84 (2009) 734–737. doi:10.1016/j.vacuum.2009.10.007.

[4] R. D. Garcia, C. E. Siewert, The linearized Boltzmann equation: Sound-wave propagation in a rarefied gas, Zeitschrift Fur Angewandte Mathematik Und Physik 57 (2005) 94–122. doi:10.1007/s00033-005-0007-8.

[5] O. A. Sinkevich, A. M. Semenov, Solution of the Boltzmann equation by expanding the distribution function with several time and coordinate scales in the enskog series in knudsen parameter, Technical Physics 48 (2003) 1221–1225. doi:10.1134/1.1620111.

[6] D. Valougeorgis, S. Naris, Analytical Lattice Boltzmann Solutions for Thermal Flow Problems, Transport Theory and Statistical Physics 32 (2003) 645–656. doi:10.1081/TT-120025070.

[7] T. Abe, Takashi, Derivation of the Lattice Boltzmann Method by Means of the Discrete Ordinate Method for the Boltzmann Equation, Journal of Computational Physics 131 (1997) 241–246. doi:10.1006/jcph.1996.5595.

[8] F. Sharipov, L. G. Cumin, D. Kalempa, Plane Couette flow of binary gaseous mixture in the whole range of the Knudsen number, European Journal of Mechanics B-fluids 23 (2004) 899–906. doi:10.1016/j.euromechflu.2004.03.002.

[9] S. Ching, Y. Zhiqiang, Direct numerical test of the B-G-K model equation by the DSMC method, Acta Mechanica Sinica 16 (2000) 133–140. doi:10.1007/BF02486705.

[10] G. A. Bird, Approach to Translational Equilibrium in a Rigid Sphere Gas, Physics of Fluids 6 (1963) 1518–1519. doi:10.1063/1.1710976.

[11] M. Ikegawa, J. Kobayashi, Development of a rarefied gas flow simulation using the direct simulation Monte Carlo method, series 2, JSME International Journal 33 (3) (1990) 463–467.

[12] E. S. Piekos, K. S. Breuer, Numerical Modeling of Micromechanical Devices Using the Direct Simulation Monte Carlo Method, Journal of Fluids Engineering-transactions of The Asme 118. doi:10.1115/1.2817781.

[13] Y. Fang, W. Liou, Computations of the flow and heat transfer in mirodevices using DSMC with implicit boundary conditions, Journal of Heat Transfer 124 (2002) 338–345.

[14] M. Wang, Z. Li, Simulations for gas flows in microgeometries using the direct simulation Monte Carlo method, International Journal of Heat and Fluid Flow 25 (2004) 975–985.

[15] Q. Wang, X. Yan, Q. He, Heat-flux-specified boundary treatment for gas flow and heat transfer in microchannel using direct simulation Monte Carlo method, Internatonal Journal for Numerical Methods in Engineering 74 (2008) 1109–1127.

[16] M. Le, I. Hassan, DSMC simulation of gas mixing in T-shape micromixer, Applied Thermal Engineering 27 (2007) 2370–2377. doi:10.1016/j.applthermaleng.2007.03.012.

[17] F. Yan, B. . Farouk, Numerical simulation of gas flow and mixing in a microchannel using the direct simulation Monte Carlo method, Microscale Thermophysical Engineering 6 (2002) 235–251.

[18] G. Bird, Chemical reactions in dsmc, in: AIP Conference Proceedings, Vol. 1333, 2011, pp. 1195–1202.

[19] C. Lilley, M. Macrossan, A macroscopic chemistry method for the direct simulation of gas flows, Physics of Fluids 16 (2004) 2054–2067.

[20] C. Cercignani, A. Frezzotti, S. Sibilla, Hypersonic rarefied flows DSMC analysis by a simplified chemical model, Meccanica 30 (1995) 93–104.

[21] A. Qazi Zade, A. Ahmadzadegan, M. Renksizbulut, A detailed comparison between navier–stokes and dsmc simulations of multicomponent gaseous flow in microchannels, International Journal of Heat and Mass Transfer 55 (17) (2012) 4673–4681.

[22] A. Ahmadzadegan, J. Wen, M. Renksizbulut, The role of the velocity distribution in the DSMC pressure boundary condition for gas mixtures, International Journal of Modern Physics C 23 (2012) 1250087.

[23] W. Wagner, A convergence proof for Bird's direct simulation Monte Carlo method for the Boltzmann equation, Journal of Statistical Physics 66 (1992) 1011–1044.

[24] H. Struchtrup, Macroscopic Transport Equations for Rarefied Gas Flows: Approximation Methods in Kinetic Theory, Interaction of Mechanics and Mathematics, Springer, 2005.

[25] K. Koura, H. Matsumoto, Variable soft sphere molecular model for inverse-power-law or lennard-jones potential, Physics of Fluids A 3 (1991) 2459–2465.

[26] K. Koura, H. Matsumoto, Variable soft sphere molecular model for air species, Physics of Fluids A 4 (1992) 1083.

[27] H. A. Hassan, D. B. Hash, A generalized hard-sphere model for Monte Carlo simulation, Physics of Fluids 5 (1993) 738–744. doi:10.1063/1.858656.

[28] S. Chapman, T. Cowling, The Mathematical Theory of Non-uniform Gases, 3rd Edition, Cambridge University Press, 2003.

[29] C. Borgnakke, P. Larsen, Statistical collision model for monte carlo simulation of polyatomic gas mixture, Journal of Computational Physics 18 (1975) 405–420.

[30] R. Barber, D. Emerson, Challenges in modeling gas-phase flow in microchannels: From slip to transition, Heat Transfer Engineering 27 (2006) 3–12.

[31] C. Shen, Rarefied Gas Dynamics, Fundamentals, Simulations and Micro Flows, Springer, 2005.

[32] C. Cai, I. Boyd, J. Fan, Direct simulation method for low-speed microchannel flows, Journal of Thermophysics and Heat Transfer 14 (3) (2000) 368–378.

[33] P. S. Prasanth, J. K. Kakkassery, Direct simulation Monte Carlo (DSMC): A numerical method for transition-regime flows-A review, Journal of the Indian Institute of Science 86 (2006) 169–192.

[34] G. A. Bird, M. A. Gallis, J. R. Torczynski, D. J. Rader, Accuracy and efficiency of the sophisticated direct simulation Monte Carlo algorithm for simulating noncontinuum gas flows, Physics of Fluids 21. doi:10.1063/1.3067865.

[35] D. I. Pullin, Kinetic models for polyatomic molecules with phenomenological energy exchange, Physics of Fluids 21 (1978) 209–216. doi:10.1063/1.862215.

[36] S. Varoutis, C. Day, F. Sharipov, Rarefied gas flow through channels of finite length at various pressure ratios, Vacuum 86 (12) (2012) 1952 – 1959.

[37] S. Pantazis, D. Valougeorgis, F. Sharipov, End corrections for rarefied gas flows through capillaries of finite length, Vacuum 97 (2013) 26 – 29.

[38] E. Roohi, M. Darbandi, V. Mirjalili, Direct Simulation Monte Carlo Solution of Subsonic Flow Through Micro/Nanoscale Channels, Journal of Heat Transfer-transactions of The Asme 131. doi:10.1115/1.3139105.

[39] R. Fernandez-Feria, On the Gas Dynamics of Binary Gas Mixtures with Large Mass Disparity, Yale University, 1987.

[40] A. Q. Zade, M. Renksizbulut, J. Friedman, Homogeneous oxidation of hydrogen in catalytic mini/microchannels, Vol. 1, Edmonton, AB, Canada, 2011, pp. 35 – 43.

[41] A. Qazi Zade, M. Renksizbulut, J. Friedman, Heat transfer characteristics of developing gaseous slip-flow in rectangular microchannels with variable physical properties, International Journal of Heat and Fluid Flow 32 (1) (2011) 117 – 127.

[42] A. Q. Zade, M. Renksizbulut, J. Friedman, Rarefaction effects on the catalytic oxidation of hydrogen in microchannels, Chemical Engineering Journal 181–182 (2012) 643–654.

[43] Q. He, Q. Wang, X. Wang, L. Luo, DSMC simulation of low-speed gas flow and heat transfer in 2D rectangular micro-channel, Progress in Computational Fluid Dynamics 5. doi:10.1504/PCFD.2005.006757.

[44] A. Q. Zade, Slip/jump effects in catalytic reacting flows in microchannels, Ph.D. thesis, University of Waterloo (2012).

[45] A. Q. Zade, M. Renksizbulut, J. Friedman, Slip/jump boundary conditions for rarefied reacting/non-reacting multi-component gaseous flows, International Journal of Heat and Mass Transfer 51 (2008) 5063–5071. doi:10.1016/j.ijheatmasstransfer.2008.02.044.

[46] R. Nance, D. Hash, H. Hassan, Role of boundary conditions in Monte Carlo simulation of microelectromechanical systems, Journal of Thermophysics and Heat Transfer 12 (3) (1998) 447–449.

[47] J. Wu, K. Tseng, Development of a rarefied gas flow simulation using the direct simulation Monte Carlo method, JSME International Journal, Series 2 33 (3) (1990) 463–467.

[48] M. Wang, Z. Li, Gas mixing in microchannels using the direct simulation Monte Carlo method, International Journal of Heat and Mass Transfer 49 (2006) 1696–1702.

[49] E. Tipton, R. Tompson, S. Loyalka, Chapman-Enskog solutions to arbitrary order in sonine polynomials II: Viscosity in a binary, rigid-sphere, gas mixture, European Journal of Mechanics B/Fluids 28 (2009) 335–352.

[50] E. Tipton, R. Tompson, S. Loyalka, Chapman-Enskog solutions to arbitrary order in sonine polynomials III: Diffusion, thermal diffusion, and thermal conductivity in a binary, rigid-sphere, gas mixture, European Journal of Mechanics B/Fluids 28 (2009) 353–386.

[51] R. Gupta, C. Scott, J. Moss, Slip-Boundary Equations for Multicomponent Nonequilibrium Airflow, Technical paper 2452, NASA (1985).

[52] B. Kiryutin, G. Tirskii, Slip boundary condition on a catalytic surface in a multicomponent gas flow, Fluid Dynamics 31 (1996) 134–143.

[53] Q. Wang, C. Zhao, M. Zeng, Y. Wu, Numerical investigation of rarefied diatomic gas flow and heat transfer in a microchannel using DSMC with uniform heat flux boundary conditionpart II: Applications, Numerical Heat Transfer, Part B: Fundamentals 53 (2008) 174–187.

[54] I. Chorkendorff, J. Niemantsverdriet, Concepts of Modern Catalysis and Kinetics, WILEY-VCH Verlag GmbH & Co. KGaA, Weinheim, 2003.

[55] T. T. Tsong, Mechanisms of surface diffusion, Progress in Surface Science 67 (1) (2001) 235–248.

[56] R. Cukier, The effect of surface diffusion on surface reaction rates, The Journal of chemical physics 79 (1983) 2430.

[57] T. Golfinopoulos, Oxygen reduction on platinum: an eis study, Ph.D. thesis, Massachusetts Institute of Technology (2009).

[58] O. Deutschmann, R. Schmidt, F. Behrendt, J. Warnatz, Numerical modeling of catalytic ignition, 26th Symposium on Combustion/The Combustion Institute (2012) 1747–1754.

[59] P. Brown, G. Byrne, A. Hindmarsh, Vode, a variable-coefficient ode solver, SIAM Journal on Scientific and Statistical Computing 10 (1989) 1038–1051.

[60] A. Zade, M. Renksizbulut, J. Friedman, Contribution of homogeneous reactions to hydrogen oxidation in catalytic microchannels, Combustion and Flame 159 (2012) 784–792.

[61] E. H. Kennard, E. H. Kennard, Kinetic theory of gases: with an introduction to statistical mechanics, McGraw-hill New York, 1938.

[62] J. Corts, E. Valencia, P. Araya, Monte Carlo simulation studies of the catalytic combustion of methane, Catalysis Letters 112 (2006) 121–128. doi:10.1007/s10562-006-0174-z.

[63] O. Deutschmann, Modeling and Simulation of Heterogeneous Catalytic Reactions, Wiley, 2011.

[64] Q. Sun, J. Fan, I. D. Boyd, Improved sampling techniques for the direct simulation Monte Carlo method, Computers & Fluids 38 (2009) 475–479. doi:10.1016/j.compfluid.2008.04.010.

[65] R. B. Bird, W. E. Stewart, E. N. Lightfoot, Transport Phenomena, 2nd Edition, John Wiley & Sons, New York, 2001.

[66] J. O. Hirschfelder, C. F. Curtiss, R. B. Bird, Molecular Theory of Gases and Liquids, 2nd Edition, John Wiley & Sons, New York, 1965.

[67] M. C. Rhie, W. L. Chow, Numerical study of the turbulent flow past an airfoil with trailing edge separation, AIAA Journal 21 (11) (1983) 1525–1532.

[68] R. J. Kee, G. Dixon-Lewis, J. Warnatz, M. E. Coltrin, J. A. Miller, A fortran computer package for the evaluation of gas-phase multicomponent transport properties, Tech. Rep. SAND87-8246, Sandia (1986).

[69] C. Appel, J. Mantzaras, R. Schaeren, R. Bombach, A. Inauen, B. Kaeppeli, B. Hemmerling, A. Stampanoni, An experimental and numerical investigation of homogeneous

ignition in catalytically stabilized combustion of hydrogen/air mixtures over platinum, Combustion and Flame 128 (4) (2002) 340–368.